

Abstract

Measurement of total hadronic differential cross sections in the LArIAT experiment

Elena Gramellini

2018

6 Abstract goes here. Limit 750 words.

Measurement of total hadronic differential cross sections in the LArIAT experiment

A Dissertation
Presented to the Faculty of the Graduate School
of
Yale University
in Candidacy for the Degree of
Doctor of Philosophy

15 by
16 Elena Gramellini

¹⁷ Dissertation Director: Bonnie T. Fleming

18 Date you'll receive your degree

¹⁹

Copyright © 2018 by Elena Gramellini

²⁰

All rights reserved.

21

A mia mamma e mio babbo,

22

grazie per le radici e grazie per le ali.

23

To my mom and dad,

24

thank you for the roots and thank you for the wings.

²⁵ Contents

²⁶	Acknowledgements	viii
²⁷	0 Introduction	1
²⁸	1 The theoretical framework	2
²⁹	1.1 The Standard Model	2
³⁰	1.2 Neutrinos: tiny cracks in the Standard Model	4
³¹	1.2.1 Neutrinos in the Standard Model	4
³²	1.2.2 Neutrino Oscillations	6
³³	1.2.3 Make up of Neutrino Interactions	7
³⁴	1.3 Beyond the Standard Model	11
³⁵	1.3.1 Open Questions in Neutrino Physics	11
³⁶	1.3.2 Towards a more fundamental theory: GUTs	15
³⁷	1.4 Motivations for Hadronic Cross Sections in Argon	18
³⁸	1.4.1 Pion-Argon Total Hadronic Cross Section	19
³⁹	1.4.2 Kaon-Argon Total Hadronic Cross Section	29
⁴⁰	2 Liquid Argon Detectors at the Intensity Frontier	34
⁴¹	2.1 The Liquid Argon Time Projection Chamber Technology	34
⁴²	2.1.1 TPCs, Neutrinos & Argon	34
⁴³	2.1.2 LArTPC: Principles of Operation	37

44	2.1.3	Liquid Argon: Ionization Charge	39
45	2.1.4	Liquid Argon: Scintillation Light	45
46	2.1.5	Signal Processing and Event Reconstruction	49
47	2.2	The Intensity Frontier Program	53
48	2.2.1	Prospects for LArTPCs in Neutrino Physics: SBN and DUNE	53
49	2.2.2	Prospects for LArTPCs in GUT Physics: DUNE	55
50	2.2.3	Enabling the next generation of discoveries: LArIAT	56
51	3	LArIAT: Liquid Argon In A Testbeam	59
52	3.1	The Particles' Path to LArIAT	59
53	3.2	LArIAT Tertiary Beam Instrumentation	61
54	3.2.1	Bending Magnets	62
55	3.2.2	Multi-Wire Proportional Chambers	64
56	3.2.3	Time-of-Flight System	66
57	3.2.4	Punch-Through and Muon Range Stack Instruments	67
58	3.2.5	LArIAT Cosmic Ray Paddle Detectors	69
59	3.3	In the Cryostat	70
60	3.3.1	Cryogenics and Argon Purity	70
61	3.3.2	LArTPC: Charge Collection	73
62	3.3.3	LArTPC: Light Collection System	76
63	3.4	Trigger and DAQ	78
64	3.5	Control Systems	80
65	4	Total Hadronic Cross Section Measurement Methodology	86
66	4.1	Event Selection	87
67	4.1.1	Selection of Beamline Events	87
68	4.1.2	Particle Identification in the Beamline	88
69	4.1.3	TPC Selection: Halo Mitigation	88

70	4.1.4 TPC Selection: Shower Removal	89
71	4.2 Beamline and TPC Handshake: the Wire Chamber to TPC Match . .	90
72	4.3 The Thin Slice Method	92
73	4.3.1 Cross Sections on Thin Target	92
74	4.3.2 Not-so-Thin Target: Slicing the Argon	93
75	4.3.3 Corrections to the Raw Cross Section	95
76	4.4 Procedure testing with truth quantities	96
77	5 Data and MC preparation for the Cross Section Measurements	99
78	5.1 Cross Section Analyses Data Sets	99
79	5.2 Construction of a Monte Carlo Simulation for LArIAT	101
80	5.2.1 G4Beamline	101
81	5.2.2 Data Driven MC	105
82	5.3 Estimate of Backgrounds in the Pion Cross Section	107
83	5.3.1 Background from Pion Capture and Decay	109
84	5.3.2 Contributions from the Beamline Background	112
85	5.4 Estimate of Energy Loss before the TPC	115
86	5.5 Tracking Studies	119
87	5.5.1 Study of WC to TPC Match	119
88	5.5.2 Tracking Optimization	122
89	5.5.3 Angular Resolution	122
90	5.6 Calorimetry Studies	127
91	5.6.1 Energy Calibration	127
92	5.6.2 Kinetic Energy Measurement	129
93	6 Negative Pion Cross Section Measurement	133
94	6.1 Raw Cross Section	133
95	6.1.1 Statistical Uncertainty	135

96	6.1.2 Treatment of Systematics	137
97	6.2 Corrections to the Raw Cross Section	138
98	6.2.1 Background subtraction	138
99	6.2.2 Efficiency Correction	141
100	6.3 Results	145
101	7 Positive Kaon Cross Section Measurement	147
102	7.1 Raw Cross Section	147
103	A Measurement of LArIAT Electric Field	148

¹⁰⁴ Acknowledgements

¹⁰⁵ “*Dunque io ringrazio tutti quanti.*

¹⁰⁶ *Specie la mia mamma che mi ha fatto così funky.”*

¹⁰⁷ – Articolo 31, Tanqi Funky, 1996 –

¹⁰⁸ “*At last, I thank everyone.*

¹⁰⁹ *Especiallly my mom who made me so funky.”*

¹¹⁰ – Articolo 31, Tanqi Funky, 1996 –

¹¹¹ A lot of people are awesome, especially you, since you probably agreed to read
¹¹² this when it was a draft.

¹¹³ Chapter 0

¹¹⁴ Introduction

¹¹⁵ Chapter 1

¹¹⁶ The theoretical framework

¹¹⁷ 1.1 The Standard Model

¹¹⁸ The Standard Model (SM) of particle physics is the most accurate theoretical descrip-
¹¹⁹ tion of the subatomic world and, in general, one of the most precisely tested theories
¹²⁰ in the history of physics. The SM describes the strong, electromagnetic and weak
¹²¹ interactions among elementary particles in the framework of quantum field theory,
¹²² accounting for the unification of electromagnetic and weak interactions for energies
¹²³ above the vacuum expectation value (VEV) of the Higgs field. The SM does not
¹²⁴ describe gravity or general relativity.

¹²⁵ The Standard Model is a gauge theory based on the local group of symmetry

$$G_{SM} = SU(3)_C \otimes SU(2)_T \otimes U(1)_Y \quad (1.1)$$

¹²⁶ where the subscripts indicate the conserved charges: the strong charge, or color C,
¹²⁷ the weak isospin T (or rather its third component T3) and the hypercharge Y. These
¹²⁸ quantities can be related to the electric charge Q through the Gell-Mann-Nishijima
¹²⁹ relation:

$$Q = \frac{Y}{2} + T_3. \quad (1.2)$$

Generation	I	II	III	T	Y	Q
Leptons	$\begin{pmatrix} \nu_e \\ e \end{pmatrix}_L$	$\begin{pmatrix} \nu_\mu \\ \mu \end{pmatrix}_L$	$\begin{pmatrix} \nu_\tau \\ \tau \end{pmatrix}_L$	1/2 -1/2	-1 -1	0 -1
	e_R	μ_R	τ_R	0	-2	1
Quarks	$\begin{pmatrix} u \\ d' \end{pmatrix}_L$	$\begin{pmatrix} c \\ s' \end{pmatrix}_L$	$\begin{pmatrix} t \\ b' \end{pmatrix}_L$	1/2 -1/2	1/3 1/3	2/3 -1/3
	u_R d'_R	c_R s'_R	t_R b'_R	0 0	4/3 -2/3	2/3 -1/3

Table 1.1: SM elementary fermions. The subscripts L and R indicate respectively the negative helicity (left-handed) and the positive helicity (right-handed).

130 In the quantum field framework, the elementary particles correspond to the ir-
 131 reducible representations of the G_{SM} symmetry group. In particular, the particles
 132 are divided in two categories, fermions and bosons, according to their spin-statistics.
 133 Described by the Fermi-Dirac statistics, fermions have half-integer spin and are some-
 134 times called “matter-particles”. Bosons or “force carriers” have integer spin, follow
 135 the Bose-Einstein statistics and mediate the interaction between fermions. The fun-
 136 damental fermions and their quantum numbers are listed in Tab 1.1.

137 Quarks can interact via all three the fundamental forces; they are triplets of
 138 $SU(3)_C$, that is they can exist in three different colors: C = R, G, B. If one chooses
 139 a base where u , c and t quarks are simultaneously eigenstates of both the strong
 140 and the weak interactions, the remaining eigenstates are usually written as d , s and
 141 b for the strong interaction and d' , s' and b' for the weak interaction, because the
 142 latter ones are the result of a Cabibbo rotation on the first ones. Charged leptons
 143 interact via the weak and the electromagnetic forces, while neutrinos only interact
 144 via the weak force. The gauge group univocally determines the number of gauge
 145 bosons that carry the interaction; the gauge bosons correspond to the generators of

₁₄₆ the group: eight gluons (g) for the strong interaction, one photon (γ) and three bosons
₁₄₇ (W^\pm , Z^0) for the electroweak interaction. A gauge theory by itself cannot provide
₁₄₈ a description of massive particles, but it is experimentally well known that most of
₁₄₉ the elementary particles have non-zero masses. The introduction of massive fields in
₁₅₀ the Standard Model lagrangian would make the theory non-renormalizable, and - so
₁₅₁ far - mathematically impossible to handle. This problem is solved in the SM by the
₁₅₂ introduction of a scalar iso-doublet $\Phi(x)$, the Higgs field, which gives mass to W^\pm and
₁₅₃ Z^0 gauge bosons through the electroweak symmetry breaking mechanism and to the
₁₅₄ fermions through Yukawa coupling [74, 75]. The discovery of the Higgs boson in 2012
₁₅₅ by the LHC experiments [40, 41] marked the ultimate confirmation of a long history
₁₅₆ of successful predictions by the SM.

₁₅₇ **1.2 Neutrinos: tiny cracks in the Standard Model**

₁₅₈ **1.2.1 Neutrinos in the Standard Model**

₁₅₉ Neutrino were introduced in the SM as left-handed massless Weyl spinors. The Dirac
₁₆₀ equation of motion

$$(i\gamma^\mu \partial_\mu - m)\psi = 0 \quad (1.3)$$

₁₆₁ for a fermionic field

$$\psi = \psi_L + \psi_R \quad (1.4)$$

₁₆₂ is equivalent to the equations

$$i\gamma^\mu \partial_\mu \psi_L = m\psi_R \quad (1.5)$$

₁₆₃

$$i\gamma^\mu \partial_\mu \psi_R = m\psi_L \quad (1.6)$$

₁₆₄ for the chiral fields ψ_R and ψ_L , whose evolution in space and time is coupled
₁₆₅ through the mass m . If the fermion is massless, the chiral fields decouple and the

₁₆₆ fermion can be described by a single Weyl spinor with two independent components [114]. Pauli initially rejected the description of a physical particle through
₁₆₇ a single Weyl spinor because of its implication of parity violation. In fact, since the
₁₆₈ spatial inversion operator throws $\psi_R \leftrightarrow \psi_L$, parity is conserved only if the both the
₁₆₉ chiral components exist at the same time. For the neutrino introduction in the SM,
₁₇₀ experiments came in help of the theoretical description. The constraint of parity
₁₇₁ conservation weakened after Wu's experiment in 1957 [117]. Additionally, there was
₁₇₂ no experimental indication for massive neutrinos, nor evidence of interaction via the
₁₇₃ neutrino right-handed component.

₁₇₅ The symmetry group $SU(2)_T \otimes U(1)_Y$ is the only group relevant for neutrino
₁₇₆ interactions. The SM electroweak lagrangian is the most general renormalizable la-
₁₇₇ grangian invariant under the local symmetry group $SU(2)_T \otimes U(1)_Y$. The lagrangian
₁₇₈ couples the weak isotopic spin doublets and singlets described in Table 1.1 with the
₁₇₉ gauge bosons A_a^μ ($a = 1, 2, 3$) and B^μ , and Higgs doublet $\Phi(x)$:

$$\begin{aligned}
\mathcal{L} = & i \sum_{\alpha=e,\mu,\tau} \bar{L}'_{\alpha L} \not{D} L'_{\alpha L} + i \sum_{\alpha=1,2,3} \bar{Q}'_{\alpha L} \not{D} Q'_{\alpha L} \\
& + i \sum_{\alpha=e,\mu,\tau} \bar{l}'_{\alpha R} \not{D} l'_{\alpha R} + i \sum_{\alpha=d,s,b} \bar{q}'^D_{\alpha R} \not{D} q'^D_{\alpha R} + i \sum_{\alpha=u,e,t} \bar{q}'^U_{\alpha R} \not{D} q'^U_{\alpha R} \\
& - \frac{1}{4} A_{\mu\nu} A^{\mu\nu} - \frac{1}{4} B_{\mu\nu} B^{\mu\nu} \\
& + (D_\rho \Phi)^\dagger (D^\rho \Phi) - \mu^2 \Phi^\dagger \Phi - \lambda (\Phi^\dagger \Phi)^2 \\
& - \sum_{\alpha,\beta=e,\mu,\tau} \left(Y_{\alpha\beta}^n \bar{L}'_{\alpha L} \Phi l'_{\beta R} + Y_{\alpha\beta}^{n*} \bar{l}'_{\beta R} \Phi^\dagger L'_{\alpha L} \right) \\
& - \sum_{\alpha=1,2,3} \sum_{\beta=d,s,b} \left(Y_{\alpha\beta}^D \bar{Q}'_{\alpha L} \Phi q'^D_{\beta R} + Y_{\alpha\beta}^{D*} \bar{q}'^D_{\beta R} \Phi^\dagger Q'_{\alpha L} \right) \\
& - \sum_{\alpha=1,2,3} \sum_{\beta=u,c,t} \left(Y_{\alpha\beta}^U \bar{Q}'_{\alpha L} \tilde{\Phi} q'^U_{\beta R} + Y_{\alpha\beta}^{U*} \bar{q}'^U_{\beta R} \tilde{\Phi}^\dagger Q'_{\alpha L} \right).
\end{aligned} \tag{1.7}$$

₁₈₀ The first two lines of the lagrangian summarize the kinetic terms for the fermionic

181 fields and their coupling to the gauge bosons $A_a^{\mu\nu}$, $B^{\mu\nu}$ ¹. The third line describes
182 the kinetic terms and the self-coupling terms of the gauge bosons. The forth line is
183 the Higgs lagrangian, which results in the spontaneous symmetry breaking. The last
184 three lines describe the Yukawa coupling between fermions and the Higgs field, origin
185 of the fermions' mass.

186 The coupling between left-handed and right-handed field generates the mass term
187 for fermions. The SM assumes only left-handed components for neutrinos, thus im-
188 plying zero neutrino mass. Since any linear combination of massless fields results in a
189 massless field, the flavor eigenstates are identical to the mass eigenstates in the SM.

190 1.2.2 Neutrino Oscillations

191 The determination of the flavor of a neutrino dynamically arises from the correspond-
192 ing charged lepton associated in a change current interaction; for example, a ν_e is a
193 neutrino which produces an e^- , a $\bar{\nu}_\mu$ is a neutrino which produces a μ^+ , etc. The
194 neutrino flavor eigenstates $|\nu_\alpha\rangle$, with $\alpha = e, \mu, \tau$, are orthogonal to each other and
195 form a base for the weak interaction matrix.

196 Overwhelming experimental data show that neutrinos change flavor during their
197 propagation [100]. This phenomenon, called “neutrino oscillations”, was predicted
198 first by Bruno Pontecorvo in 1957 [101]. Neutrino oscillations are possible only if the
199 neutrino flavor eigenstate are not identical to the mass eigenstates, thus resulting in
200 the first evidence of physics beyond the Standard Model. A minimal extension of the
201 SM introduces three mass eigenstates, $|\nu_i\rangle$ ($i = 1, 2, 3$), whose mass m_i is well defined.
202 The unitary Pontecorvo-Maki-Nakagawa-Sakata matrix transforms the spinor wave
203 functions (ψ) of each component between the flavor and mass bases as follows

1. In gauge theories the ordinary derivative ∂_μ is substituted with the covariant derivative D_μ . Here $D_\mu = \partial_\mu + igA_\mu \cdot I + ig'B_\mu \frac{Y}{2}$, where I and Y are the SU(2)_L and U(1)_Y generators, respectively.

$$\sum_{\alpha} \psi_{\alpha} |\nu_{\alpha}\rangle = \sum_i \psi_i |\nu_i\rangle, \rightarrow \psi_{\alpha} = U_{PMNS} \psi_i, \quad (1.8)$$

204 with

$$U_{PMNS} = \begin{bmatrix} c_{12} & s_{12} & 0 \\ -s_{12} & c_{12} & 0 \\ 0 & 0 & 1 \end{bmatrix} \begin{bmatrix} c_{13} & 0 & s_{13} e^{-i\delta} \\ 0 & 1 & 0 \\ -s_{13} e^{-i\delta} & 0 & c_{13} \end{bmatrix} \begin{bmatrix} 1 & 0 & 0 \\ 0 & c_{23} & s_{23} \\ 0 & -s_{23} & c_{23} \end{bmatrix} \begin{bmatrix} e^{i\alpha_1} & 0 & 0 \\ 0 & e^{i\alpha_2} & 0 \\ 0 & 0 & 1 \end{bmatrix} \quad (1.9)$$

205 where c e s stand respectively for cosine and sine of the corresponding mixing
206 angles (θ_{12} , θ_{23} and θ_{13}), δ is the Dirac CP violation phase, α_1 and α_2 are the eventual
207 Majorana CP violation phases. Experimental results on neutrino oscillations are
208 generally reported in terms of the mixing angles and of the squared mass splitting
209 $\Delta m_{ab}^2 = m_a^2 - m_b^2$, where a and b represent the mass eigenstates. A summary of the
210 current status of experimental results, albeit partial, is given in table 1.2.

Table 1.2: Summary of experimental results on neutrino oscillation parameters. ADD CITATIONS

	Value	Precision	Experiment
θ_{23}	45°	9.0%	Super Kamiokande, MINOS,
Δm_{23}^2	$2.5 \cdot 10^{-3} \text{ eV}^2$	1.8%	No ν a, MACRO
θ_{12}	34°	5.8%	SNO, Gallex,
Δm_{12}^2	$7.4 \cdot 10^{-5} \text{ eV}^2$	2.8%	SAGE, KamLAND
θ_{13}	9°	4.7%	DAYA Bay,
Δm_{13}^2	$2.5 \cdot 10^{-3} \text{ eV}^2$	1.8%	RENO

211 1.2.3 Make up of Neutrino Interactions

212 All neutrino experiments involving the detection of single neutrinos are concerned
213 with neutrino interactions (and neutrino cross sections) on nuclei. Given the invis-
214 ible nature of the neutrino, characterizing the products of its interaction is the only

215 method to a) assess the neutrino presence, b) detect its flavor in case of a charge
216 current interaction and c) eventually reconstruct its energy.

217 Historically, neutrino interactions with the nucleus in the GeV region are divided
218 into three categories into three categories whose contributions change as a function
219 of increasing neutrino energy:: quasi elastic (QE), resonant (RES), and deep inelas-
220 tic (DIS) scattering. All current and forthcoming oscillation experiments live in the
221 0.1-10 GeV transition region, which encompasses the energy where the QE neutrino-
222 nucleus interaction transitions into RES and then into DIS. For scattering off free
223 nucleons, neutrino and antineutrino QE charge current scattering refers to the pro-
224 cess $\nu_l n \rightarrow l^- p$ and $\bar{\nu}_l p \rightarrow l^+ n$ where a charged lepton and single nucleon are ejected in
225 the elastic interaction. Resonant scattering refers to an inelastic collision producing a
226 nucleon excited state (Δ, N^*) – the resonance – which then quickly decays, most often
227 to a nucleon and single-pion final state. DIS refers to the head-on collision between
228 the neutrino and a parton inside the nucleon, producing hadronization and subse-
229 quent abundant production of mesons and nucleons. In addition to such interactions
230 between the neutrino and a single component of the nucleus, neutrinos can also inter-
231 act with the nucleus as a whole, albeit more rarely, a well documented process called
232 coherent meson production scattering [57]; the signature of such process is the pro-
233 duction of a distinctly forward-scattered single meson final state, most often a pion.
234 This simple picture of neutrino interactions works rather well for scattering off of
235 light nuclear targets, such as the H₂ and D₂ of bubble chamber experiments [63], but
236 the complexity of the nuclear structure for heavier nuclei such as argon complicates
237 this model.

238 As we will discuss in Chapter 2, the properties of argon make it a good candidate
239 for an interacting medium in neutrino experiments; in particular the density of its
240 interaction centers increases the yield of neutrino interactions and allows for relatively
241 compact detectors. Though, the choice of a relatively heavy nuclear target comes at

242 the cost of enhancing nuclear effects which modify the kinematic and final state of
243 the neutrino interaction products.

244 Nuclear effects can potentially affect neutrino event rates, final state particle emis-
245 sion, neutrino energy reconstruction, and the neutrino/antineutrino ratios, carrying
246 deep implications for oscillation experiments. Even in the case of “simple” QE scat-
247 tering, intra-nuclear hadron rescattering and correlation effects between the target
248 nucleons can cause the ejection of additional nucleons in the final state, modifying
249 the final state kinematics and topology. In the case of resonant and DIS scattering,
250 the hadronic interactions of meson and nucleons produced in the decay of the res-
251 onance or during hadronization complicate this picture even more. A large source
252 of uncertainty in modeling nuclear effects in neutrino interactions come from mesons
253 interactions (and re-interactions) in the nucleus, e.g., pion re-scattering, charge ex-
254 change, and absorption.

255 A renewed interest for neutrino cross section measurements surged in recent years,
256 along with a lively discussion on the data reporting; the historical method of reporting
257 the neutrino cross section as a function of the neutrino energy or momentum trans-
258 fered shakes under the weight of its dependency on the chosen nuclear model. On one
259 hand, correcting for nuclear effects in neutrino interaction can introduce unwanted
260 sources of uncertainty and model dependency especially due to the mis-modeling of
261 the meson interactions. On the other, avoiding this correction makes a comparison
262 between neutrino interactions on different target nuclei extremely difficult.

263 Data on neutrino scattering off many different nuclei are available for both charged
264 current (CC) and neutral current (NC) channels, as summarized in [63]. A summary
265 of the results on QE, resonant and DIS scattering for neutrinos and antineutrinos from
266 accelerators on different target is reported in Figure 1.1, where the (NUANCE) [37]
267 event generator is used as comparison with the theory.

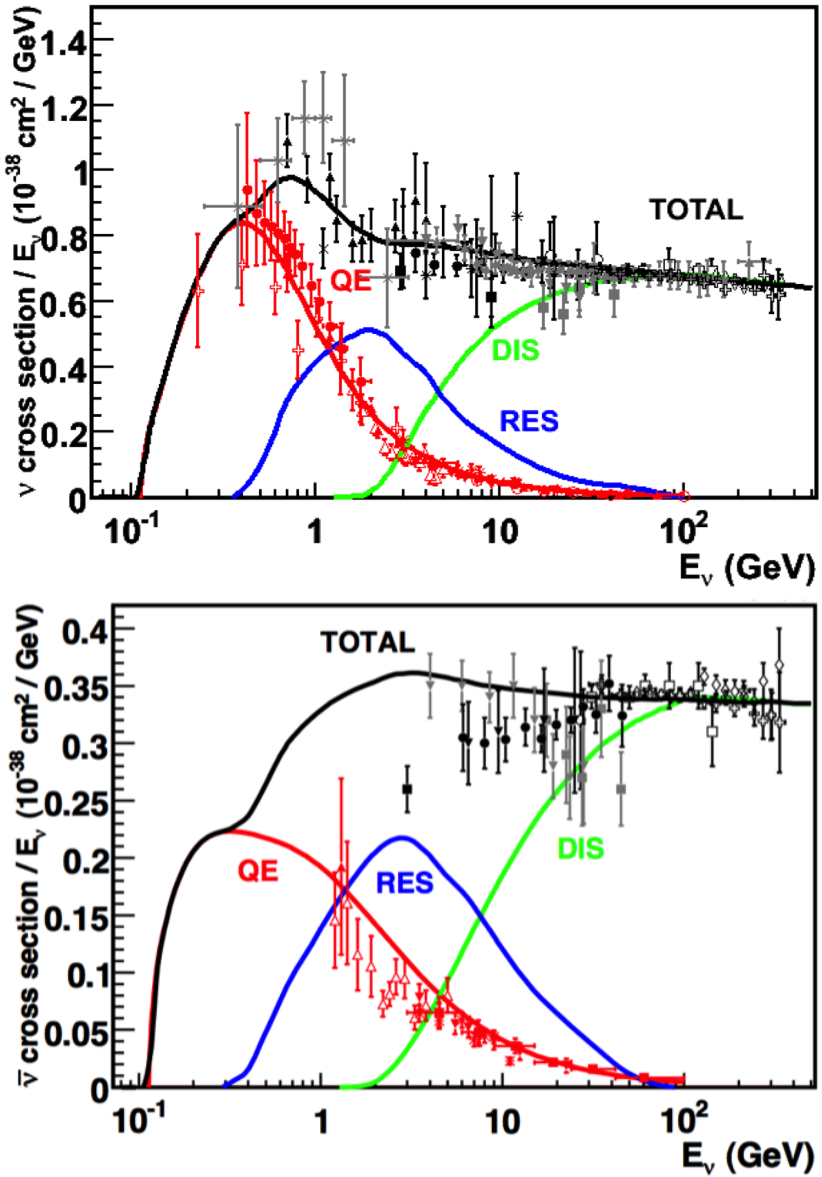


Figure 1.1: Total neutrino (top) and antineutrino (bottom) CC cross sections per nucleon divided by neutrino energy as a function of energy as reported in [63]. Predictions for the total (black), the QE (red), resonant (blue) and DIS (green) are provided by the NUANCE generator. The quasi-elastic scattering data and predictions have been averaged over neutron and proton targets (isoscalar target).

268 1.3 Beyond the Standard Model

269 The discovery of neutrino oscillation and its implication of non-zero neutrino mass
270 mark the beginning of a new, exciting era in neutrino physics: the era of physics Be-
271 yond the Standard Model (BSM) at the intensity frontier. We are currently searching
272 for new, deeper theories that can accommodate neutrinos with tiny but non-zero
273 masses, while remaining consistent with the rest of the Standard Model.

274 1.3.1 Open Questions in Neutrino Physics

275 On one hand, the last three decades of experiments in neutrino oscillations brought
276 spectacular advancements in the understanding of the oscillations pattern, measuring
277 the neutrino mixing angles and mass splitting with a precision of less than 10%. On
278 the other, they opened the field for a series of questions needing experimental answers.

279 **Sterile neutrinos.** Hints to the existence of at least one additional neutrino,
280 in the form of various anomalies, have been puzzling physicists almost from the be-
281 ginning of neutrino oscillation searches. Originally designed to look for evidence of
282 neutrino oscillation, the Liquid Scintillator Neutrino Detector (LSND) [53] provided
283 a first conflicting result with the Standard Model expectation of only three neutrinos.
284 A second conflicting result has also been provided by the MiniBooNE experiment [49].

285 The LSND and MiniBooNE ν_e and $\bar{\nu}_e$ appearance results, known as the “LSND and
286 MiniBooNE anomalies” [14, 15, 23], may be interpreted under the assumption of a new
287 right-handed neutrino. The additional neutrino needs to be “sterile”, i.e needs not
288 to couple with the electroweak force carriers, in order to meet the constraint imposed
289 by the measurement of the width of the Z boson [2]. The new sterile neutrino would
290 mainly be composed of a heavy neutrino ν_4 with mass m_4 such that $m_1, m_2, m_3 \ll m_4$
291 and $\Delta m^2 = \Delta m_{14}^2 \sim [0.1 - 10]$ eV². The introduction of sterile neutrinos is an ap-
292 pealing line of thinking, since this renormalizable generalization of the SM has the

293 potential to impact long standing questions in high energy physics and cosmology:
 294 light sterile neutrinos are candidates for dark matter particles and there are ideas
 295 that the theory could be adjusted to explain the baryon asymmetry of the Universe
 296 via leptogenesis [70].

297 **CP Violation In Lepton Sector.** The measurement of non-zero value for the
 298 oscillation parameter θ_{13} allows the exploration of low-energy CP violation in the lep-
 299 ton sector at neutrino long baseline oscillation experiments, enabling the possibility
 300 to measure the Dirac CP-violating phase δ . Exciting theoretical results tie δ directly
 301 to the generation of the baryon asymmetry of the Universe at the Grand Unified
 302 Theory scale **a couple of cit would be nice**. According to the theoretical model de-
 303 scribed in [99], for example, leptogenesis can be achieved if $|\sin \theta_{13} \sin \delta| > 0.11$, i.e.
 304 $\sin \delta > 0.7$.

305 The asymmetry in the oscillation probability of neutrinos and antineutrinos is the ob-
 306 servable sensitive to the Dirac CP-violating phase δ leveraged in neutrino oscillation
 307 experiments. Using the parameterization of the PMNS matrix shown in Equation
 308 1.9, the difference between the probability of $\nu_e \rightarrow \nu_\mu$ oscillation and the probability
 309 of $\bar{\nu}_e \rightarrow \bar{\nu}_\mu$ oscillation can be parametrized as follows [38],

$$P_{\nu_e \rightarrow \nu_\mu} - P_{\bar{\nu}_e \rightarrow \bar{\nu}_\mu} = J \cos \left(\pm \delta - \frac{\Delta_{31} L}{2} \right) \sin \left(\frac{\Delta_{21} L}{2} \right) \sin \left(\frac{\Delta_{31} L}{2} \right) \quad (1.10)$$

310 where

$$J = \cos \theta_{13} \sin 2\theta_{13} \sin 2\theta_{12} \sin 2\theta_{23} \quad (1.11)$$

311 is the Jarlskog invariant [80], L the neutrino baseline, i.e. the distance between
 312 the neutrino production and detection points, and Δ_{ab} a factor proportional to the
 313 sign and magnitude of the mass splitting. From these equations, it is clear how the
 314 relative large value of θ_{13} is a happy accident necessary not to completely suppress
 315 the sensitivity to CP violation. The equations also show how the sensitivity to δ is

316 tied to the measurement of the least precisely measured mixing angle, θ_{23} (via the
317 $\sin 2\theta_{23}$ term) and to an other unknown quantity, the neutrino “mass hierarchy” (via
318 the Δ_{ab} terms). The precise determination of θ_{23} is often referred as to “the octant
319 problem”. Current experimental results [3, 12] are consistent with $\theta_{23} = 45^\circ$, which
320 would imply maximal mixing between $\nu_\mu - \nu_\tau$, hinting to an intriguing new symmetry.
321 Therefore, a precise measurement of θ_{23} is of great interest for theoretical models of
322 quark-lepton universality [73, 91, 104], whose quark and lepton mixing matrices are
323 proportional to the deviation of θ_{23} from 45° .

324 **Neutrino mass hierarchy.** The “mass hierarchy” problem refers to the unknown
325 ordering of the value of absolute mass of the neutrino mass eigenstates. Current
326 oscillation experiments are sensitive only to the magnitude of the mass splitting, and
327 not directly to its sign. In a framework where the lightest neutrino mass (arbitrarily)
328 corresponds to the first eigenstate m_1 , it is unknown whether $m_2 - m_1 < m_3 - m_1$
329 (Normal Hierarchy) or $m_2 - m_1 > m_3 - m_1$ (Inverted Hierarchy). The mass hierarchy
330 affects not only the sensitivity to CP violation searches in long baseline oscillation
331 experiments, but also the sensitivity to determine whether neutrinos are Majorana
332 particles in neutrinoless double beta decay experiments.

333 **Majorana or Dirac?** Evidence of neutrino oscillations demands the introduction
334 of a mechanism which can give mass to the neutrinos. This mechanism should possibly
335 also explain why neutrino masses are at least six orders of magnitude lower than the
336 electron mass (the second lightest SM fermion). In a description of neutrinos as Dirac
337 4-component spinors, the neutrino field acquires mass via the Higgs mechanism as
338 any other fermion of the SM. In this case, the neutrino mass is given by $m_a = \frac{y_a^\nu v}{\sqrt{2}}$,
339 where v is the Higgs VEV and y_a^ν is the Yukawa coupling between the Higgs and the
340 neutrino. The smallness of neutrino masses can only be pinned on a tiny Yukawa
341 coupling which is not justified by the theory.

342 In 1937, Majorana demonstrated that the introduction of a two components spinor is

343 sufficient to describe a massive fermion [90]. The Dirac equations of motion for the
 344 chiral fields (equations 1.5 and 1.6) hold true in the case of two components spinor
 345 under the assumption that the chiral components ψ_R and ψ_L are correlated through
 346 the charge conjugation matrix \mathcal{C} , $\psi_R = \mathcal{C}\bar{\psi}_L$. Therefore the theory is applicable only
 347 to neutral fermions. Neutrinos are the only neutral elementary particles in the SM
 348 – the only possible Majorana particle candidate. This theory constructs a neutrino
 349 Majorana mass term \mathcal{L}_5 of the following form in the Higgs unitary gauge

$$\mathcal{L}_5 = \frac{1}{2} \frac{gv^2}{\mathcal{M}} \nu_L^T \mathcal{C}^\dagger \nu_L, \quad (1.12)$$

350 where g is the coupling coefficient, v the Higgs VEV and \mathcal{M} a constant with the
 351 dimension of the mass proportional to the scale of new physics. The \mathcal{L}_5 term would
 352 introduce a non-renormalizable term in the lagrangian, since it has dimensions of
 353 energy to the fifth power. This is not allowed in the SM lagrangian; however, the
 354 existence of such terms is plausible if we consider the SM as an effective theory
 355 at low energy, manifestation of the symmetry breaking of a more general theory at
 356 higher energy, e.g. a Grand Unified Theory (GUT), and not the definitive theory.
 357 The mass term in eq 1.12 implies the neutrino mass to be $m = \frac{gv^2}{\mathcal{M}}$. The coupling
 358 coefficient can be of the order of any other fermion's coupling coefficient, since the
 359 smallness of neutrino masses is achieved by the big value of the new physics mass
 360 scale alone. This vanilla formulation is the conceptual basis for many flavors of *see-*
 361 *saw mechanism* [119], which we will not discuss here in any detail. However, it is
 362 fascinating how the puzzle of the neutrino mass hints to the existence of a deeper and
 363 more complete theory.

364 From a kinematic point of view, Dirac and Majorana neutrinos satisfy the same
 365 energy-momentum dispersion relationship. Thus, it is impossible to discern the neu-
 366 trino nature through kinematic effects such as neutrino oscillations. Neutrinoless

367 double beta decay searches are the most promising way to understand the nature of
368 the neutrino and are therefore subject of great theoretical and experimental interest.
369 Observation of the lepton number violating process $0\nu\beta\beta$ would imply neutrinos have
370 a Majorana component. Depending on the mass hierarchy, the theory also predicts
371 $0\nu\beta\beta$ exclusion regions and confirmation of the sole Dirac component for neutrinos
372 [43].

373

374 1.3.2 Towards a more fundamental theory: GUTs

375 Despite its highly predictive power, a number of conceptual issues arise in the SM
376 which disfavor it to be a good candidate for a fundamental theory.

377 The SM does not include a suitable dark matter candidate and a mechanisms
378 that accounts for the baryon asymmetry of the universe. Additionally, up to a total
379 of 25 parameters remain seemingly arbitrary and need to be fitted to data: 3 gauge
380 couplings, 9 charged fermion masses, 3 mixing angles and one CP phase in the CKM
381 matrix, the Higgs mass and quartic coupling, θ_{QCD} , 3 neutrino mixing angles, 1 Dirac
382 phase and, eventually, 2 Majorana phases.

383 From a group theory perspective, the SM has a rather complex group structure,
384 where a gauge group is formed with the direct product of other three groups as shown
385 in eq. 1.1. Drawing a parallel with the electroweak symmetry breaking mechanism,
386 where the $SU(2)_T \otimes U(1)_Y$ is recovered from $U(1)_{EM}$, an interesting line of simplifi-
387 cation for the SM group structure would be to devise a similar mechanism where
388 $SU(3)_C \otimes SU(2)_T \otimes U(1)_Y$ is recovered from an hypothetical larger group. IS THIS
389 CORRECT? Just as the electroweak unification becomes evident at energies higher
390 than the Higgs VEV, a direct manifestation of Grand Unification Theories (GUTs)
391 would occur at even higher energies.

392 As the smallness of neutrino masses suggests the existence of a higher mass scale,

393 an other, even stronger, hint to Grand Unification comes from the slope of running
 394 of the coupling constants. The coupling constants for the electromagnetic, weak and
 395 strong interactions in the SM vary as a function of the interaction energy as shown
 396 in figure 1.2; they do not exactly meet under the current experimental constraints,
 397 but their trend is interesting enough to push for the construction of theories where
 398 perfect unification is achieved through the addition of new particles.

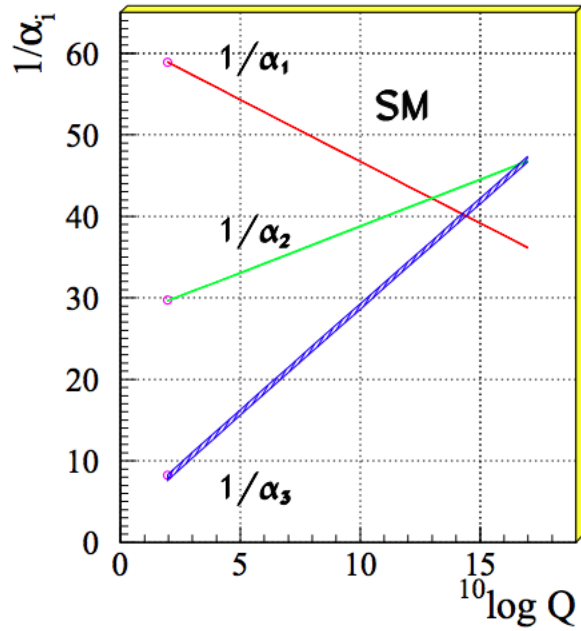


Figure 1.2: Evolution of the inverse of the three coupling constants in the Standard Model as a function of the momentum transferred, [84].

SU(5). The smallest simple group containing $SU(3)_C \otimes SU(2)_T \otimes U(1)_Y$ is SU(5), as shown first by Georgi and Glashow in [67]. Quarks and leptons in this group fit the $\bar{5}$ and 10 representations. The representation for left-handed fermions are the following

$$\bar{5} = (\nu_e, e^-)_L + \bar{d}_L \quad (1.13)$$

$$10 = e_L^+ + \bar{u}_L + (u, d)_L, \quad (1.14)$$

³⁹⁹ while the boson structure gains a new couple of super heavy bosons (X,Y)

$$24 = \underbrace{(8, 1)}_{\text{gluons}} + \underbrace{(1, 3) + (1, 1)}_{W^\pm, Z, \gamma} + \underbrace{(3, 2) + (\bar{3}, 2)}_{X, Y \text{ bosons}}. \quad (1.15)$$

⁴⁰⁰ Nice features such as charge quantization and the identity between the positron
⁴⁰¹ and proton charge value come directly from the group structure. The new super
⁴⁰² heavy bosons are colored and form a weak doublet. Their are the mediator of the
⁴⁰³ interaction that turns quarks into leptons, leading to predict the existence of processes
⁴⁰⁴ that violate baryon number, such as $p \rightarrow \pi^0 + e^+$ (see fig 1.8, right). The prediction
⁴⁰⁵ for proton decay lifetime, $\tau_p \sim \frac{M_X^4}{m_p^5} \sim 10^{30 \pm 1.5}$ years, is unfortunately experimentally
⁴⁰⁶ disproved by IMB and Super-Kamiokande [4, 28].

⁴⁰⁷ **SO(10).** More complicated group structures, such as SO(10) are still viable
⁴⁰⁸ candidates for GUT. SO(10) includes the same type of X and Y bosons as SU(5).
⁴⁰⁹ Right-handed massive neutrinos are embedded in the construction of the irreducible
⁴¹⁰ representation of SO(10). Different patterns of SO(10) symmetry breaking to recover
⁴¹¹ the SM are possible and lead to different predictions for the proton decay lifetime;
⁴¹² some of these predictions are not excluded by the experiments [85].

⁴¹³ **SUSY GUTs.** Supersymmetry theories allow for another family of GUTs. In
⁴¹⁴ SUSY, every fundamental particle in the SM has a “superpartner”, identical in each
⁴¹⁵ quantum number except for the spin-statistics: the fermion supersymmetric partners
⁴¹⁶ are bosons and vice versa. Collider experiments (mainly LHC) constrain the mass of
⁴¹⁷ the supersymmetric partners to be very heavy [?]. The SU(5), SU(10) groups with
⁴¹⁸ a SUSY twist are the basic groups for SUSY GUTs. From the phenomenology point
⁴¹⁹ of view, SUSY models tend to push the proton decay life time higher by a factor of
⁴²⁰ four, they solve the “hierarchy problem”, and they also predict new channels for the
⁴²¹ proton decay. In particular they predict the presence of kaons in the final product,
⁴²² with a dominant mode of $p \rightarrow K^+ \bar{\nu}$. Predictions on the proton decay lifetime depend

423 on the chosen SUSY model; again, some of the predictions are not excluded by the
424 experiments [88, 89, 108].

425 **1.4 Motivations for Hadronic Cross Sections in Ar- 426 gon**

427 Critical challenges await the next decade of high energy physics at the intensity
428 frontier. Following the recommendation of the latest Particle Physics Project Priori-
429 tization Panel [105], the US is dedicating substantial resources to the development of
430 a short- and long- baseline neutrino program to address many of open questions in
431 neutrino physics today. This program pivots on the Liquid Argon Time Projection
432 Chamber (LArTPC) detector technology which will be described in Chapter 2.

433 The main goals of these research programs include:

- 434 - the assessment of the existence of right-handed sterile neutrinos via the study
435 of accelerator neutrinos on a short baseline (SBN),
- 436 - the determination of the sign of Δm_{13}^2 (or Δm_{23}^2), i.e., the neutrino mass hier-
437 archy via the study of accelerator neutrinos on a long baseline (DUNE),
- 438 - the determination of the octant, i.e. whether θ_{23} is maximal, via the study of
439 accelerator neutrinos on a long baseline (DUNE),
- 440 - the determination the status of CP symmetry in the lepton sector, via the study
441 of accelerator neutrinos on a long baseline (DUNE),
- 442 - the search for observables predicted by GUTs, such as proton decay via the
443 study of non accelerator physics in massive underground detectors (DUNE).

444 1.4.1 Pion-Argon Total Hadronic Cross Section

445 This section outlines the importance of the pion-argon total hadronic cross section in
446 the context of the current and upcoming liquid argon neutrino experiments, SBN and
447 DUNE. We describe the signal signature and historic measurements of pion-nucleus
448 cross section, as well as the implementation of these cross sections in the current
449 version of the simulation package used by LArIAT.

450 π^- -Ar Cross Section in the Context of Neutrino Searches

451 As outlined in 1.2.3, neutrino experiments use the products of neutrino interactions
452 to identify the energy and flavor of the incoming neutrino. Pions are a common
453 product of neutrino interaction, especially in resonant scattering, DIS and coherent
454 pion production. For neutrino experiments in argon, there are two main reasons
455 why understanding pion hadronic interactions with argon is important: to model the
456 behavior of the pion inside the target nucleus and to model the behavior of the pion
457 during its propagation inside the detector medium.

458 Assumptions on the nuclear modeling and on the interaction of hadrons inside the
459 nucleus performed at the level of the neutrino event generator bridge the measure-
460 ment of the products of a neutrino interaction to the reconstruction of the neutrino
461 energy and flavor. Thus, understanding pion hadronic interactions with the nucleus is
462 particularly important to model correctly resonant, DIS and coherent pion production
463 in neutrino interactions. For example, in case of resonant scattering,

$$\nu_l + N \rightarrow l + \Delta/N^* \rightarrow l + \pi + N', \quad (1.16)$$

464 the Δ and N^* and excited states will decay hadronically in matters of $\sim 10^{-24}$ s
465 inside the nucleus producing pions which will have many chances to re-interact
466 as they exit the target medium. The decay modes for the lower mass Δ (1232) and

467 $N^*(1440)$ are listed in table 1.3.

468 The key elements of a neutrino event generators for resonance and DIS events
469 are the nuclear model and the hadron treatment (both production and transporta-
470 tion). We illustrate here the conceptual basis of the GENIE Neutrino Generator [18]
471 as an example, since GENIE is one the most popular event generators for liquid ar-
472 gon experiments. For example, the nuclear model used by GENIE for all processes
473 is a Relativistic Fermi Gas (RFG) model modified to incorporate nucleon-nucleon
474 correlations [30]. This means that the initial momentum and binding energy of the
475 struck nucleon is determined by assuming nucleons inside the nucleus are quasi-free,
476 acting independently in the mean field of the nucleus. For $A > 20$ such as argon, the
477 2-parameter Woods-Saxon shell model for density function is used. The GENIE mod-
478 ule INTRANUKE [83] is used to simulate final-state interactions (FSI) which model
479 hadron re-interactions inside the nucleus. This module places the outgoing parti-
480 cles in the nucleus and propagates them using the “hA model”. In the INTRANUKE
481 hA model, hadrons can undergo at most one FSI per event. When possible, external
482 hadron-nucleus scattering data are used to tune INTRANUKE. Since no data is avail-
483 able for Argon, GENIE uses an interpolation of data from heavier and lighter nuclei
484 for the pion-argon cross section leading to large (10?s of %) resultant uncertainties in
485 the INTRANUKE module.

486 Once the pion has left the target nucleus, the pion-argon hadronic cross section also
487 plays an important role in the pion transportation inside the argon medium: processes
488 such as pion absorption or pion charge exchange can greatly modify the topology of
489 a neutrino interactions in the detector and lead to significant modifications in the
490 event classification. Being able to reconstruct the details of pions inside the detector
491 is an imperative for modern liquid argon neutrino experiment to achieve the design
492 resolution for their key physics measurements.

493 **π^- -Ar Hadronic Interaction: Signal Signatures**

494 Strong hadronic interaction models [48, 68] predict the pion interaction processes with
495 argon in the [100 - 1200] MeV energy range. The total hadronic π^- -Ar interaction
496 cross section is defined as the one related to the single process driven only by the
497 strong interaction which is dominant in the considered energy range. In measuring
498 the “total” cross section, we include both the elastic and reaction channels, regardless
499 of the final state,

$$\sigma_{Tot} = \sigma_{Elastic} + \sigma_{Reaction}; \quad (1.17)$$

500 the reaction channel is further characterized by several exclusive channels with defined
501 topologies,

$$\sigma_{Reaction} = \sigma_{Inelastic} + \sigma_{abs} + \sigma_{chex} + \sigma_{\pi prod}. \quad (1.18)$$

502 A summary of the pion final states in order of pion multiplicity for the reaction
503 channel is given in table 1.4. Pion capture and pion decay at rest dominate the
504 cross section under 100 MeV. We define pion capture as the process determining the
505 formation of a pionic atom and the subsequent pion’s end of life. Stopping negative
506 pions can form pionic argon, where the negative pion plays the role of an orbital
507 electron. Since the pion mass is two orders of magnitude greater than the electron
508 mass, the spatial wave form of the pion will overlap more with the nucleus compared
509 to the electron case. After the electromagnetic formation of the pionic atom, the
510 pion will get quickly absorbed by the nucleus, which is put in an excited state. The
511 nucleus then de-excites with the emission of low energy nucleons and photons. Pion
512 capture is dominant compared to pion decay, the other important process for very
513 low energy pions. The decay of a pion is governed by the weak force; the pion decay
514 life time is $\tau_\pi = 2.6 \times 10^{-8}$ s and the main decay mode is $\pi^- \rightarrow \mu^- + \bar{\nu}_\mu$ (BR 99.98%).
515 Since pion capture can be considered an electromagnetic process and pion decay is a
516 weak process, this energy region is purposely excluded from the hadronic cross section

517 measurement.

518 **Previous measurements: Lighter and Heavier Nuclei**

519 Many experiments with pion beams have studied the hadronic interaction of pions on
520 light and heavy materials, such as He, Li, C, Fe, Pb [36]. However, data on argon are
521 rare: the total differential hadronic cross section has never been measured before on
522 argon. Simulation packages such as Geant4 base their pion transportation for argon
523 on data from lighter and heavier nuclei: the goal of LArIAT’s dedicated measurement
524 on argon is to bridge this gap in data, thus reducing the uncertainties related to pion
525 interactions in argon in both neutrino event generators and in simulation packages of
526 pion transportation.

527 The shape of the pion-nucleus interaction cross section in the energy range con-
528 sidered shows the distinct features indicating the presence of a resonance. In fact, the
529 mean free path of a pion of kinetic energy between 100 and 400 MeV is much shorter
530 than the average distance between nucleons (which is of the order of 1 fm). There-
531 fore, the pion interacts with surface nucleons. A Δ resonance is often produced in
532 the interaction, which subsequently decays inside the nucleus. Experimental results
533 on several nuclei as reported in [36] are shown in Figure 1.3; it is interesting to notice
534 here how the shape of the Δ resonance becomes less pronounced as a function of the
535 mass number of the target nucleus. Pion interactions with heavier nuclei also shift the
536 peak of the resonance at lower energy; this effect is due to kinematic considerations
537 and to the difference in propagation of the Δ inside the nucleus. Multiple scattering
538 effect modify the resonance width, which is larger than the natural-decay width. As
539 an example of a fairly well studied target, Figure 1.4 reports the negative pion cross
540 section on Carbon for the elastic and reaction² channels, and their sum [54].

2. This paper calls “inelastic interaction” what we refer as to “reaction channel”.

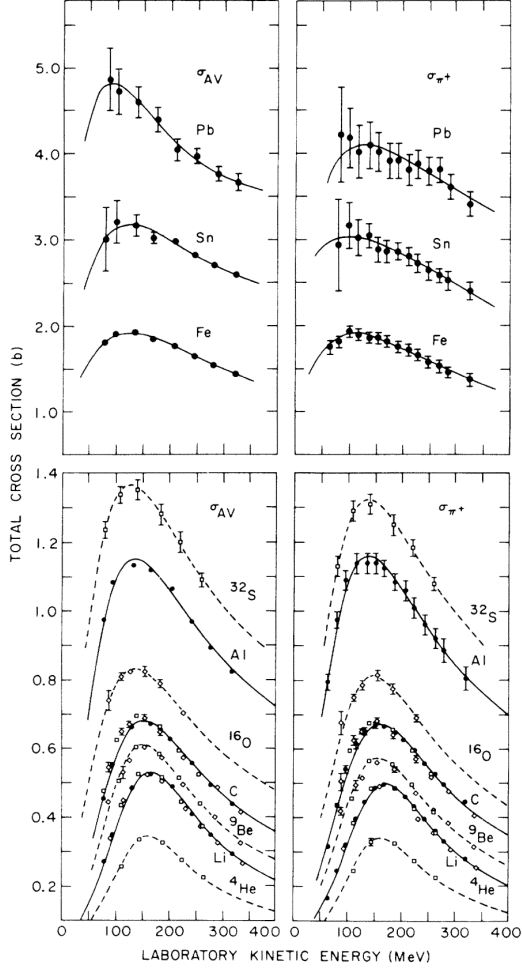


Figure 1.3: Pion-nucleus total cross sections: σ_{π^+} for positive pions (right) and σ_{AV} (left) for the average between positive and negative pions $\sigma_{AV} = \frac{\sigma_{\pi^+} + \sigma_{\pi^-}}{2}$ in the Δ resonance region. The error bars include estimates of systematic uncertainties. The curves are the results of fits to the data assuming a Breit-Wigner shape. This summary plot is reported in [36] and uses data from [51, 115].

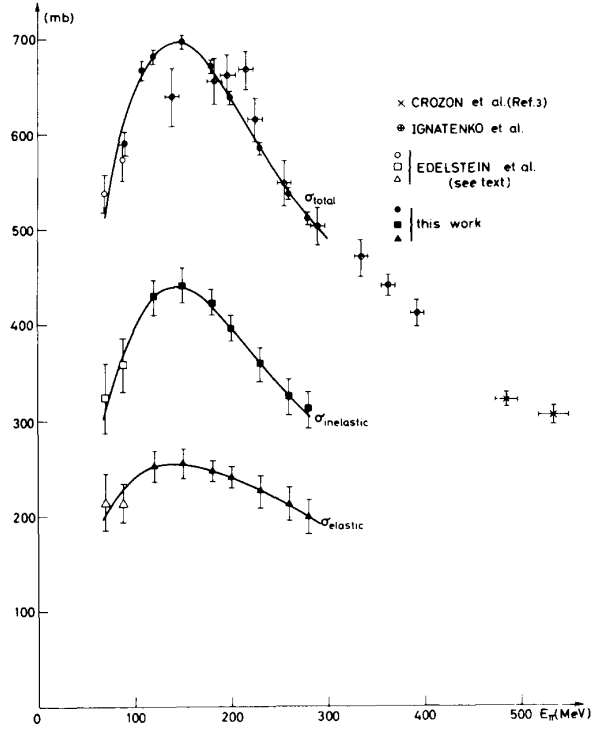


Figure 1.4: Negative pion nucleus total, elastic and reaction cross sections on ^{12}C as from [54].

541 Negative Pion Interaction Cross Section in Simulation Packages

542 LArIAT uses Geant4 as the default simulation package. In particular, pions (and
 543 kaons) transportation is achieved through the Geant4 FTFP_BERT physics list. In
 544 this physics list, Geant4 uses the Bertini cascade model [116] to simulate the products
 545 of the pion-nucleus interaction as well as secondary hadronic re-interactions inside
 546 the target nucleus (intra-nuclear cascade). The target nucleus is represented as a
 547 continuous gas where the nuclear potential follows concentrical shells whose depths
 548 approximate the Woods-Saxon shape. The CERN-HERA compilations [112, 113] of
 549 hadron-nucleon interaction data is the data base used for the decision making process
 550 after the cascade is invoked. The cross section model determines if the pion inter-
 551 acts, the eventual type of interaction and the interaction multiplicity. For hadron
 552 projectiles with energy less than 20 GeV, Geant4 reports the uncertainty on the cross

553 section model to be about the size of the error bars on the data used, or about 10%,
554 increasing to 20-30% in energy regions where data is sparse.

555 The relevance of the GENIE generator for neutrino physics and its basic working
556 principles have been outlined earlier in this section. Given GENIE’s modularity,
557 information on hadron-nucleus interactions can be extracted from the INTRANUKE
558 module and directly compared against the Geant4 predictions. The work in [96]
559 reviews the current status of negative and positive pion simulation in Geant4 and
560 GENIE for ^{12}C , ^{56}Fe , and ^{40}Ca . From that work, we report the results for ^{12}C in
561 Figure 1.5 as it allows a direct comparison between Geant4, GENIE and and pion
562 re-scattering data. Geant4 predictions for π^- on Carbon are in good agreement with
563 data over the entire spectrum spectrum, while GENIE predictions seem to show some
564 features at around 500 MeV and 900 MeV, maybe due to higher resonances in the hA
565 model. From the same work, we also report the negative pion cross section on ^{40}Ca
566 in Figure 1.6, since this is the nuclear medium closest to argon. The predictions from
567 both Geant4 and GENIE agree with data in the high energy region; the Geant4 and
568 GENIE predictions diverge in the resonance region, where data is not available. These
569 few examples highlight how cross section data for the specific nucleus considered in
570 the neutrino experiments is fundamental to inform the Monte Carlo simulation.

571 For the LArIAT simulation of the MC sample used in the π^- argon total hadronic
572 cross section measurement we use the Geant4 Bertini Cascade model, whose predic-
573 tions for the total, elastic and reaction hadronic cross sections are show in Figure
574 1.7.

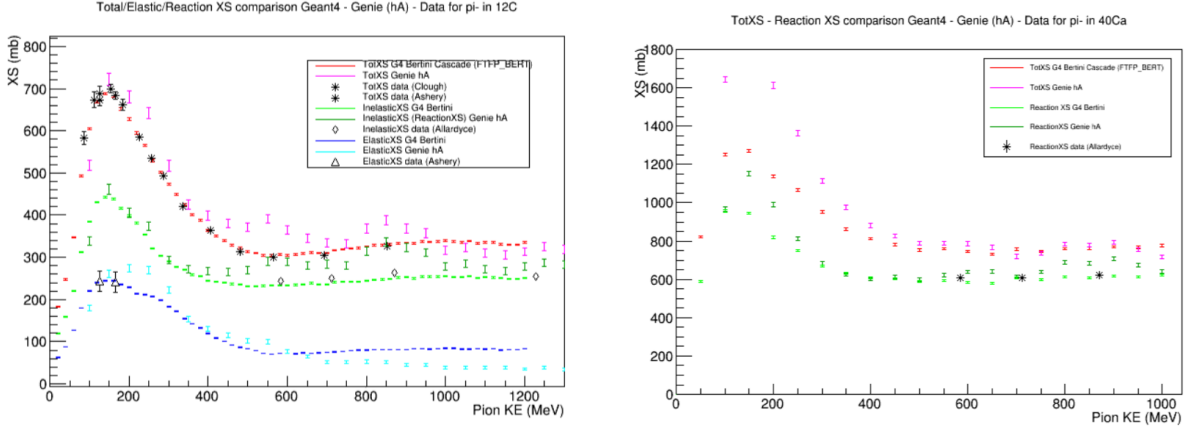


Figure 1.5: Total, elastic and reaction cross section for π^- on ^{12}C . Comparison between results from Geant4 simulation (Bertini cascade model), Genie simulation (hA model), and experimental data [22, 51, 52, 107].

Figure 1.6: Total, elastic and reaction cross section for π^- on ^{40}Ca . Comparison between results from Geant4 simulation (Bertini cascade model), Genie simulation (hA model), and experimental data [52].

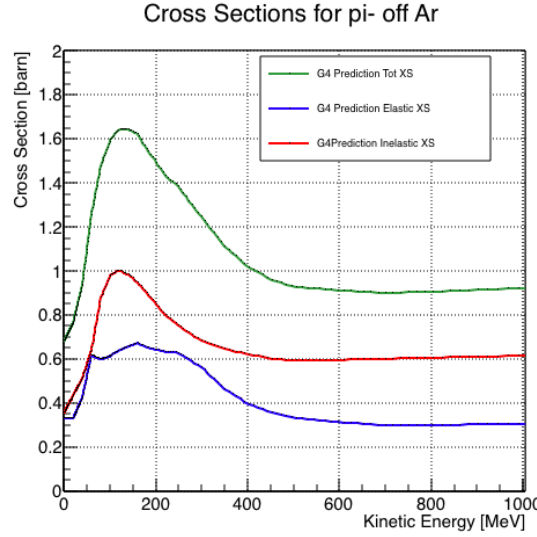


Figure 1.7: Total, elastic and reaction hadronic cross section for π^- -argon implemented in Geant4 10.01.p3.

Resonance	Decay Mode	Lifetime (s)
Δ (1232) $3/2^+$	$\Delta^{++}(\text{uuu}) \rightarrow p\pi^+$ $\Delta^+(\text{uud}) \rightarrow n\pi^+$ $\Delta^+(\text{uud}) \rightarrow p\pi^0$ $\Delta^0(\text{udd}) \rightarrow n\pi^0$ $\Delta^0(\text{udd}) \rightarrow p\pi^-$ $\Delta^-(\text{ddd}) \rightarrow n\pi^-$	$\sim 5.6 \times 10^{-24}$
N^* (1440) $1/2^+$	$N^* \rightarrow N\pi$ $N^* \rightarrow N\pi\pi$	$\sim 2.2 \times 10^{-24}$

Table 1.3: Main decay modes of the lightest Delta resonance and Nucleon excited state.

N π in FS	Channel Name	Reaction	Notes
0	Pion Absorption, σ_{abs}	$\pi^-(np) \rightarrow nn$ (2-body abs) $\pi^-(nnp) \rightarrow nnn$ (3-body abs) $\pi^-(npp) \rightarrow pnn$ (3-body abs) $\pi^-(nnpp) \rightarrow pmn$ (Multi-body abs)	Suppressed on single nucleon by energy conservation: the process occurs on at least two nucleons system.
1	Elastic Scattering, σ_{el}	$\pi^- + N \rightarrow \pi^- + N$	Scattering on nucleon or nucleus, the target is left in ground state
1	Charge Exchange, σ_{chea}	$\pi^- + p \rightarrow \Delta^0 \rightarrow \pi^0 + n$ $\pi^- + N \rightarrow \pi^+ + \text{nucleons}$	Single charge exchange: charged pion converts into neutral pion Double charge exchange: charged pion converts into opposite charge pion
1	Inelastic Scattering, σ_{inel}	$\pi^- + p \rightarrow \Delta^0 \rightarrow \pi^- + p$ (knock-out) $\pi^- + n \rightarrow \Delta^- \rightarrow \pi^- + n$ (knock-out)	Other possible reactions: Pure Inelastic scattering: population of low energy bound excited states Nuclear break-up with nucleons or fragments knock-out
2+	Pion Production, $\sigma_{\pi prod}$	$\pi^- + N \rightarrow \geq 2\pi + \text{nucleons}$	Possible if pion K.E ≥ 500 MeV/c

Table 1.4: Summary of negative pion hadronic interactions of the reaction channel as a function of the pion multiplicity in the final state in the energy range [100-1200] MeV.

575 1.4.2 Kaon-Argon Total Hadronic Cross Section

576 This section outlines the importance of the kaon-argon total hadronic cross section.
577 We start by discussing the measurement in the context of nucleon decay searches. We
578 then describe the signal signature and historical measurements of kaon-nucleus cross
579 section, as well as the implementation of this cross sections in the current version of
580 the simulation package used by LArIAT.

581 **K⁺Ar Cross section in the Context of Nucleon Decay Searches**

582 Baryon number is accidentally conserved in the Standard Model. Even though no
583 baryon number violation has been experimentally observed thus far, no underlying
584 symmetry in line with the Noether paradigm [95] explains its conservation. As shown
585 in section 1.3.2, almost all Grand Unified Theories predict at some level baryon num-
586 ber violation in the form of nucleon decay on long time-scales. Given the impossibil-
587 ity to reach grand unification energy scales with collider experiments (Energy Scale
588 $> 10^{15}$ GeV), an indirect proof of GUTs is needed. The experimental observation of
589 nucleon decay may be the only viable way to explore these theories.

590 In case of nucleon decay discovery, the dominant decay mode may uncover addi-
591 tional information about the GUT type. Supersymmetric GUTs [24, 45] prefer the
592 presence of kaons in the products of the decay, e.g. $p \rightarrow K^+ \bar{\nu}$ (see fig 1.8, left).
593 Gauge mediated GUTs, in which new gauge bosons are introduced that allow for the
594 transformation of quarks into leptons, and vice versa, prefer the mode $p \rightarrow e^+ \pi^0$ (see
595 fig 1.8, right).

596 LArIAT tiny active volume makes it impossible for the experiment to place com-
597 petitive limits on nucleon decay searches. However, LArIAT provides excellent data
598 to characterize kaons in liquid argon for the “LAr golden mode”, $p \rightarrow K^+ \bar{\nu}$. The
599 result of these studies will affect future proton decay searches in LArTPCs. Previous
600 work has been done to assess the potential identification efficiency for different decay

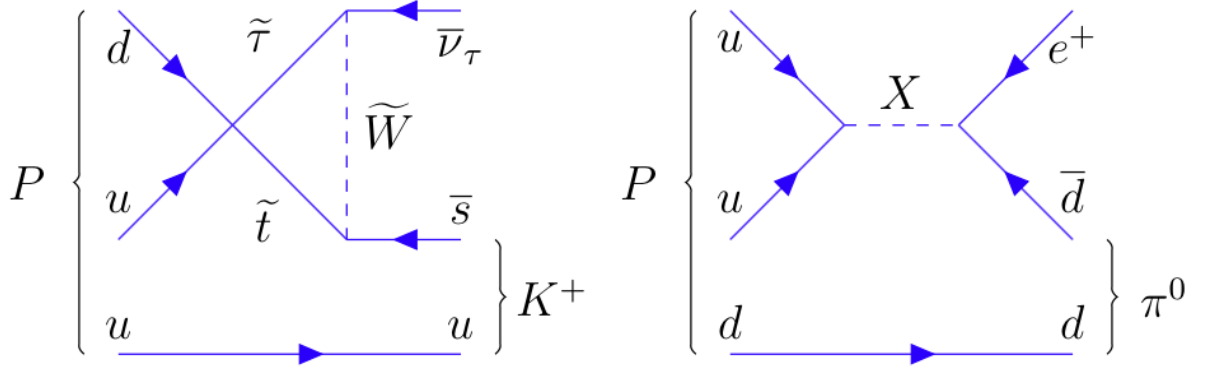


Figure 1.8: Feynman diagrams for proton decay “golden modes”: $p \rightarrow K^+\bar{\nu}$ for supersymmetric GUTs on the left and $p \rightarrow e^+\pi^0$ for gauge-mediated GUTs on the right.

601 modes in a LArTPC [50], but, as the time of this writing, no study of kaon selection
 602 efficiency in LArTPCs has been performed on data. The K^+ -Ar interaction cross
 603 section has never been measured before and can affect the possibility of detecting
 604 and measuring kaons when produced in a proton decay event. Kaon interactions with
 605 argon can distort the kaon energy spectrum as well as change the topology of single
 606 kaon events. In a LArTPC, non-interacting kaons appear as straight tracks with a
 607 high ionization depositions at the end (Bragg peak). The topology of interacting
 608 kaons can be quite different. In case of elastic scattering, a distinct kink will be
 609 present in the track. In case of inelastic scattering the Bragg peak will not be present
 610 and additional tracks will populate the event. Performing the total hadronic K^+ -Ar
 611 cross section measurement on data serves the double purpose of identifying the rate
 612 of “unusual” topologies (kinks and additional tracks) and of developing tools for kaon
 613 tracking in LAr.

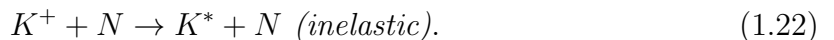
614 **K^+ Ar Hadronic Interaction: Signal Signatures**

The interaction of a mildly relativistic charged kaon with an argon nucleus is determined largely by the strong force. The total hadronic K^+ -Ar interaction cross section

is defined as the one related to the single (hadronic) process driven only by the strong interaction. In this case, “total” indicates all strong interactions regardless of the final state. This condition purposefully includes both elastic and inelastic (reaction) channels. Indeed, the total cross section section can be then decomposed into

$$\sigma_{Tot} = \sigma_{Elastic} + \sigma_{Reaction}.$$

615 For the LArIAT cross section analysis, the kaons considered span a momentum
 616 inside the TPC from 100 MeV/c to 800 MeV/c. In this energy range, the relevant
 617 K-Nucleon interactions are according to [62]:



618 **Previous Measurements: Lighter and Heavier Nuclei**

619 In general, measurements on kaon cross sections are extremely scarce. The mea-
 620 surement of the kaon interaction cross section would bring the additional benefit
 621 of reducing the uncertainties associated with hadron interaction models adopted in
 622 MC simulations for argon targets, beneficial for both proton decay studies and kaon
 623 production from neutrino interaction studies, where the uncertainties for final state
 624 interaction models are big [46].

625 Figure 1.9 shows a 1997 measurement on several elements as performed by Fried-
 626 mann et al. [64]. As a reference, this paper measures a σ_{Tot} for Si of 366.5 ± 4.8
 627 mb and a σ_{Tot} for Ca of 494.6 ± 7.7 mb at 488 MeV/c. The cross section for argon

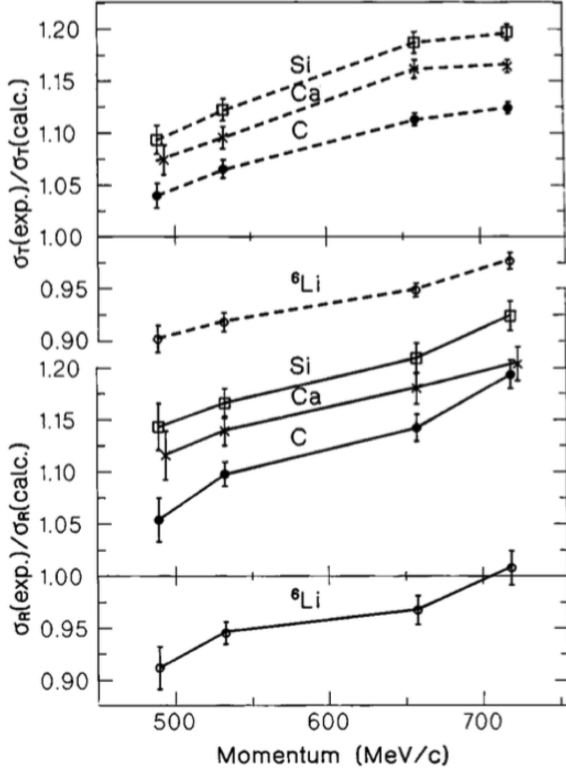


Figure 1.9: Ratios between experimental and calculated cross sections as from [64].
Top: Total cross sections.
Bottom: reaction cross sections.

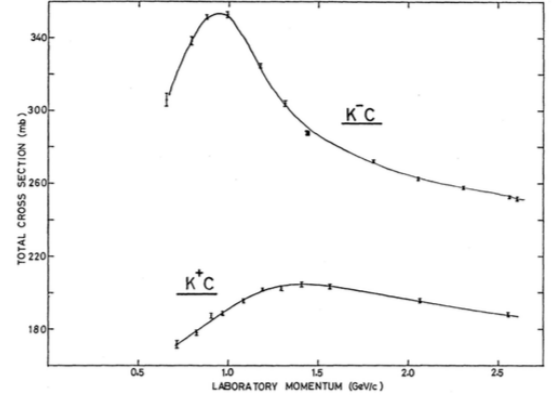


Figure 1.10: Total K^+ and K^- cross sections on carbon as from [32].

is expected to lie in between these two measurements. Additional data on the kaon cross section are provided by Bugg et al. [32]. Bugg performs a measurement of the total K^+ and K^- cross sections on protons and deuterons over the range of 0.6-2.65 GeV/c, as well as a measurement of the total K^+ and K^- cross sections on carbon for a number of momenta; the results of this paper on carbon are reported in Figure 1.10.

634 **Kaon Interaction Cross Section for thin target in Geant4**

Since the kaon cross section in argon has never been measured before, simulation packages tune kaon transportation in argon by extrapolation from lighter and heavier nuclei. LArIAT uses the Geant4 suite for particle transportation. Since kaon data on

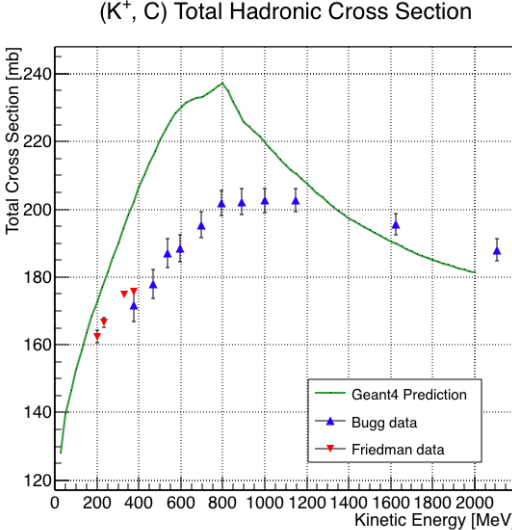


Figure 1.11: Total hadronic cross section for carbon implemented in Geant4 10.01.p3 with overlaid with the Bugg and Friedman data.

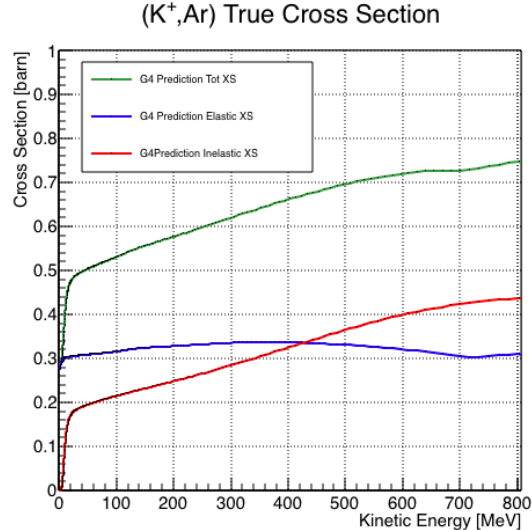


Figure 1.12: Total, elastic and reaction hadronic cross section for K^+ -argon implemented in Geant4 10.01.p3.

carbon are available, we used it as a metric to evaluate the Geant4 prediction performances. Figure 1.11 shows the total hadronic cross section for carbon implemented in Geant4 10.01.p3 overlaid with the Bugg and Friedman data. Unfortunately, version 10.01.p3³ of Geant4, which is the version used for the simulation in this work, does not reproduce the data for carbon closely. On one hand, this evidence makes us even more wary when using the Monte Carlo in simulating the kaon-argon interactions. On the other, it further highlights the importance of the kaon measurement. For the LArIAT simulation of the MC sample used in the K^+ argon total hadronic cross section measurement we use the Geant4 Bertini Cascade model, whose predictions for the total, elastic and reaction hadronic cross sections are shown in Figure 1.12.

3. It should be noted that the latest Geant4 version, 10.03.p3, uses a different parametrization for the kaon cross section and retrieves a better agreement with data.

648 **Chapter 2**

649 **Liquid Argon Detectors at the**
650 **Intensity Frontier**

651 “Beat-up little seagull, on a marble stair
652 Tryin’ to find the ocean, lookin’ everywhere.”
653 – Nina Simone, Baltimore, 1978 –

654 In the next few years, LArTPCs will be the tools to answer some of the burning
655 questions in neutrino physics today. This section illustrates the operational principles
656 of this detector technology, as well as the scope of the key detectors in the US liquid
657 argon program – SBN, DUNE and LArIAT.

658 **2.1 The Liquid Argon Time Projection Chamber**
659 **Technology**

660 **2.1.1 TPCs, Neutrinos & Argon**

661 David Nygren designed the first Time Projection Chamber (TPC) in the late 1970s [97]
662 for the PEP-4 experiment, a detector apt to study electron-positron collisions at the

663 PEP storage ring at the SLAC National Accelerator Laboratory. From the original
664 design in the seventies – a cylindrical chamber filled with methane gas – the TPC
665 detector concept has seen many incarnations, the employment of several different
666 active media and a variety of different particle physics applications, including, but
667 not limited to the study of electron/positron storage rings (e.g. PEP4, TOPAZ,
668 ALEPH and DELPHI), heavy ions collisions in fixed target and collider experiments
669 (e.g. EOS/HISSL and ALICE), dark matter (ArDM), rare decays and capture (e.g.
670 TRIUMF, MuCap), neutrino detectors and nucleon decay (ICARUS, SBN, DUNE),
671 and neutrino less double beta decay (Next). A nice review of the history of TPCs
672 and working principles is provided in [76].

673 Several features of the TPC technology make these detectors a more versatile tool
674 compared to other ionization detectors and explain such a wide popularity. TPCs are
675 the only electronically read detector which deliver simultaneous three-dimensional
676 track information and a measurement of the particle energy loss. Leveraging on both
677 tracking and calorimetry, particle identification (PID) capabilities are enhanced over
678 a wide momentum range.

679 Historically, the active medium in ionization detectors has been in the gaseous
680 form. Carlo Rubbia first proposed the use of a Liquid Argon TPC for a neutrino
681 experiment, ICARUS [106], in 1977. Using nobles elements in the liquid form for
682 neutrino detectors is advantageous for several reasons. The density of liquids is ~ 1000
683 times greater than gases, augmenting the number of targets for neutrino's interaction
684 in the same volume, in a effort to balance the smallness of neutrino cross section. Since
685 the energy loss of charged particle is proportional to the target material density, as
686 shown in the Bethe-Block equation (eq. 2.1), the increased density reflects into a
687 proportionally higher energy loss, enhancing the calorimetry capability of detectors
688 with a liquid active medium. Additionally, the ionization energy of liquids is smaller
689 than gasses by the order of tens of eV. Thus, at the passage of charged particles,

Element	LAr	LXe
Atomic Number	18	54
Atomic weight A	40	131
Boiling Point Tb at 1 atm	87.3 K	165.0 K
Density	1.4 g/cm ³	3.0 g/cm ³
Radiation length	14.0 cm	2.8 cm
Moliere Radius	10.0 cm	5.7 cm
Work function	23.6 eV	15.6 eV
Electron Mobility at $E_{field} = 10^4$ V/m	0.047 m ² /Vs	0.22 m ² /Vs
Average dE/dx MIP	2.1 MeV/cm	3.8 MeV/cm
Average Scintillation Light Yield	40000 γ /MeV	42000 γ /MeV
Scintillation λ	128 nm	175 nm

Table 2.1: LAr, LXe summary of properties relevant for neutrino detectors.

liquids generally produce more ionization electrons than gases for the same deposited energy, forcing the particles to deposit more energy in a shorter range. The downside of using noble liquid elements in experiments is that they require expensive cryogenic systems to cool the gas until it transitions to its the liquid form. The properties of liquid argon in comparison liquid xenon – a popular choice for dark matter and neutrinoless double beta decay detectors – are summarized in table 2.1. Albeit xenon would be more desirable than argon given some superior properties such as lower ionization energy and higher density and light yield, argon relative abundance abates the cost of argon compared to xenon, making argon a more viable choice for the construction of ton (and kilo-ton) scale neutrino detectors.

LArTPCs are some times referred as to “electronic” bubble-chambers, for the similarity in the tracking and energy resolution which is coupled with an electronic readout of the imaging information in LArTPCs. Compared to these historic detectors however, LArTPC bestow tridimensional tracking and a self triggering mechanism provided by the scintillation light in the liquid argon. An event display of a ν_μ CC interaction candidate in the MicroBooNE detector is shown in picture 2.1 to display the level of spatial details these detectors are capable of; the color scale of the image is proportional to the energy deposited, hinting to these calorimetry capabilities of

the detectors.

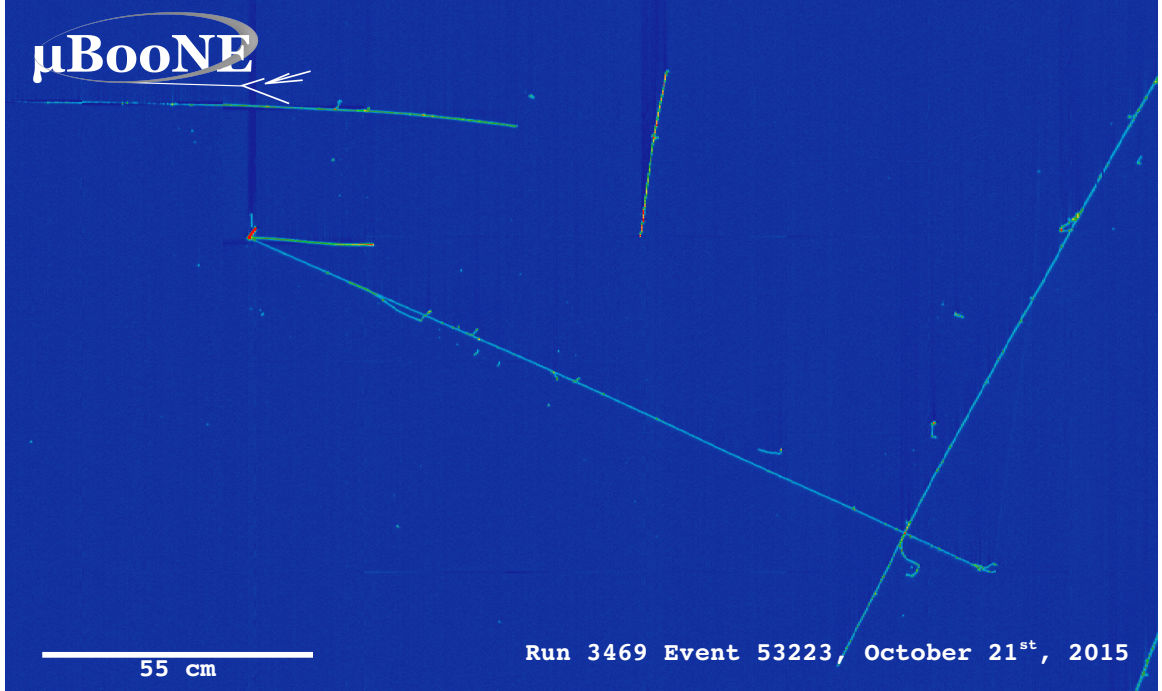


Figure 2.1: Event display of a ν_μ CC interaction candidate in the MicroBooNE detector.

708

709 2.1.2 LArTPC: Principles of Operation

710 To the bare bones, a LArTPC is a bulk of liquid argon sandwiched in a flat capacitor,
711 equipped with a light collection system, as the cartoon in 2.2 shows. A uniform
712 electric field of the order of 500 V/cm is maintained constant between the faces of the
713 capacitor. The anode is sensitive to ionization charge and it is usually made of two
714 or more planes segmented into several hundreds parallel sense wires a few millimeters
715 apart; different geometries for the anode segmentation are under study [47].

716 Argon ionization and scintillation are the processes leveraged to detect particles
717 in the LArTPC active volume. When a ionizing radiation traverses the argon active
718 volume it leaves a trail of ionization electrons along its trajectory and it excites
719 the argon producing scintillation light – details on the production and detection of
720 ionization charge and scintillation light are provided in 2.1.4 and 2.1.4 respectively.

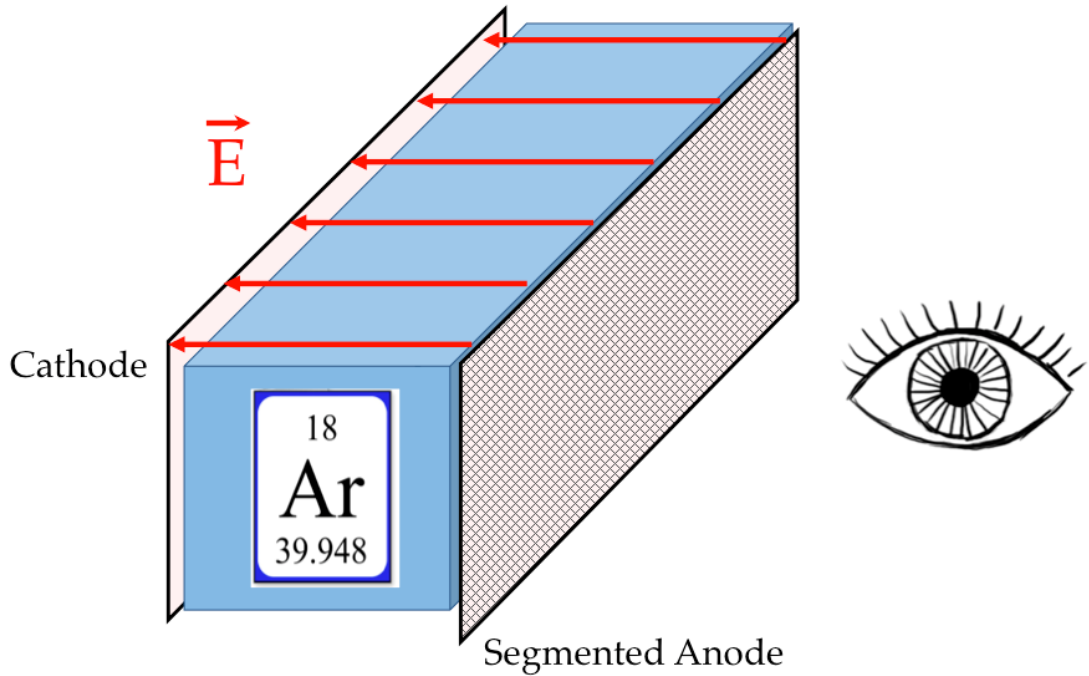


Figure 2.2: A cartoonish sketch of a LArTPC.

721 The optical detector sees the argon scintillation light in matters of nanoseconds.
 722 This flash of light determines the start time of an event in the chamber, t_0 . The
 723 uniform electric field drifts the ionization electrons from the production point towards
 724 the anode in order of hundreds of microseconds or more depending on the chamber
 725 dimensions¹. The anode sense wires see either an induced current by the drifting
 726 ionization charge (on induction planes) or an injection of such charge (collection
 727 plane). An appropriate choice of the voltage bias on each wire plane assures ideal
 728 charge transparency, so that all the ionization charge is collected on the collection
 729 plane and none on the induction planes.

730 The arrival time of the charge on the anode sense wires is used to measure the
 731 position of the original ionizing radiation in the drift direction. In fact, since the

1. The ionized argon also drifts, but in the opposite directions compared to the electrons. Since the drift time is proportional to the particle mass, the ions' drift time is much longer than the electrons'. Ionized argon is collected on the cathode which is not instrumented, so it is not used to infer information about the interactions in the chamber.

constant electric field implies that the drift velocity is also constant, the position of
 the original ionization is simply given by the multiplication of the drift velocity by the
 drift time, where the “drift time” is the difference between t_0 and the charge arrival
 time on the wire planes. The spacial resolution on this dimension is limited by the
 time resolution of the electronics or by longitudinal diffusion of the electrons. The
 spatial information on the different wire planes maps a bi-dimensional projection of
 the interaction pattern in the plane perpendicular to the drift direction. The spacial
 resolution on this dimension is limited by the transverse electron diffusion in argon
 and by the grain of the anode segmentation, i.e. the spacing between the wires in
 the sense planes [44]. The off-line combination of the 2-D information on the wire
 planes with the timing information allows for the 3D reconstruction of the event in
 the chamber.

Since the charge deposited by the ionizing radiation is proportional to the de-
 posited energy and the charge collected on the sense plane is a function of the de-
 posited charge, LArTPCs allow the measurement of the energy deposit in the active
 volume. Effects due to the presence of free charge and impurities in the active vol-
 ume, such as a finite electron lifetime, recombination and space charge, complicate
 the relationship between deposited and collected charge affecting the measurement of
 the particle’s energy, as described in the next section.

2.1.3 Liquid Argon: Ionization Charge

The mean rate of energy loss by moderately relativistic elementary charge particles
 heavier than electrons is well described by the modified Bethe-Bloch [100] equation

$$-\frac{dE}{dx} = K z^2 \frac{Z}{A} \varrho \frac{1}{\beta^2} \left[\frac{1}{2} \ln \frac{2m_e c^2 \beta^2 \gamma^2 T_{max}}{I^2} - \beta^2 - \frac{\delta}{2} \right], \quad (2.1)$$

754 where z is the number of unit charge of the ionizing radiation, Z , A and ϱ are the
 755 atomic number, mass number and density of the medium, m_e is the electron mass,
 756 $\gamma = \frac{\beta}{\sqrt{1-\beta^2}}$ is the Lorentz factor of the ionizing radiation, T_{max} is the maximum kinetic
 757 energy which can be imparted to a free electron in a single collision, I is the mean
 758 excitation energy on eV, δ is the density correction and $K = 0.307075 \text{ MeV g}^{-1} \text{ cm}^2$ is
 759 a numerical conversion factor. The Bethe-Bloch treats the energy loss by an ionizing
 760 radiation via quantum-mechanical collisions producing ionization or an excitation in
 761 the medium as an uniform and continuous process. The density correction terms
 762 becomes relevant for incident particle with high energy, where screening effects due
 763 to the polarization of the medium by high energy particles occur.

764 Excitation and ionization of the detector medium occur in similar amounts. Since
 765 the ionizing collisions occur randomly, we can parametrize their number k in a segment
 766 of length s along the track with a Poissonian function

$$P(k) = \frac{s^k}{k! \lambda^k} e^{-s/\lambda}, \quad (2.2)$$

767 where $\lambda = 1/N_e \sigma_i$, with N_e being the electron density of σ_i the ionization cross-
 768 section per electron. About 66% of the ionizing collisions in Argon produce only
 769 a single electron/ion pair [76]; in the other cases, the transferred kinetic energy is
 770 enough for the primary electron to liberate one or more secondary electrons, which
 771 usually stay close to the original pair. Occasionally, electrons can receive enough
 772 energy to be ejected with high energy, forming a so-called “ δ -ray”: a detectable short
 773 track off the particle trajectory, as shown in figure 2.3. The average number of δ -ray
 774 with energy $E > E_0$ per cm follows the empirical form

$$P(E > E_0) \sim \frac{y}{\beta^2 E_0}, \quad (2.3)$$

775 where y is an empirical factor depending on the medium (0.114 for gaseous Ar), and

776 β is v/c .

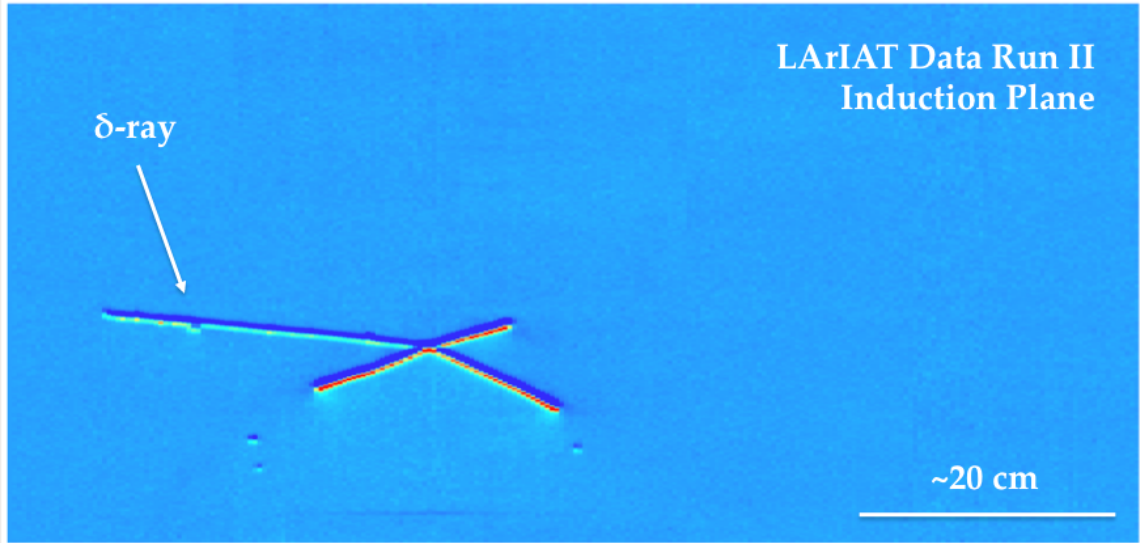


Figure 2.3: Events display for a LArIAT pion absorption candidate on the induction plane, with highlighted delta ray.

777 Purity & Electron Life Time

778 The presence of electronegative contaminants in liquid argon, such as oxygen O_2
779 and water H_2O , is particularly pernicious, since these molecules quench the charge
780 produced by the ionizing radiation. Thus, amount of charge per unit of length dQ/dx
781 collected on the collection plane depends on the charge's production point in the
782 detector: ionization produced close to the cathode will see more impurities along its
783 journey to the collection plane than ionization produced close to the anode, resulting
784 in greater attenuation of its charge. As a result, the amount of charge collected on
785 the sense wires as a function of the traveled distance follows an exponential decay
786 trend. The traveled distance is generally measured in terms of drift time and the
787 characteristic time constant of the exponential decay is called electron lifetime τ_e .
788 Figure 2.4 shows the typical life time for LArIAT data. The procedure to measure
789 the electron lifetime in LArIAT is outlined in [103]. LArIAT small drift distance (47
790 cm) allows for a relatively short electron life time. The life time for bigger detectors

such as MicroBooNE, whose drift distance is 2.6 m, needs to be of the order of tens of milliseconds to allow a charge collection usable for physics analyses. Energy reconstruction in LArTPC applies a correction for the finite lifetime to calibrate the detector calorimetric response; details for LArIAT are provided in Section 5.6.1.

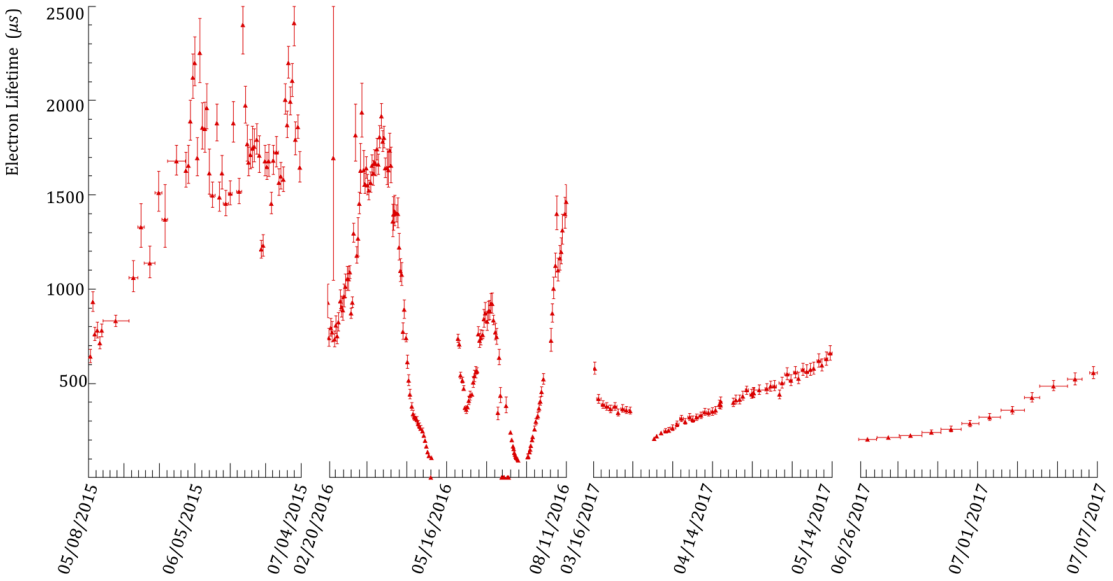


Figure 2.4: Electron lifetime during the LArIAT run period [42].

LArTPCs use hermetically sealed and leak-checked vessels to abate the leakage and diffusion of contaminants into the system. The liquid argon filling of the volume occurs after the vessel is evacuated or purged with gaseous argon [10] to reduce remaining gases in the volume. Even so, the construction of a pure tank of argon is unviable, as several sources of impurity remain. In particular, impurities can come from the raw argon supply, the argon filtration system and from the outgassing from internal surfaces. Outgassing is a continuous diffusive process producing contami-

nants, especially water, even after the vessel is sealed, particularly from materials in the ullage region². Since research-grade argon comes from the industrial distillation of air, the impurities with the highest concentration are nitrogen, oxygen and water, generally maintained under the 1 part per million level by the vendor. Even so, a higher level of purity is necessary to achieve a free electron life time usable in meter scale detectors. Thus, argon is constantly filtered in the cryogenic system, which reduce the oxygen and water contamination to less than 100 parts per trillion. The filtration system depends on the size and drift distance of the experiment and, for experiments on several meters scale, it includes an argon recirculation system.

811 Recombination Effect

812 After production, ionization electrons thermalize with the surrounding medium and
813 may recombine with nearby ions. Recombination might occur either between the
814 electron and the parent ion through Coulomb attraction, as described in the geminate
815 theory [98], or thanks to the collective charge density of electrons and ions from
816 multiple ionizations in a cylindrical volume surrounding the particle trajectory, as
817 described in the columnar model [79]. Consideration on the average electron-ion
818 distance and the average ion-ion distance for argon show that the probability of
819 geminate recombination is low; thus recombination in argon is mainly due to collective
820 effects [5]. Since protons, kaons and stopping particles present a higher ionization
821 compared to MIPs, recombination effects are more prominent when considering the
822 reconstruction of energy deposited by these particles.

823 Theoretical descriptions of recombination based on the Birks model and the Box
824 model are provided in [29] and [111], respectively. The Birks model assumes a gaussian
825 spatial distribution around the particle trajectory during the entire recombina-

2. While the liquid argon low temperature reduces outgassing in the liquid, this process remains significant for absorptive material (such as plastic) above the surface of the liquid phase.

826 tion phase and identical charge mobility for ions and electrons. The Box model also
827 assumes that electron diffusion and ion mobility are negligible in liquid argon during
828 recombination. In these models, the fraction of ionization electrons surviving recom-
829 bination is a function of the number of ion-electron pairs per unit length, the electric
830 field, the average ion-electron separation distance after thermalization and the angle
831 of the particle with respect to the direction of the electric field – plus the diffusion
832 coefficient in the Birks model. Given the stringent assumptions, it is perhaps not sur-
833 prising that these models are in accordance to data only in specific regimes: the Birks
834 model is generally used to describe recombination for low dE/dx , the Box model for
835 high dE/dX . In LArTPC, the ICARUS and ArgoNeut experiments have measured
836 recombination in [16] and [5] respectively. Since LArIAT uses the refurbished Ar-
837 goNeut TPC and cryostat at the same electric field, LArIAT currently corrects for
838 recombination using the ArgoNeut measured recombination parameters in [5].

839 Space Charge Effect

840 Slow-moving positive argon ions created during ionization can build-up in LArTPC,
841 causing the distortion of the electric field within the detector. This effect, called
842 “space charge effect” leads to a displacement in the reconstructed position of the
843 signal ionization electrons. In surface LArTPCs the space charge effect is primarily
844 due to the rate of ionization produced by cosmic rays which is slowly drifting in the
845 chamber at all times. Surface LArTPC of the size of several meters are expected
846 to be modestly impacted from the space charge effect, where charge build-up create
847 anisotropy of the electric field magnitude of the order of 5% at a drift field of 500
848 V/cm [92]. The smallness of the LArIAT drift volume and its relatively high electric
849 field are such that the effect of space charge is expected to be negligible.

850 **2.1.4 Liquid Argon: Scintillation Light**

851 Liquid argon emits scintillation light at the passage of charged particles. LArTPCs
852 leverage this property to determine when the ionization charge begins to drift towards
853 the anode plane.

854 **Scintillation Process**

855 Scintillation light in argon peaks in the ultraviolet at a 128 nm, shown in comparison
856 to Xenon and Kypton in Figure 2.5, from [93]. The light yield collected by the optical
857 detector depends on the argon purity, the electric field, the dE/dx and particle type,
858 averaging at the tens of thousands of photons per MeV.

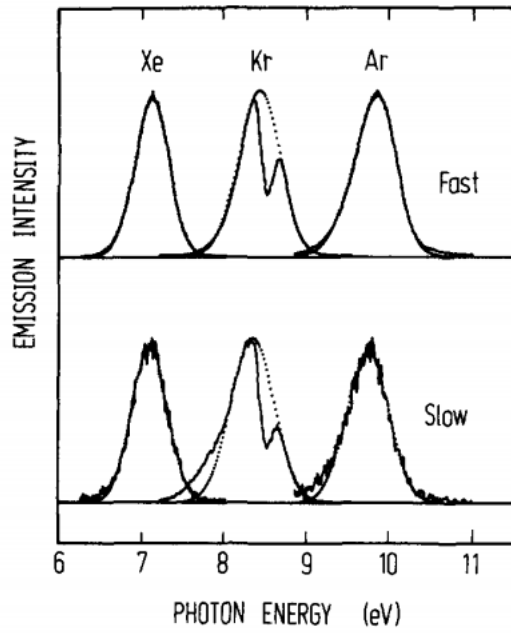


Figure 2.5: Emission spectra of the fast and slow emission components in Xenon, Kypton and Argon according to [93]. The dotted lines correspond to the Gaussian fits.

859 The de-excitation of Rydberg dimers in the argon is responsible for the scintillation
860 light. Rydberg dimers exist in two states: singlets and a triplets. The time constant
861 for the singlet radiative decay is 6 ns, resulting in a prompt component for the scin-

tillation light. The decay of the triplet is delayed by intersystem crossing, producing a slow component with a time constant of ~ 1500 ns. “Self-trapped exciton luminescence” and “recombination luminescence” are the two processes responsible for the creation of the Rydberg dimers [82]. In the first process, a charged particle excites an argon atom which becomes self-trapped in the surrounding bulk of argon, forming a dimer; the dimer is in the singlet state 65% of the times and in the triplet state 35% of the times. In case of recombination luminescence, the charged particle transfers enough energy to ionize the argon. The argon ion forms a charged argon dimer state, which quickly recombines with the thermalized free electron cloud. Excimer states are produced in the recombination, roughly half in the singlet and half in the triplet state. The light yield dependency on the electric field, on the dE/dx and particle type derives from the role of free charge in the recombination luminescence process. The spacial separation between the argon ions and the free electron cloud depends on the electric field. On one hand, a strong electric field diminishes the recombination probability, leading to a smaller light yield; on the other, it increases the free charge drifting towards the anode plane. Hence, the amount of measurable charge and light anti-correlates as a function of the electric field. Ionizing particles in the argon modify the local density of both free electrons and ions depending on their dE/dx . Since the recombination rate is proportional to the square of the local ionization density, highly ionizing particles boost recombination and the subsequent light yield compared to MIPs. The possibility to leverage this dependency for pulseshape-based particle identification has been shown in [31, 87].

Effects Modifying the Light Yield

The production mechanism through emission from bound excimer states implies that argon is transparent to its own scintillation light. In fact, the photons emitted from these metastable states are not energetic enough to re-excite the argon bulk, greatly

888 suppressing absorption mechanisms. In a LArTPC however, several processes modify
889 the light yield in between the location where light is produced and the optical detector.
890 In a hypothetical pure tank of argon, Rayleigh scattering would be the most important
891 processes modifying the light yield. Rayleigh scattering changes the path of light
892 propagation in argon, prolonging the time between light production and detection.
893 The scattering length has been measured to be 66 cm [77] , shorter than the theoretical
894 prediction of \sim 90 cm [110]; this value is short enough to be relevant for the current
895 size of LArTPCs detectors. In fact, Rayleigh scattering worsen the resolution on t_0 ,
896 the start time for charge drifting, and alters the light directionality, complicating the
897 matching between light and charge coming from the same object in case of multiple
898 charged particles in the detector.

899 Traces of impurities in argon such as oxygen, water and nitrogen also affect the
900 light yield, mainly via absorption and quenching mechanisms. Absorption occurs as
901 the interaction of a 128 nm photon directly with the impurity dissolved in the liquid
902 argon. Differently, quenching occurs as the interaction of an argon excimer and an
903 impurity, where the excimer transfers its excitation to the impurity and dissociates
904 non-radiatively. Given this mechanism, it is evident how quenching is both a function
905 of the impurity concentrations and the excimer lifetime. Since the triplet states
906 live much longer than the singlet states, quenching occurs mainly on triplet states,
907 affecting primarily the slow component of the light, reducing the scintillation yield
908 and a shortening of the scintillation time constants.

909 The stringent constraints for the electron life time limit the presence of oxygen and
910 water to such a low level that both absorption and quenching on these impurity is not
911 expected to be significant. Contrarily, the nitrogen level is not bound by the electron
912 life time constraints – nitrogen being an inert gas, expensive to filter. Thus, nitrogen
913 is often present at the level provided by the vendor. The effects of nitrogen on argon
914 scintillation light have been studied in the WArP R&D program and at several test

915 stands. The quenching process induced by nitrogen in liquid Ar has been measured
916 to be proportional to the nitrogen concentration, with a rate constant of ~ 0.11
917 μs^{-1} ppm $^{-1}$; appreciable decreasing in lifetime and relative amplitude of the slow
918 component have been shown for contamination as high as a few ppm of nitrogen [6].
919 For a nitrogen concentration of 2 parts per million, typical of the current generation
920 of LArTPC, the attenuation length due to nitrogen has been measured to be ~ 30
921 meters [81].

922 Wavelength Shifting of LAr Scintillation Light

923 Liquid argon scintillation light is invisible for most optical detectors deployed in a
924 LArTPC, such as cryogenic PMTs and SiPMs, since a wavelength of 128 nm is gen-
925 erally too short to be absorbed from most in glasses, polymers and semiconductor
926 materials. Research on prototype SiPMs absorbing directly VUV light and their
927 deployment in noble gasses experiment is ongoing but not mature [118]. Thus, ex-
928 periments need to shift the wavelength of scintillation light to be able to detect it.
929 Albeit deployed in different ways, neutrinos and dark matter experiments commonly
930 use 1,1,4,4-tetraphenyl-butadiene (TPB) to shift the scintillation light. TPB absorbs
931 the vacuum ultraviolet (VUV) light and emits in the visible at ~ 425 nm [33], with
932 a ratio of visible photon emitted per VUV photon absorbed of $\sim 1.2:1$ [65].

933 Neutrino experiments typically coat their optical detector system evaporating a
934 layer of TPB either directly on the PMTs glass surface or on acrylic plates mounted in
935 front of the PMTs [59]; this technique allows the fast detection light coming directly
936 from the neutrino interaction. Dark matter experiments typically evaporate TPB on
937 reflective foils mounted on the inside walls of the sensitive volume and detect the
938 light after it has been reflected; this technique leads to a higher and more uniform
939 light yield, though scattering effects for both the visible and VUV light augment
940 the propagation time and hinder directionality information [60]. In order to take

941 advantage of both these techniques, hybrid systems with PMT coating and foils are
942 being considered for the next generation of large neutrino detectors.

943 **2.1.5 Signal Processing and Event Reconstruction**

944 In this section we illustrate the processing and reconstruction chain of the TPC sig-
945 nals, from the pulses on the sense wire to the construction of three dimensional objects
946 with associated calorimetry. Different experiments can chose different software pack-
947 ages for their off line signal processing and event reconstruction, but a popular choice
948 for US based LArTPCs is LArSoft [39]. Based on the Art framework [71], LArSoft is
949 an event-based toolkit to perform simulation, analysis and reconstruction of LArT-
950 PCs events.

951

952 LArTPC signal processing develops in several consecutive stages that we summa-
953 rize here in the following categories: *Deconvolution, Hit Reconstruction, 2D Cluster-*
954 *ing, 3D Tracking, Calorimetry Reconstruction*. A visualization of the signal processing
955 workflow is shown in figure 2.6.

956

957 **Deconvolution.** Induction and collection planes have different field responses,
958 given the different nature of the signals on these planes: the wires on the induction
959 planes see the inductive signal of the drifting charge, while the wires on the collection
960 planes see the current derived from the charge entering the conductor. Thus, signals
961 on the induction plane are bi-polar pulse and signal on the collection plane are unipo-
962 lar pulses, see Figure 2.6 panel a). The first step in signal processing is deconvolution,
963 that is a series of off-line algorithms geared towards undoing the detector effects. The
964 result of the deconvolution step is the production of a comparable set waveforms on
965 all planes presenting unipolar, approximately gaussian-like pulses (Figure 2.6 panel
966 b)). Signal from all planes are treated on equal footage beyond this point. Some

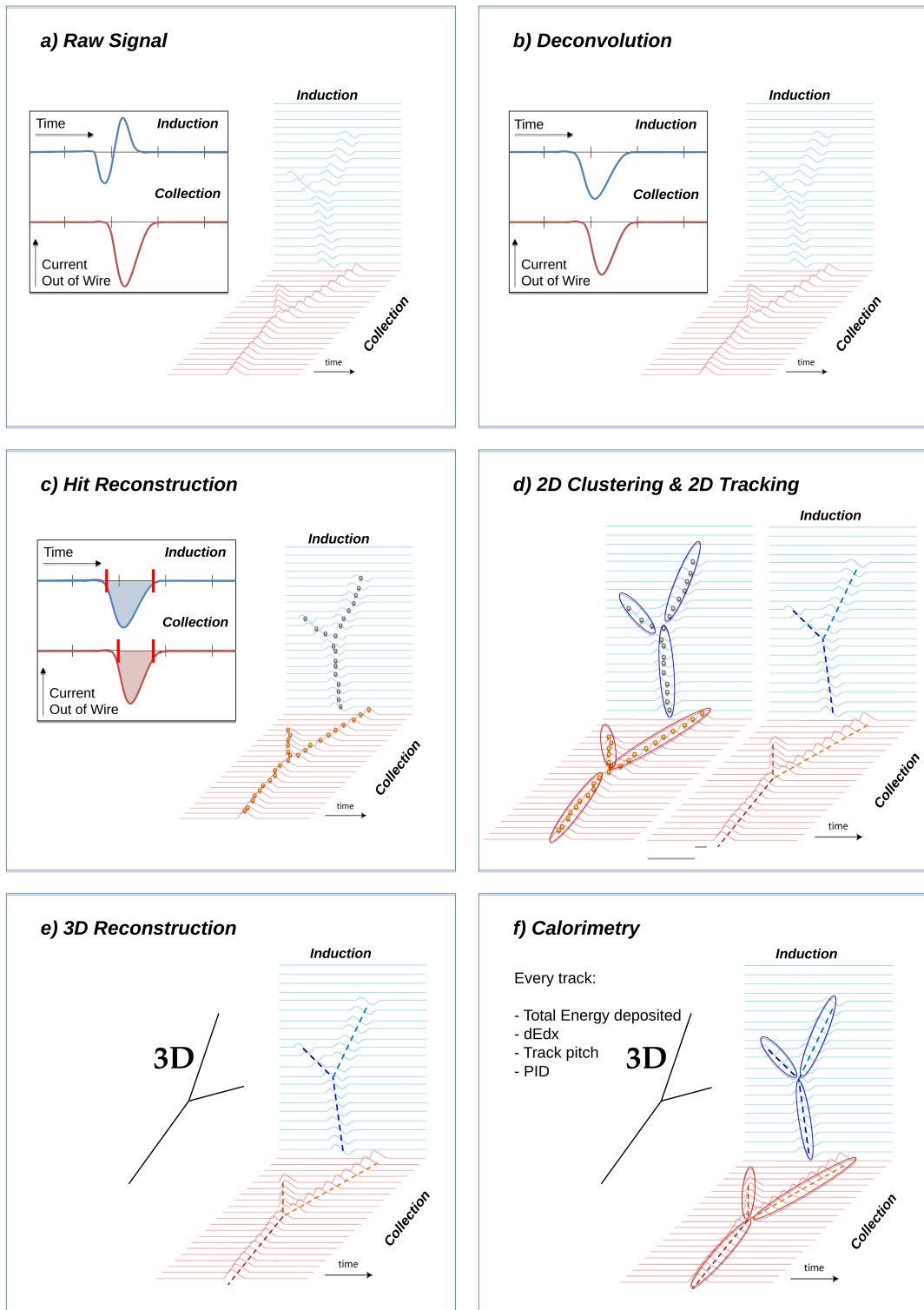


Figure 2.6: A scheme of a typical signal processing workflow in LArSoft.

967 LArTPC apply noise filtering in the frequency domain just after the deconvolution
968 to clean up wire cross talk. Since signals from the LArIAT TPC are extremely clean,
969 noise filtering is not necessary.

970

971 **Hit Reconstruction.** The second stage of the signal processing is the recon-
972 struction of hits, indicating an energy deposition in the detector. A peak finder scans
973 the deconvolved TPC waveforms for each wire on the whole readout time looking for
974 spikes above the waveform’s baseline. It then fits these peaks with gaussian shapes
975 and stores the fit parameters such as the quality of the fit, the peak time, height and
976 area under the gaussian fit. The information resulting from this process on a single
977 spike form a single reconstructed “hit”, see Figure 2.6 panel c). The next steps in
978 the event reconstruction chain will then decide if rejecting hits with poor fits. It is
979 important to notice how the height and width of the hit depend on the topology of
980 the event: for example, a particle running parallel to the wire planes will leave a series
981 of sharp hits on many consecutive wires, while a particle traveling towards the planes
982 will leave a long, wide hit on very few wires. The height of the hits and their integral
983 is proportional to the charge collected on the wire, so it depends on the particle type.

984

985 The event reconstruction chain uses collection of hits to form more complex objects
986 associated with the particles in the detector. The development of different approaches
987 to accomplish this task is an extremely hot topic in LArTPC event reconstruction
988 which spans from more traditional approaches such as line-clustering [26] to the use of
989 machine learning tools [58]. Generally speaking, the scope of hit clustering and event
990 reconstruction to provide shower-like or track like-objects with an associated energy
991 reconstruction. This is because different particles have different topology in the de-
992 tector – electrons and photon create electromagnetic showers, resulting in shower-like
993 topologies, while muons and hadrons leave track-like signals. For the scope of these

994 thesis, we will describe only LArIAT's approach to track reconstruction even if we
995 recognize the breath of LArTPC event reconstruction is much wider. We are inter-
996 ested in the reconstruction of pions and kaons in the active volume, whose topology
997 is track-like.

998

999 **2D Clustering Reconstruction.** The LArIAT reconstruction of track-like ob-
1000 jects starts by clustering hits on the collection and induction planes separately with
1001 the use of the TrajCluster clustering package [25]. TrajCluster looks for a collection
1002 of hits in the wire-time 2D space which can be described with a line-like 2D trajec-
1003 tory. TrajCluster reconstructs trajectories by adding trajectory points to the leading
1004 edge of the trajectory while stepping through the 2D space of hits. Several factors
1005 determine whether a hit is added to the trajectory, including but not limited to

- 1006 1. the goodness of the fit of the single hit,
1007 2. the charge of the hit compared to the average charge and RMS of the hits
1008 already forming the trajectory,
1009 3. the goodness of trajectory fit with and without the hit addition,
1010 4. the angle between the two lines formed by the collection of hits before and after
1011 the considered hit in the trajectory.

1012 The final product of this reconstruction stage is the collection of bidimensional clusters
1013 on each wire plane, see Figure 2.6 panel d).

1014 **3D Tracking.** The 3D tracking set of algorithms uses clusters close in time on
1015 the induction and collection planes as starting point to form a 3D track. Firstly, it
1016 construct a tentative 3D trajectory using the edges of the clusters. Then, it projected
1017 back the tentative trajectory on to the planes and adjusts the parameters of the 3D
1018 track fit such that they minimize the distance between the fit projections and the

1019 track hits in all wire planes simultaneously. Tridimensional tracking can use multiple
1020 clusters in one plane, but it can never break them in smaller groups of hits. This
1021 algorithm was first developed for the ICARUS collaboration [20]. The final product
1022 of this reconstruction stage is the formation of tridimensional objects in the TPC
1023 active volume, see Figure 2.6 panel e).

1024

1025 **Calorimetry.** The last step in the event reconstruction chain is to assign calorimetric
1026 information to the track (or shower) objects. Calorimetry is performed separately
1027 on the different planes. A multi-step procedure is needed to retrieve the energy
1028 deposited in the TPC from the charge seen by the wires. For each hit associated with
1029 the track object, the calorimetry algorithms calculate the charge seen on every wire
1030 using the area underneath the gaussian fit; then, they correct this raw charge by the
1031 electron life time, the electronic noise on the considered wire and the recombination
1032 effect. Lastly an overall calibration of the energy, explained in detail in section 5.6.1,
1033 is applied and the calorimetric information for the given track is assigned. Even if
1034 calorimetry is done in 2D, it benefits from the 3D tracking information; typical information
1035 available after the calorimetric reconstruction are the total energy deposited
1036 by the particle and its stopping power dE/dx at each “track pitch”, i.e. at each 2D
1037 projection on the wire plane of the 3D trajectory.

1038 2.2 The Intensity Frontier Program

1039 2.2.1 Prospects for LArTPCs in Neutrino Physics: SBN and 1040 DUNE

1041 The ArgoNeut experiment [17] initiated the US LArTPC neutrino program. Following
1042 the success of this small TPC on the NuMI beam, a wide program of LArTPCs
1043 on neutrino beams has flourished. The construction of LArTPCs as near and far

1044 detectors at different baseline allows for the exploration of some of the fundamental
1045 questions in neutrino physics today illustrated in section 1.3.1.

1046 The Short-Baseline Neutrino (SBN) [21] program at Fermilab is tasked with con-
1047 clusively assess the nature of the “LSND and MiniBooNE anomalies” [14, 15, 23],
1048 resolving the mystery of sterile neutrinos at the eV² scale. The SBN program entails
1049 three surface LArTPCs positioned on the Booster Neutrino Beam at different dis-
1050 tances from the neutrino production in oder to fully exploit the L/E dependence of
1051 the oscillation pattern: SBND (100 m from the decay pipe), MicroBooNE (450 m),
1052 and ICARUS (600 m). Within the oscillation context, the choice of the LArTPC tech-
1053 nology for the SBN detectors changes the set of systematics with respect to LSND
1054 and MiniBooNE, whose detection techniques were both based on Cherenkov light.
1055 In particular, LArTPCs provide excellent electron/photon separation [9] lacking in
1056 Cherenkov detectors which can be leveraged to abate the photon background from
1057 neutral current interactions in ν_e searches. MicroBooNE [8], the first detector of the
1058 SBN program to be fully operational, started its first neutrino run in October 2015.
1059 MicroBooNE is a 89 ton active volume LArTPC, single drift chamber with TPC di-
1060 mensions of 2.6 m (drift) x 2.3 m (heigh) x 10.4 m (depth). MicroBooNE is positioned
1061 at a very similar L/E on the Booster neutrino beam as MiniBooNE has the scope to
1062 directly cross check the MiniBooNE oscillation measurement. In case MicroBooNE
1063 confirms the presence of the “low energy excess” anomaly, SBND and ICARUS will
1064 provide the full measurement of the oscillation parameters. SBND and ICARUS are
1065 both dual drift chambers, whose active volume is respectively 112 ton and 600 ton.
1066 ICARUS is scheduled to become operational by the end of 2018 and SBND shortly
1067 after. Besides the oscillation analysis, the second main goals of SBN is to perform
1068 an extensive campaign of neutrino cross section measurements in argon. Given the
1069 importance of nuclear effects in (relatively) heavy materials, as discussed in section
1070 1.2.3, both the oscillation analysis of the SBN program and the measurements of

1071 neutrino properties in DUNE will benefit from such a campaign.

1072 On a different neutrino beam and baseline, the DUNE experiment, née LBNE [11],
1073 is the flagship experiment on the medium-long term of US-based neutrino physics,
1074 scheduled to start data taking in 2026. Shooting neutrinos from Fermilab for 800 miles
1075 to the SURF laboratory in South Dakota, DUNE is tasked with performing conclusive
1076 measurements of CP violation in the lepton sector, the neutrino mass ordering and
1077 the θ_{23} octant. The DUNE far detector will count four 10 kton LArTPCs, roughly of
1078 dimensions of 19 m (horizontally) x 18 m (vertically) x 66 m (depth).

1079 **2.2.2 Prospects for LArTPCs in GUT Physics: DUNE**

1080 The experimental exploration of a manifestation of Grand Unified Theory is possible
1081 in DUNE thanks to its sheer mass. In particular, proton decay searches are a capital
1082 topic of DUNE's wide non-accelerator physics program. The key elements for a
1083 rare decay experiment are: massive active volume, long exposure, high identification
1084 efficiency and low background. Figure 2.7 shows the current best experimental limits
1085 on nucleon decay lifetime over branching ratio (dots). Historically, the dominant
1086 technology used in these searches has been water Cherenkov detectors: all the best
1087 experimental limits on every decay mode are indeed set by Super-Kamiokande [?,?].
1088 As shown in section 1.3.2, different family of GUTs predict the proton to decay in
1089 different modes. In particular, SUSY flavored GUTs prefer the presence of kaons
1090 in the decay products, e.g. $p \rightarrow K^+ \bar{\nu}$. It is particularly important to notice that
1091 the kaon energy for the proton decay mode $p \rightarrow K^+ \bar{\nu}$ is under Cherenkov threshold
1092 in water. Thus, Super-Kamiokande set the limit on the lifetime for the $p \rightarrow K^+ \bar{\nu}$
1093 mode by relying on photons from nuclear de-excitation and on the muon tagging in
1094 the kaon decay leptonic mode. For this reason, an attractive alternative approach to
1095 identifying nucleon decay is the use of a LArTPCs, where the kaon is directly visible
1096 in the detector. According to [11], DUNE will have an active volume large enough,

1097 have sufficient shielding from the surface, and will run for lengths of time sufficient
 1098 to compete with Hyper-K, opening up the opportunity for the discovery of nucleon
 1099 decay.

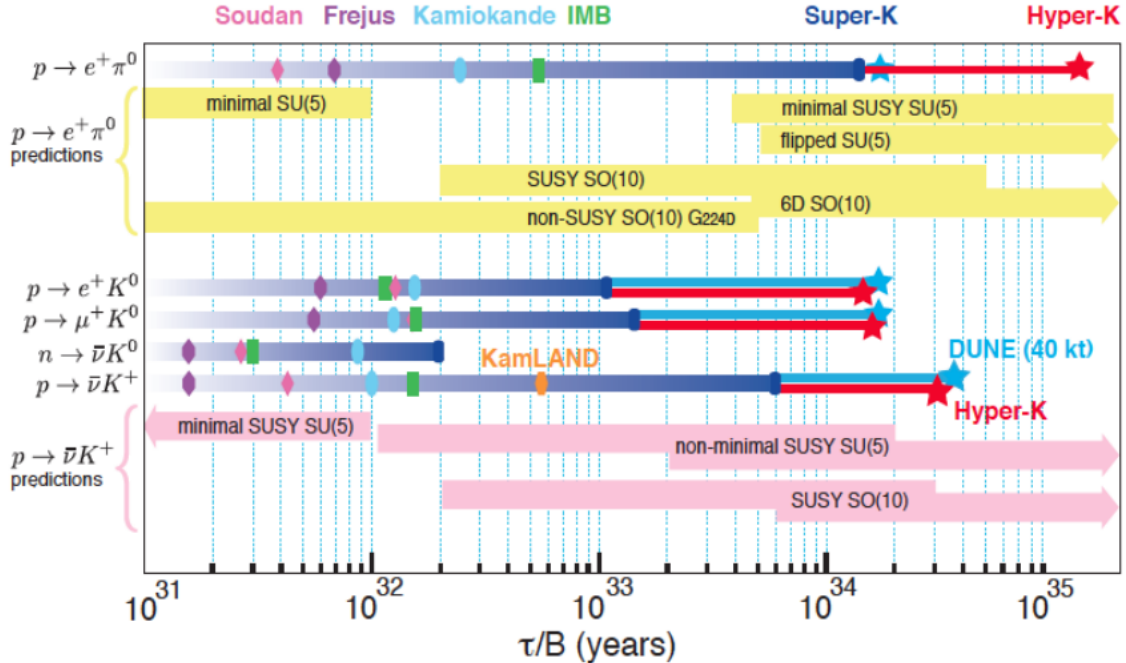


Figure 2.7: Proton decay lifetime limits from passed and future experiments.

1100 2.2.3 Enabling the next generation of discoveries: LArIAT

1101 LArIAT, a small LArTPC in a test beam, is designed to perform an extensive physics
 1102 campaign centered on charged particle cross section measurements while characteriz-
 1103 ing the detector performance for future LArTPCs. Since LArTPCs represent the most
 1104 advanced experiments for physics at the Intensity Frontier, their complex technology
 1105 needs a thorough calibration and dedicated measurements of some key quantities to
 1106 achieve the precision required for the next generation of discoveries. LArIAT's goal
 1107 is to provide such calibration and dedicated measurements. The LArIAT LArTPC is
 1108 deployed in a dedicated calibration test beamline at Fermilab. We use the LArIAT
 1109 beamline to characterize the charge particles before they enter the TPC: the particle

1110 type and initial momentum is known from beamline information. The precise calor-
1111 metric energy reconstruction of the LArTPC technology enables the measurement of
1112 the total differential cross section for tagged hadrons. The Pion-Nucleus and Kaon-
1113 Nucleus total hadronic interaction cross section have never been measured before in
1114 argon and they are a fundamental step to shed light on light meson interaction in nu-
1115 clei per se, while providing a key input to neutrino physics and proton decay studies
1116 in future LArTPC experiments like SBN and DUNE.

1117 In order to showcase LArIAT’s utility to SBN and DUNE, we illustrate briefly
1118 two comparisons as examples: one regarding neutrino interactions and the second
1119 regarding proton decay studies.

1120 The left side of figure 2.8 shows the distribution of products in momentum spectrum
1121 and particle type as simulated in a ν_e CC interaction in DUNE (according to [86]);
1122 the range of these distribution is to compare with the momentum distribution of
1123 light particles in the LArIAT beamline – shown on the right side of figure 2.8. The
1124 momentum spectrum in the LArIAT beamline for electrons, muons and pions – the
1125 most abundant particles produced in a ν_e CC interaction – covers a wide range of the
1126 expected momentum distribution in a neutrino event.

1127 The signature of a proton decay event in the “LAr golden mode” is the presence of
1128 a single kaon of about 400 MeV in the detector; the momentum spectrum of the kaon
1129 pre and post FSI in such an event as simulated by GENIE is shown on the left side
1130 of figure 2.9. The right side of figure 2.9 shows the momentum spectrum of kaons in
1131 the LArIAT beamline. Kaons arriving to the LArIAT TPC are ideal for proton decay
1132 studies, since their momentum in the beamline is just above the typical momentum
1133 for kaons in a proton decay event: the majority of LArIAT kaons slow down in the
1134 TPC enough to enter the desired momentum window.

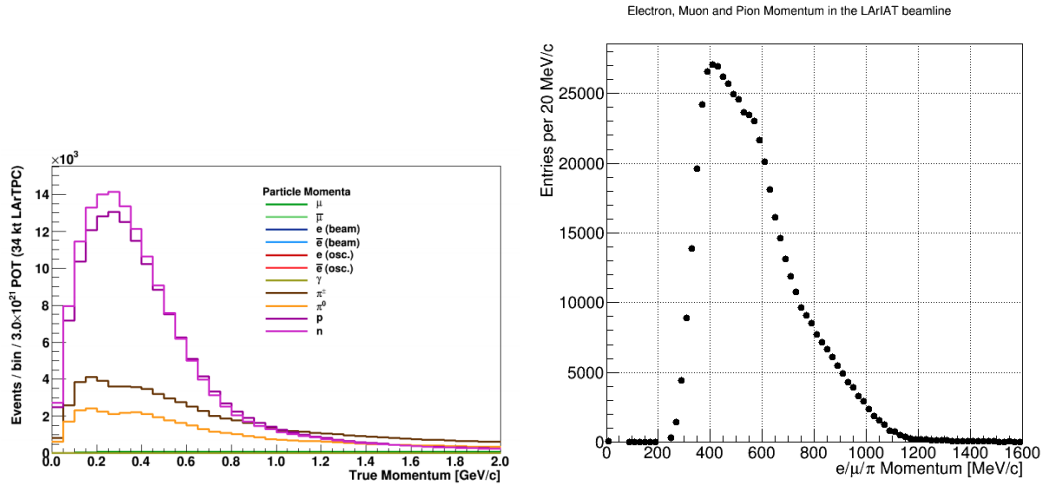


Figure 2.8: *Left.* Simulation of the products of a ν_e CC interaction in DUNE, both in particles type and momentum.
Right. Momentum spectrum for low mass particles (e, μ, π) in the LArIAT beamline, negative tune, Run II, Picky Tracks see section 3.2.2.

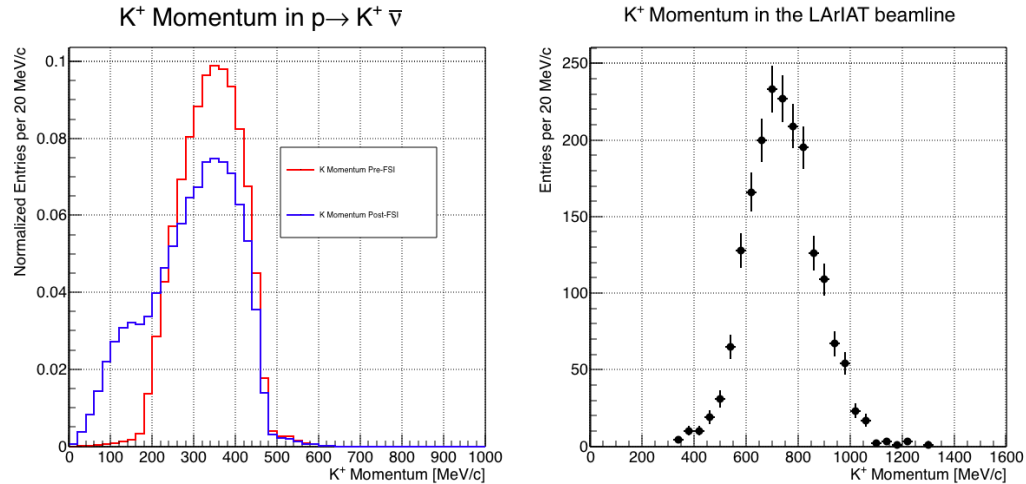


Figure 2.9: *Left.* Momentum of the kaon outgoing a proton decay $p \rightarrow K^+ \bar{\nu}$ event as simulated by the Genie 2.8.10 event generator in argon. The red line represents the kaon momentum distribution before undergoing the simulated final state interaction inside the argon nucleus, while the blue line represents the momentum distribution after FSI.
Right. Positive Kaon momentum spectrum in the LArIAT beamline, positive tune, Run II, Picky Tracks see section 3.2.2.

1135 **Chapter 3**

1136 **LArIAT: Liquid Argon In A**

1137 **Testbeam**

1138 *“But hey we need to be somewhat foolish,
1139 feebleminded, wrong and senseless.”*
1140 – Agnes Obel, Avenue, 2010 –

1141 In this chapter, we describe the LArIAT experimental setup. We start by illus-
1142 trating the journey of the charged particles in the Fermilab accelerator complex, from
1143 the gaseous thermal hydrogen at the Fermilab ion source to the delivery of the LAr-
1144 IAT tertiary beam at MC7. We then describe the LArIAT beamline detectors, the
1145 LArTPC, the DAQ and the monitoring system.

1146 **3.1 The Particles’ Path to LArIAT**

1147 LArIAT’s particle history begins in the Fermilab accelerator complex with a beam of
1148 protons. The process of proton acceleration develops in gradual stages (see picture
1149 3.1): gaseous hydrogen is ionized in order to form H⁻ ions; these ions are boosted
1150 to 750 keV by a Cockcroft-Walton accelerator and injected into the linear accelerator

1151 (Linac) that increases their energy up to 400 MeV; then, H^- ions pass through a
1152 carbon foil and lose the two electrons; the resulting protons are then injected into a
1153 rapid cycling synchrotron, called the Booster; at this stage, protons reach 8 GeV of
1154 energy and are compacted into bunches; the next stage of acceleration is the Main
1155 Injector, a synchrotron which accelerates the bunches up to 120 GeV; in the Main
1156 Injector, several bunches are merged into one and are ready for delivery.

1157 The Fermilab accelerator complex works in supercycles of 60 seconds in duration.
1158 A 120 GeV primary proton beam with variable intensity is extracted in four-second
1159 “spills” and sent to the Meson Center beam line.

1160 LArIAT’s home at Fermilab is the Fermilab Test Beam Facility (FTBF), where
1161 the experiment characterizes a beam of charged particles in the Meson Center beam
1162 line. At FTBF, the primary beam is focused onto a tungsten target to create LAr-
1163 IAT’s secondary beam. The secondary beamline is set such that the composition of
1164 the secondary particle beam is mainly positive pions. The momentum peak of the
1165 secondary beam was fixed at 64 GeV/c for the LArIAT data considered in this work,
1166 although the beam is tunable in momentum between 8-80 GeV/c; this configuration
1167 of the secondary beamline assured a stable beam delivery at the LArIAT experimental
1168 hall.

1169 The secondary beam impinges then on a copper target within a steel collimator
1170 inside the LArIAT experimental hall (MC7) to create the LArIAT tertiary beam,
1171 (shown in Fig. 3.2). The steel collimator selects particles produced with a 13° pro-
1172 duction angle. The particles are then bent by roughly 10° through a pair of dipole
1173 magnets. By configuring the field intensity of the magnets we allow the particles of
1174 LArIAT’s tertiary beam to span a momentum range from 0.2 to 1.4 GeV/c. The
1175 polarity of the magnet is also configurable and determines the sign of the beamline
1176 particles which are focused on the LArTPC. If the magnet polarity is positive the
1177 tertiary beam composition is mostly pions and protons with a small fraction of elec-

Fermilab Accelerator Complex

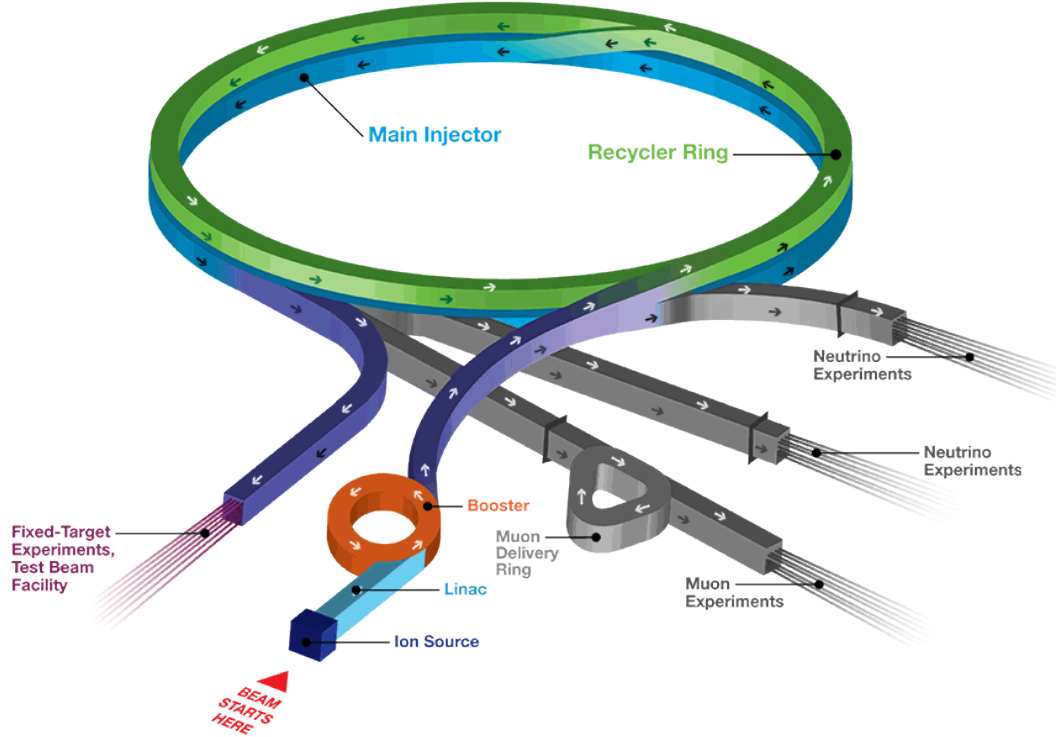


Figure 3.1: Layout of Fermilab Accelerator complex.

1178 trons, muons, and kaons. It is the job of the LArIAT beamline equipment to select the
1179 particles polarity, to perform particle identification in the beamline and to measure
1180 the momentum of the tertiary beam particles before they get to the LArTPC. The
1181 LArIAT detectors are described in the following paragraphs.

1182 3.2 LArIAT Tertiary Beam Instrumentation

1183 The instrumentation of LArIAT tertiary beam and the TPC components have changed
1184 several times during the three years of LArIAT data taking. The following paragraphs
1185 describe the components operational during “Run II”, the data taking period relevant
1186 to the hadron cross section measurements considered in this thesis.

1187 The key components of the tertiary beamline instrumentation for the hadron cross

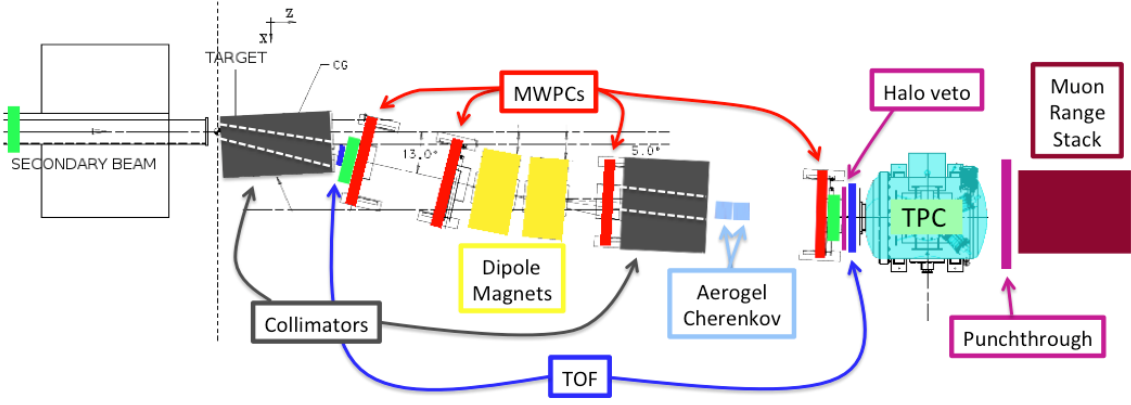


Figure 3.2: Bird’s eye view of the LArIAT tertiary beamline. In grey: upstream and downstream collimators; in yellow: bending magnets; in red: multi wire proportional chambers; in blue: time of flight; in green: liquid argon TPC volume; in maroon: muon range stack.

section analyses are the two bending magnets, a set of four wire chambers (WCs) and two time-of-flight scintillating paddles (TOF) and, of course, the LArTPC. The magnets determine the polarity of the particles in the tertiary beam; the combination of magnets and wire chambers determines the particles’ momenta, which is used to determine the particle species in conjunction with the TOF. A muon range stack downstream from the TPC and two sets of cosmic paddles configured as a telescope surrounding the TPC are also used for calibration purposes. A couple of Aerogel Cherenkov counters, which we will not describe here as they are not used in the hadron cross section measurements, completes the beamline instrumentation.

3.2.1 Bending Magnets

LArIAT uses a pair of identical Fermilab type “NDB” electromagnets, recycled from the Tevatron’s anti-proton ring, in a similar configuration used for the MINERvA T-977 test beam calibration [55]. The magnets are a fundamental piece of the LArIAT beamline equipment, as they are used for the selection of the particle polarity and for the momentum measurement before the LArTPC. The sign of the current in the

1203 magnets allows us to select either positively or negatively charged particles; the value
1204 of the magnetic field is used in the momentum determination and in the subsequent
1205 particle identification.

1206 We describe here the characteristics and response of one magnet, as the second one
1207 has a similar response, given its identical shape and history. Each magnet is a box with
1208 a rectangular aperture gap in the center to allow for the particle passage. The magnet
1209 aperture measures 14.22 cm in height, 31.75 cm in width, and 46.67 cm in length.
1210 Since the wire chambers aperture (~ 12.8 cm 2) is smaller than the magnet aperture,
1211 only the central part of the magnet gap is utilized. The field is extremely uniform
1212 over this limited aperture and was measured with two hall probes, both calibrated
1213 with nuclear magnetic resonance probes. The probes measured the excitation curve
1214 shown in Figure 3.3.

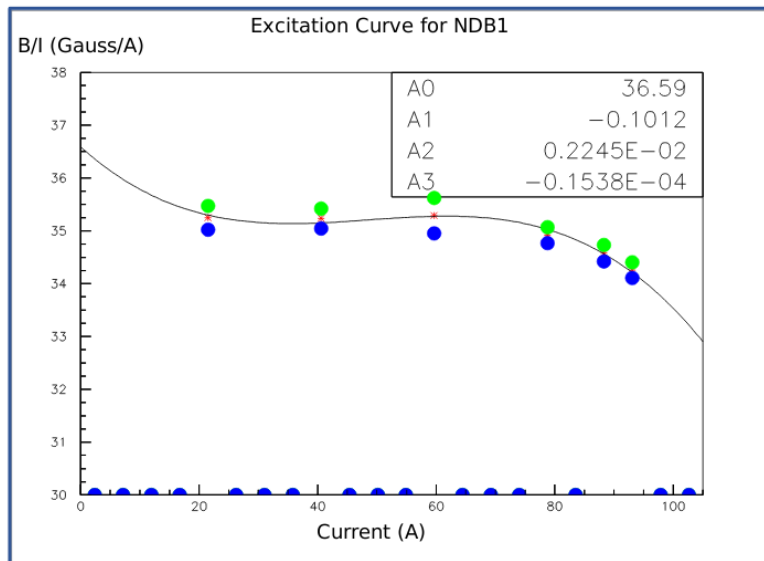


Figure 3.3: Magnetic field over current as a function of the current, for one NDB magnet (excitation curve). The data was collected using two hall probes (blue and green). We fit the readings with a cubic function (black) to average of measurements (red) given in the legend [42].

1215 The current through the magnets at a given time is identical in both magnets.
1216 For the Run II data taking period, the current settings explored were 60A ($B \sim 0.21$
1217 T) and 100A ($B \sim 0.35$ T) in both polarities. Albeit advantageous to enrich the

1218 tertiary beam composition with high mass particles such as kaons, we never pushed
1219 the magnets current over 100 A, not to incur in overheating. During operation, we
1220 operated an air and water cooling system on the magnets and we remotely monitored
1221 the magnet temperatures.

1222 3.2.2 Multi-Wire Proportional Chambers



Figure 3.4: One of the four Multi Wire Proportional Chambers (WC) used in the LArIAT tertiary beamlne and related read-out electronics.

1223 LArIAT uses four multi-wire proportional chambers, or wire chambers (WC) for
1224 short, two upstream and two downstream from the bending magnets. The geometry of
1225 one chamber is shown in Figure 3.4: the WC effective aperture is a square of 12.8 cm
1226 perpendicular to the beam direction. Inside the chamber, the 128 horizontal and 128
1227 vertical wires strung at a distance of 1 mm from each other in a mixture of 85% Argon
1228 and 15% isobutane gas. The WC operating voltage is between 2400 V and 2500 V.
1229 The LArIAT wire chambers are an upgraded version of the Fenker Chambers [61],
1230 where an extra grounding improves the signal to noise ratio of the electronic readout.

1231 Two ASDQ chips [94] mounted on a mother board plugged into the chamber serve
1232 as front end amplifier/discriminator. The chips are connected to a multi-hit TDC [72]
1233 which provides a fast OR output used as first level trigger. The TDC time resolution
1234 is 1.18 ns/bin and can accept 2 edges per 9 ns. The maximum event rate acceptable

1235 by the chamber system is 1 MHz: this rate is not a limiting factor considering that
1236 the rate of the tertiary particle beam at the first wire chamber is estimated to be less
1237 than 15 kHz. A full spill of data occurring once per supercycle is stored on the TDC
1238 board memory at once and read out by a specially designed controller. We use LVDS
1239 cables to carry both power and data between the controller and the TDCs and from
1240 the controller to the rest of the DAQ.

1241 Multi-Wire Proportional Chambers functionality

1242 We use the wire chamber system together with the bending magnets to measure the
1243 particle's momentum.

1244 In the simplest scenario, only one hit on each and every of the four wire chambers
1245 is recorded during a single readout of the detector systems. Thus, we use the hit
1246 positions in the two wire chambers upstream of the magnets to form a trajectory
1247 before the bend, and the hit positions in the two wire chambers downstream of the
1248 magnets to form a trajectory after the bend. We use the angles in the XZ plane
1249 between the upstream and downstream trajectories to calculate the Z component of
1250 the momentum as follows:

$$P_z = \frac{B_{eff}L_{eff}}{3.3(\sin(\theta_{DS}) - \sin(\theta_{US}))}, \quad (3.1)$$

1251 where B_{eff} is the effective maximum field in a square field approximation, L_{eff}
1252 is the effective length of both magnets (twice the effective length of one magnet),
1253 θ_{US} is the angle off the z axis of the upstream trajectory, θ_{DS} is the angle off the
1254 z axis of the downstream trajectory and $3.3 c^{-1}$ is the conversion factor from [T·m]
1255 to [MeV/c]. By using the hit positions on the third and fourth wire chamber, we
1256 estimate the azimuthal and polar angles of the particle trajectory, and we are able to
1257 calculate the other components of the momentum.

1258 The presence of multiple hits in a single wire chamber or the absence of hits in one

1259 (or more) wire chambers can complicate this simple scenario. The first complication
1260 is due to beam pile up, while the latter is due to wire chamber inefficiency. In the
1261 case of multiple hits on a single WC, at most one wire chamber track is reconstructed
1262 per event. Since the magnets bend particles only in the X direction, we assume
1263 the particle trajectory to be roughly constant in the YZ plane, thus we keep the
1264 combination of hits which fit best with a straight line. It is still possible to reconstruct
1265 the particle's momentum even if the information is missing in either of the two middle
1266 wire chambers (WC2 or WC3), by constraining the particle trajectory to cross the
1267 plane in between the magnets.

1268 Events satisfying the simplest scenario of one single hit in each of the four wire
1269 chambers form the “Picky Track” sample. We construct another, higher statistics
1270 sample, where we loosen the requirements on single hit and wire chamber efficiency:
1271 the “High Yield” sample. For LArIAT Run II, the High Yield sample is about three
1272 times the Picky Tracks statistics.

1273 **Four point track momentum uncertainty**

1274 3.2.3 Time-of-Flight System

1275 Two scintillator paddles, one upstream of the first set of WCs and one downstream
1276 of the second set of WCs form LArIAT time-of-flight (TOF) detector system.

1277 The upstream paddle is made of a 10 x 6 x 1 cm scintillator piece, read out by
1278 two PMTs mounted on the beam left side which collect the light from light guides
1279 mounted on all four edges of the scintillator. The downstream paddle is a 14 x 14 x
1280 1 cm scintillator piece read out by two PMTs on the opposite ends of the scintillator,
1281 as shown in figure 3.5. The relatively thin width in the beamline direction minimizes
1282 energy loss of beam particles traveling through the scintillator material.

1283 The CAEN 1751 digitizer is used to digitize the TOF PMTs signals at a sampling
1284 rate of 1 GHz. The 12 bit samples are stored in a circular memory buffer. At trigger

1285 time, data from the TOF PMTs are recorded to output in a 28.7 μ s windows starting
1286 approximately 8.4 μ s before the trigger time.

1287 **TOF functionality**

1288 The TOF signals rise time (10-90%) is 4 ns and a full width, half-maximum of 9 ns
1289 consistent in time. The signal amplitudes from the upstream TOF and downstream
1290 TOF are slightly different: 200 mV for the upstream PMTs but only 50 mV for
1291 downstream PMTs. The time of the pulses was calculated utilizing an oversampled
1292 template derived from the data itself. We take the pulse pedestal from samples
1293 far from the pulse and subtract it from the pulse amplitude. We then vertically
1294 stretch a template to match the pedestal-subtracted pulse amplitude and we move
1295 it horizontally to find the time. With this technique, we find a pulse time-pickoff
1296 resolution better than 100 ps. The pulse pile up is not a significant problem given
1297 the TOF timing resolution and the rate of the particle beam. Leveraging on the
1298 pulses width uniformity of any given PMT, we flag events where two pulses overlap
1299 as closely in time as 4 ns with a 90% efficiency according to simulation.

1300 We combine the pulses from the two PMTs on each paddle to determine the
1301 particles' arrival time by averaging the time measured from the single PMT, so to
1302 minimize errors due to optical path differences in the scintillator. However, a time
1303 spread of approximately 300 ps is present in both the upstream and downstream
1304 detectors, likely due to transit time jitter in the PMTs themselves.

1305 **3.2.4 Punch-Through and Muon Range Stack Instruments**

1306 The punch-through and the muon range stack (MuRS) detectors are located down-
1307 stream of the TPC. These detectors provide a sample of TPC crossing tracks without
1308 relying on TPC information and can be used to improve particle ID for muons and
1309 pions with momentum higher than 450 MeV/c.



Figure 3.5: Image of the down stream time of flight paddle, PMTs and relative support structure before mounting.

1310 The punch-through is simple sheet of scintillator material, read out by two PMTs.

1311 The MuRS is a segmented block of steel with four slots instrumented with scintillation
1312 bars. The four steel layers in front of each instrumented slot are 2 cm, 2 cm, 14 cm
1313 and 16 cm deep in the beam direction. Each instrumented slot is equipped with
1314 four scintillation bars each, positioned horizontally in the direction orthogonal to the
1315 beam. Each scintillator bar measures ? x ? x 2 cm and it is read out by one PMT.

1316 The signals from both the punch-thorough and the MuRS PMTs are sent to a
1317 NIM discriminator. If the signal crosses the discriminator threshold, it is digitized in
1318 the CAEN V1740, same as the TPC. The sampling time of the CAEN V1740 is slow
1319 (of the order of 128 ns) and that the pulse shape information from the PMT is lost.
1320 A Punch-thorough and MuRS signal will then be simply a “hit” at a given time in
1321 the beamline event.

1322 It is worth mentioning here the presence of an additional scintillation paddle
1323 between WC4 and the downstream paddle of the TOF system, called halo. The
1324 halo is a 39x38x1 cm³ paddle with a 6.5 cm radius hole in the center, whose original

1325 function was to reject beam particles slightly offset from the beamline center. Data
1326 from this paddle turned out to be unusable, so our data events include both particle
1327 going through the halo scintillation material or through the halo hole.

1328 **3.2.5 LArIAT Cosmic Ray Paddle Detectors**

1329 LArIAT triggers both on beam events and on cosmic rays events. We perform this
1330 latter trigger by using two sets of cosmic ray paddle detectors (a.k.a. “cosmic towers”).
1331 The cosmic towers frame the LArIAT cryostat, as one sits in the downstream left
1332 corner and the other sits in the upstream right corner of the cryostat. Two paddle
1333 sets of four scintillators pieces each make up each cosmic tower, an upper set and a
1334 lower set per tower. Of the four paddles, a couple of two matched paddles stands
1335 upright while the a second matched pair lies across the top of the assembly in the top
1336 sets (or across the bottom of the assembly in the bottom sets). The horizontal couple
1337 is used as a veto for particles traveling from inside the TPC out. The four signals
1338 from the vertical paddles along one of the body diagonals of the TPC are combined
1339 in a logical “AND”. This allows to select track due to cosmic muons at the ground
1340 level crossing the TPC along one of its diagonals. Cosmic ray muons whose average
1341 energy is in the few GeV range crossing both anode and cathode populate the events
1342 triggered this way. This particularly useful sample of tracks is associated can be used
1343 for many tasks; for example, we use anode-cathode piercing tracks to cross check
1344 the TPC electric field on data (see Appendix A), to calibrate the charge response of
1345 the TPC wires for the full TPC volume and to measure the electron lifetime in the
1346 chamber [103].

1347 We retrieved the scintillation paddles from the decommissioning of the CDF de-
1348 tector at Fermilab and we used only the paddles with a counting efficiency greater
1349 than 95% and low noise at working voltage. The measured trigger rate of the whole
1350 system is 0.032 Hz, corresponding to ~ 2 muons per minute.



Figure 3.6: Photograph of one of the scintillation counters used in the cosmic towers.

1351 3.3 In the Cryostat

1352 3.3.1 Cryogenics and Argon Purity

1353 LArIAT repurposed the ArgoNeuT cryostat [17] in order to use it in a beam of charged
1354 particles, and added a new process piping and a new liquid argon filtration system in
1355 FTBF. Inside the LArIAT experimental hall, the cryostat sits in the beam of charged
1356 particles with its horizontal main axis oriented parallel to the secondary beam, 3°
1357 off axis from the tertiary beam

1358 Two volumes make up LArIAT cryostat, shown in Figure 3.7: the inner vessel and
1359 the outer vessel. Purified liquid argon fills the inner vessel, while the outer volume
1360 provides insulation through a vacuum jacket equipped with layers of aluminized mylar
1361 superinsulation. The inner vessel is a cylinder of 130 cm length and 76.2 cm diameter,
1362 containing about 550 L of LAr, corresponding to a mass of 0.77 ton. We run the signal
1363 cables for the LArTPC and the high voltage feedthrough through a “chimney” at the
1364 top and mid-length of the cryostat.

1365 Given the different scopes of the ArgoNeuT and LArIAT detectors, we made
1366 several modifications to the ArgoNeuT cryostat in order to use it in LArIAT. In
1367 particular, the modifications shown in Figure 3.8 were necessary to account for the
1368 beam of charged particles entering the TPC and to employ the new FTBF liquid

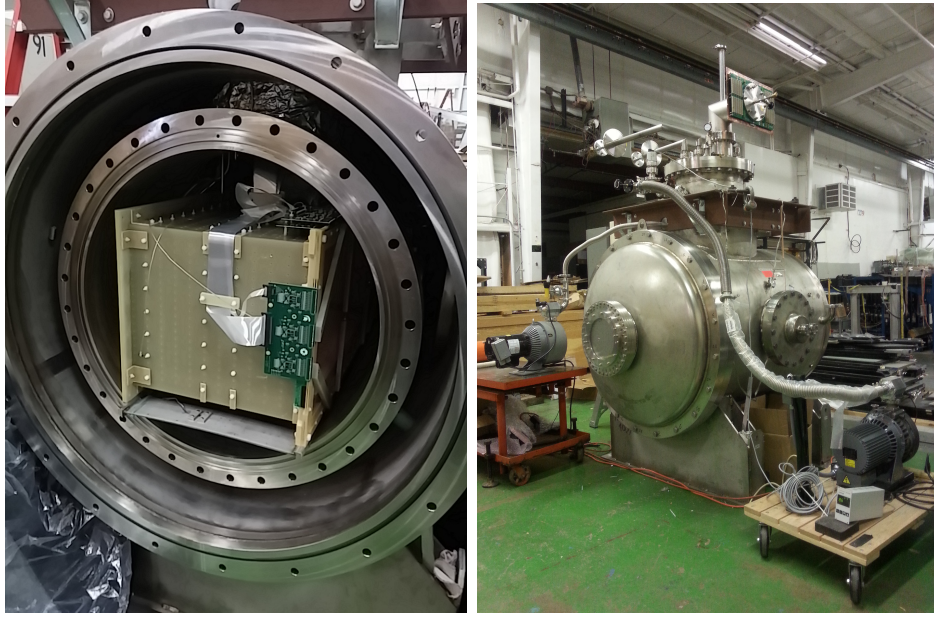


Figure 3.7: Left: the LArIAT TPC in the inner volume of the open cryostat. Right: cryostat fully sealed ready to be transported to FTBF.

1369 argon purification system. We added a “beam window” on the front outer end cap
 1370 and an “excluder” on the inner endcap, with the purpose of minimizing the amount of
 1371 non-instrumented material upstream of the TPC’s active volume. The amount of non-
 1372 instrumented material in front of the TPC for LArIAT corresponds to ~ 0.3 electron
 1373 radiation lengths (X_0), to compare against the $\sim 1.6X_0$ of ArgoNeuT. To allow studies
 1374 of the scintillation light, we added a side port feedthrough which enables the mounting
 1375 of the light collection system, as well as the connections for the corresponding signal
 1376 and high-voltage cables (see Section 3.3.3). We modified the bottom of the cryostat
 1377 adding Conflat and ISO flange sealing to connect the liquid argon transfer line to the
 1378 new argon cooling and purification system.

1379 As in any other LArTPC, argon purity is a crucial parameter for LArIAT. Indeed,
 1380 the presence of contaminants affects both the basic working principles of a LArTPC,
 1381 as shown in section 2.1.2: electronegative contaminants such as oxygen and water de-
 1382 crease the number of ionization electrons collected on the wires after drifting through
 1383 the volume. In addition, contaminants such as Nitrogen decrease the light yield



Figure 3.8: Main modifications to the ArgoNeuT cryostat: 1) outlet for connection to the purification system at the bottom of the cryostat; 2) the “beam-window” on the outer endcap and “excluder” which reduces the amount of non-instrumented material before the TPC; 3) the side port to host the light collection system.

from scintillation light, especially in its slow component. In LArIAT, contaminations should not exceed the level of 0.2 parts per billion (ppb). We achieve this level of purity in several stages. The specifics required for the commercial argon bought for LArIAT are 2 parts per million (ppm) oxygen, 3.5 ppm water, and 10 ppm nitrogen. This argon is monitored with the use of commercial gas analyzer. Argon is stored in a dewar external to LArIAT hall and filtered before filling the TPC. LArIAT uses a filtration system designed for the Liquid Argon Purity Demonstrator (LAPD) [56]: half of a 77 liter filter contains a 4A molecular sieve (Sigma-Aldrich [109]) able to remove mainly water, while the other half contains BASF CU-0226 S, a highly dispersed copper oxide impregnated on a high surface area alumina, apt to remove mainly oxygen [27]. A single pass of argon in the filter is sufficient to achieve the necessary purity, unless the filter is saturated. In case the filter saturates, the media needs to be regenerated by using heated gas; this happened twice during the Run II period¹.

¹. We deemed the filter regeneration necessary every time the electron lifetime dropped under 100 μ s.

1397 The electron lifetime during the full LArIAT data taking are shown in Figure 2.4.
1398 The filtered argon reaches the inner vessel via a liquid feedthrough which is routed to
1399 the bottom of the cryostat. Argon is not recirculated in the system; rather, it boils
1400 off and vents to the atmosphere. During data taking, we replenish the argon in the
1401 cryostat every 6 hours to keep the TPC high voltage feedthrough and cold electronics
1402 always submerged. In fact, we constantly monitor the level, temperature, and pres-
1403 sure of the argon both in the commercial dewar and inside the cryostat during data
1404 taking.

1405 **3.3.2 LArTPC: Charge Collection**

1406 The LArIAT Liquid Argon Time Projection Chamber is a rectangular box of dimen-
1407 sions 47 cm (drift) x 40 cm (height) x 90 cm (length), containing 170 liters of Liquid
1408 Argon. The LArTPC three major subcomponents are

- 1409 1) the cathode and field cage,
1410 2) the wire planes,
1411 3) the read-out electronics.

1412 **Cathode and field cage**

1413 A G10 plain sheet with copper metallization on one of the 40 x 90 cm inner surfaces
1414 forms the cathode. A high-voltage feedthrough on the top of the LArIAT cryostat
1415 delivers the high voltage to the cathode; the purpose of the high voltage system
1416 (Figure 3.9) is to drift ionization electrons from the interaction of charged particles
1417 in the liquid argon to the wire planes. The power supply used in this system is a
1418 Glassman LX125N16 [69] capable of generating up to -125 kV and 16 mA of current,
1419 but operated at -23.5kV during LArIAT Run-II. The power supply is connected via
1420 high voltage cables to a series of filter pots before finally reaching the cathode.

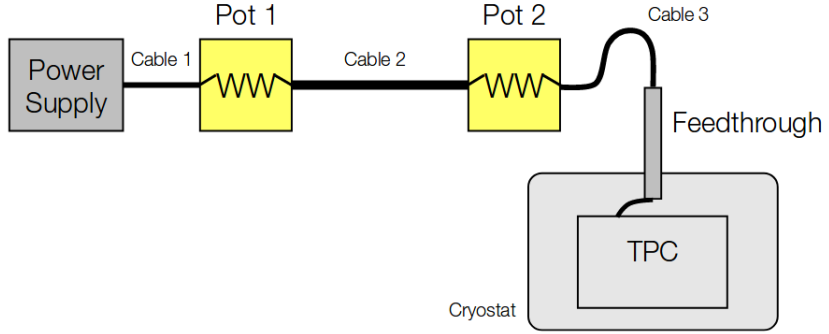


Figure 3.9: Schematic of the LArIAT high voltage system.

1421 The field cage is made of twenty-three parallel copper rings framing the inner walls
 1422 of the G10 TPC structure. A network of voltage-dividing resistors connected to the
 1423 field cage rings steps down the high voltage from the cathode to form a uniform electric
 1424 field. The electric field over the entire TPC drift volume is 486 V/cm, as measured
 1425 in appendix A. The maximum drift length, i.e. the distance between cathode and
 1426 anode planes, is 47 cm.

1427 Wire planes

1428 LArIAT Run-II has three wire planes separated by 4 mm spaces: in order of increasing
 1429 distance from the cathode, they are the shield, the induction and the collection plane.
 1430 The “wire pitch”, i.e., the distance between two adjacent wires in a given plane, is
 1431 4 mm. The shield plane counts 225 parallel wires of equal length oriented vertically.
 1432 This plane is not connected with the read-out electronics; rather it shields the outer
 1433 planes from extremely long induction signals due to the ionization in the whole drift
 1434 volume. As the shield plane acts almost like a Faraday cage, the resulting shape of
 1435 signals in the first instrumented plane (induction) is easier to reconstruct. Both the
 1436 induction and collection planes count 240 parallel wires of different length oriented at
 1437 60° from the vertical with opposite signs. Electrons moving past the induction plane
 1438 will induce a bipolar pulse on its wires; the drifting electrons will be then collected

¹⁴³⁹ on the collection plane's wires, forming a unipolar pulse.

¹⁴⁴⁰ The three wire planes and the cathode form three drift volumes, as shown in Figure
¹⁴⁴¹ 3.10. The main drift volume is defined as the region between the cathode plane and the
¹⁴⁴² shield plane (C-S). The other two drift regions are those between the shield plane and
¹⁴⁴³ the induction plane (S-I), and between the induction plane and the collection plane
¹⁴⁴⁴ (I-C). The electric field in these regions is chosen to satisfy the charge transparency
¹⁴⁴⁵ condition and allow for 100% transmission of the drifting electrons through the shield
¹⁴⁴⁶ and the induction planes.

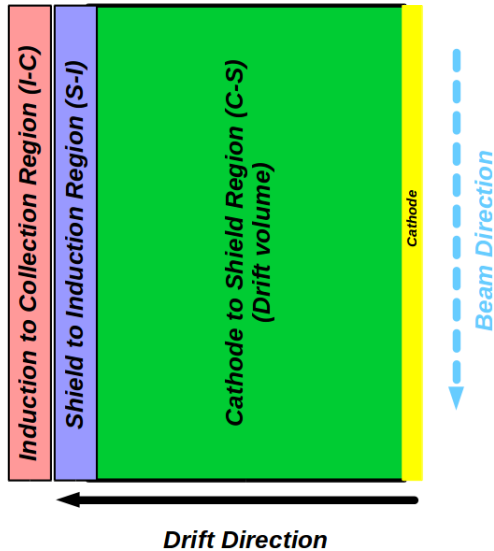


Figure 3.10: Schematic of the three drift regions inside the LArIAT TPC: the main drift volume between the cathode and the shield plane (C-S) in green, the region between the shield plane and the induction plane (S-I) in purple, and the region between the induction plane and the collection plane (I-C) in pink.

¹⁴⁴⁷ Table 3.1 provides the default voltages applied to the cathode and the shield,
¹⁴⁴⁸ induction, and collection plane.

Table 3.1: Cathode and anode planes default voltages

Cathode	Shield	Induction	Collection
-23.17 kV	-298.8 V	-18.5 V	338.5 V

1449 **Electronics**

1450 Dedicated electronics read the induction and collection plane wires, for a total of
1451 480-channel analog signal path from the TPC wires to the signal digitizers. A digital
1452 control system for the TPC-mounted electronics, a power supply, and a distribution
1453 system complete the front-end system. Figure 3.11 shows a block diagram of the
1454 overall system. The direct readout of the ionization electrons in liquid argon forms
1455 typically small signals on the wires, which need amplification in oder to be processed.
1456 LArIAT performs the amplification stage directly in cold with amplifiers mounted
1457 on the TPC frame inside the liquid argon. The BNL ASICs adopted in LArIAT are
1458 designated as LArASIC, version 4-star and are the same used by the MicroBooNE
1459 experiment [59]. The signal from the ASICs are driven to the other end of the readout
1460 chain, to the CAEN V1740 digitizers [35]. The CAEN V1740 has a 12 bit resolution
1461 and a maximum input range of 2 VDC, resulting in about 180 ADC count for a
1462 crossing MIP.

1463 **3.3.3 LArTPC: Light Collection System**

1464 The collection of scintillation photons is the second mechanism of particle detection
1465 in argon other than the ionization electrons. Over the course of LArIAT's three years
1466 of data taking, the light collection system changed several times. We describe here
1467 the light collection system for Run II. Two PMTs, a 3-inch diameter Hamamatsu
1468 R-11065 and 2-inch diameter ETL D757KFL [7], as well as three SiPMs arrays (two
1469 Hamamatsu S11828-3344M 4x4 arrays and one single-channel SensL MicroFB-60035)
1470 are mounted on the PEEK support structure. PEEK screws into an access flange
1471 as shown in Figure 3.12, on the anode side, leaving approximately 5 cm of clearance
1472 from the collection plane.

1473 Liquid argon scintillates in vacuum-ultraviolet (VUV) range at 128 nm; since
1474 cryogenic PMTs are not sensitive to VUV wavelengths, we need to shift the light to a

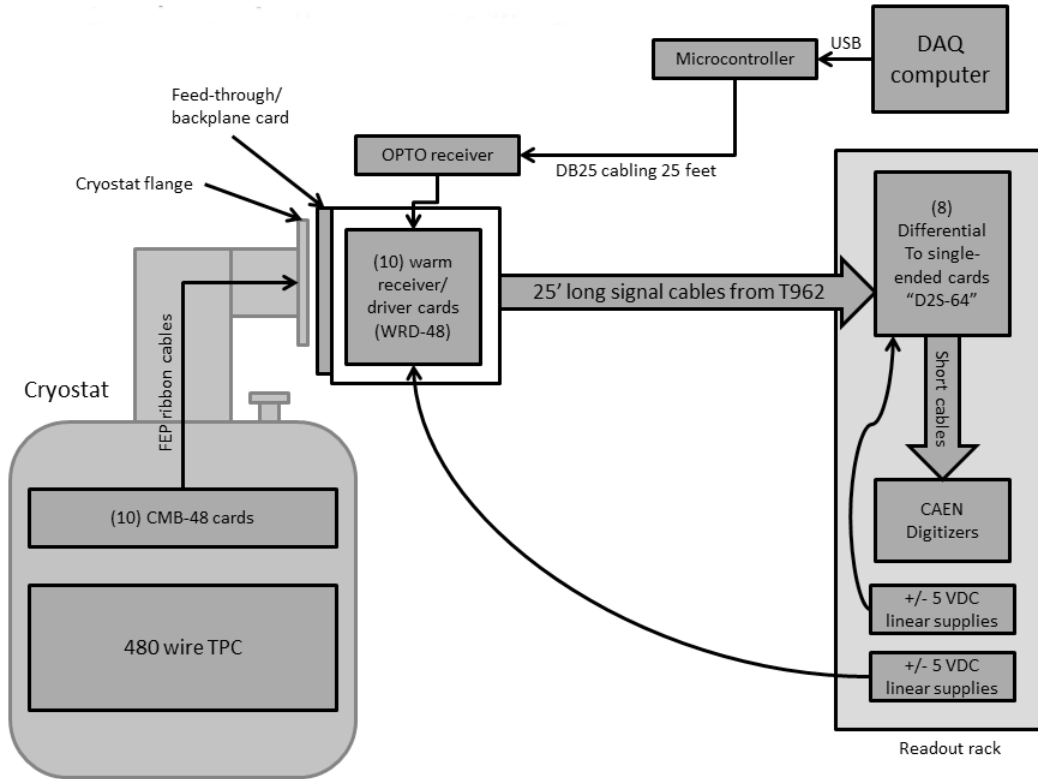


Figure 3.11: Overview of LArIAT Front End electronics.

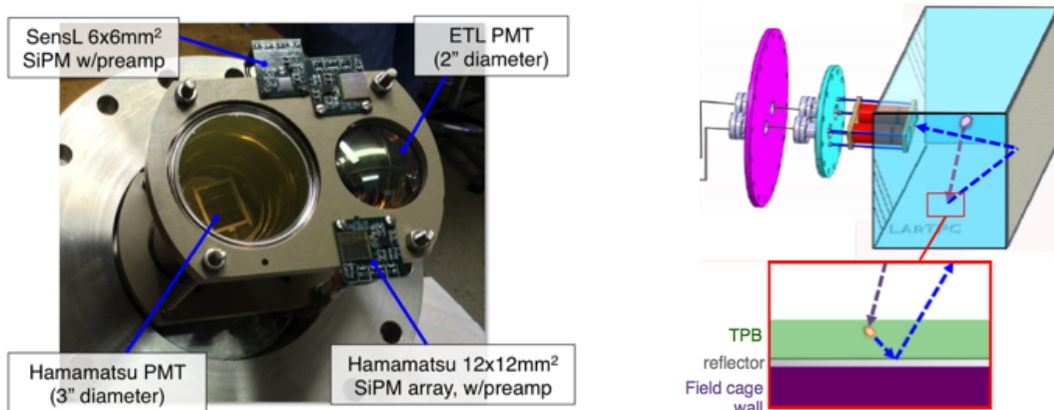


Figure 3.12: LArIAT's photodetector system for observing LAr scintillation light inside the TPC (left), and a simplified schematic of VUV light being wavelength-shifting along the TPB-coated reflecting foils (right).

range that is visible to the PMTs. In LArIAT, the wavelength shifting is achieved by installing highly-reflective 3M VIKUITI dielectric substrate foils coated with a thin layer of tetraphenyl-butadiene (TPB) on the four unbiased walls of the TPC. The scintillation light interaction with the TPB emits one or more visible photons, which are then reflected into the chamber. Thus, the light yield increases and results in higher uniformity of light across the TPC active volume, allowing the possibility of light-based calorimetry, currently under study.

For Run II, we coated the windows of the ETL PMT and the SensL SiPM with a thin layer of TPB. In doing so, some of the VUV scintillation light converts into visible right at the sensor faces, keeping information on the direction of the light source. Information about the light directionality is hindered for the light reflected on foils, as the reflection is uniform in angle.

3.4 Trigger and DAQ

The LArIAT DAQ and trigger system governs the read out of all the many subsystems forming LArIAT. The CAEN V1495 module [34] and its user-programmable FPGA are the core of this system. Every 10 ns, this module checks for matches between sixteen logical inputs and user-defined patterns in the trigger menu; if it finds a match for two consecutive clock ticks, that trigger fires.

LArIAT receives three logic signals from the Fermilab accelerator complex related to the beam timing which we use as input triggers: a pulse just before the beam, a pulse indicating beam-on, and a beam-off pulse.

The beam instruments, the cosmic ray taggers, and the light collection system provide the other NIM-standard logic pulse inputs to the trigger decision. We automatically log the trigger inputs configuration with the rest of the DAQ configuration at the beginning of each run.

1500 Fundamental inputs to the trigger card come from the TOF (see section 3.2.3)
1501 and the wire chambers (see section 3.2.2), as activity in these systems points to the
1502 presence of a charged particle in tertiary beam line. In particular, the discriminated
1503 pulses from the TOF PMTs form a NIM logic pulse for the trigger logic. We ask
1504 for a coincidence within a 20 ns window for all the pulses from the PMTs looking at
1505 the same scintillator block and use a delayed coincidence between the upstream and
1506 downstream paddle to inform the trigger decision. In order to form a coincidence
1507 between the upstream and downstream paddles, we delay the upstream paddle coin-
1508 cidence by 20 ns and widen it by 100 ns. The delay and widening are necessary to
1509 account for both lightspeed particles and slower particles (high-mass) to travel the
1510 6.5 m between the upstream and the downstream paddles. For the read out of the
1511 wire chambers, we use a total of sixteen multi-hit TDCs [72], four per chamber: two
1512 TDC per plane (horizontal and vertical), sixty-four wires per TDC. In each TDC, we
1513 keep the logical “OR” for any signal over threshold from the sixty-four wires. We
1514 then require a coincidence between the “OR” for the horizontal TDCs and the “OR”
1515 for the vertical TDCs: with this logic we make sure that at least one horizontal wire
1516 and one vertical wire saw significant signal in one wire chamber. The single logical
1517 pulse from each of the four wire chambers feeds into the first four inputs to the V1495
1518 trigger card. We require a coincidence within 20 ns of at least three logical inputs to
1519 form a trigger.

1520 The cosmic towers (see Section 3.2.5) provide another primary input to the trigger,
1521 in order to capture long tracks from cosmic muons crossing the TPC. We use NIM
1522 modules to require coincidences between one upper and one lower paddle set of any
1523 opposite cosmic towers. The OR all the opposite towers’ coincidences is fed as an
1524 input to the trigger card.

1525 We use the signal from the cryogenic PMTs (see Section 3.3.3) to form several
1526 interesting triggers. The coincidence of signals from all the PMT pulses within \sim 20 ns

1527 is an indication of ionizing radiation in the TPC and forms a trigger input. The
1528 coincidence of two subsequent scintillation logic pulses delayed by a maximum of $7 \mu\text{s}$
1529 forms the Michel electron trigger.

1530 3.5 Control Systems

1531 LArIAT is a complex ensemble of systems which needed to be monitored simultane-
1532 ously during data taking. We performed the monitoring of the systems operations
1533 with a slow control system, a DAQ monitoring system and a low level data quality
1534 monitoring described in the following sections.

1535 Slow Control

1536 We used the Synoptic Java Web Start framework [19] as a real-time display of subsys-
1537 tem conditions. Synoptic provides a Graphical User Interface that talks to the Fer-
1538 milab Accelerator Control System via the ACNET protocol. Its simple GUI allowed
1539 us to change the operating parameters and to graph the trends of several variables of
1540 interest for all of the tertiary beam detectors. Among the most important quantities
1541 monitored by Synoptic there are the level of argon in both the inner vessel and the
1542 external dewar, the operating voltages of cathode and wire planes, of the PMTs and
1543 SiPMs, and of the four wire chambers, as well as the magnet temperatures. Fig-
1544 ure 3.13 shows an example of the monitoring system. LArIAT uses the Accelerator
1545 Control NETwork system (ACNET) to monitor the beam conditions of the MCenter
1546 beamline. For example, the horizontal and vertical position of the beam at the first
1547 two wire chambers (WC1 and WC2) are shown in 3.14 as seen by the shifter during
1548 data taking.

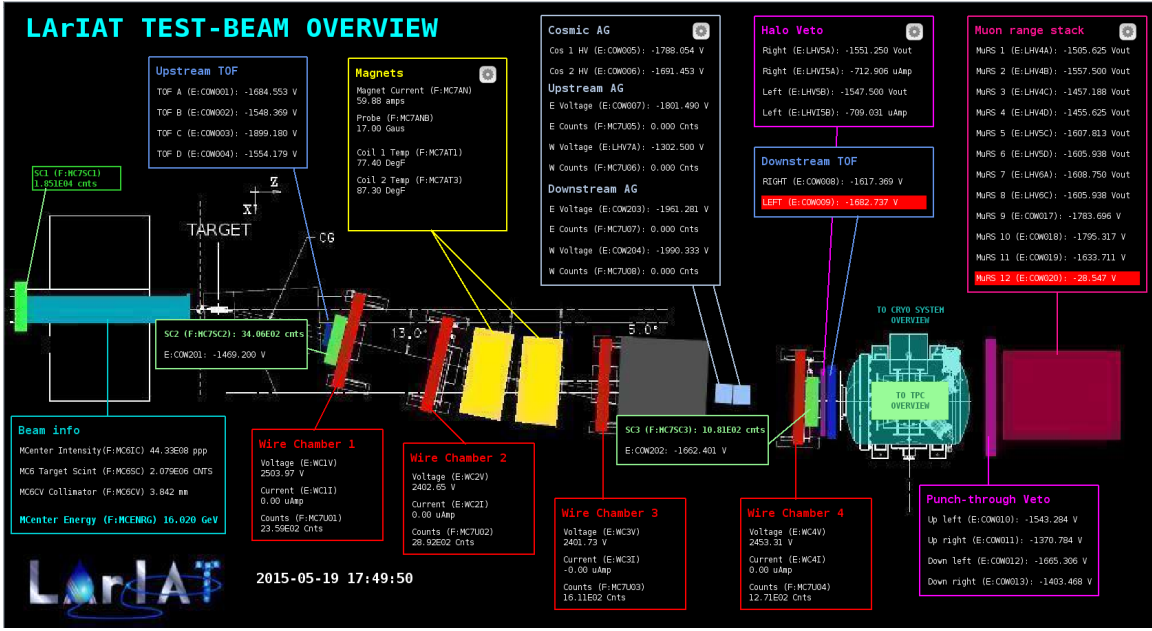


Figure 3.13: Interface of the Synoptic slow control system

1549 DAQ Monitoring

1550 We monitor the data taking and the run time evolution with the Run Status Webpage
 1551 (<http://lariat-wbm.fnal.gov/lariat/run.html>), a webpage updated in real-time. The
 1552 page displays, among other information, the total number of triggers in the event,
 1553 the total number of detectors triggered during a beam spill, the trigger patterns, the
 1554 number of times a particular trigger pattern was satisfied during a beam spill, and
 1555 the current time relative to the Fermilab accelerator complex supercycle. A screen
 1556 shot of the page is show in figure 3.15.

1557 Data Quality Monitoring

1558 We employ two systems to ensure the quality of our data during data taking: the
 1559 Near-Real-Time Data Quality Monitoring and the Event Viewer.

1560 The Near-Real-Time Data Quality Monitoring (DQM) is a webpage which receives
 1561 updates from all the VME boards in the trigger system and displays the results of
 1562 a quick analysis of the DAQ stream of raw data on a spill-by-spill basis. The DQM

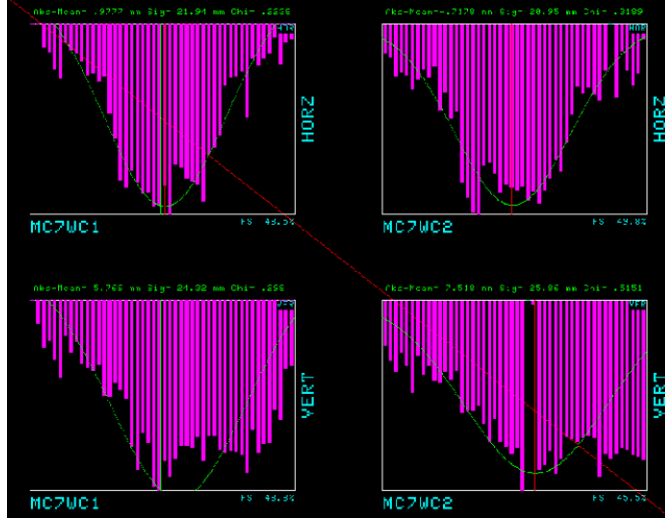


Figure 3.14: Beam position at the upstream wire chambers monitored with ACNET.

1563 allows the shifter to monitor almost in real time (typically with a 2-minute delay)
 1564 a series of low level-quantities and compare them to past collections of beam spills.
 1565 Some of the variables monitored in the DQM are the pedestal mean and RMS on
 1566 CAEN digitizer boards of the TPC wires and PMTs of the beamline detectors, the
 1567 hit occupancy and timing plots on the wire chambers, and number of data fragments
 1568 recorded that are used to build a TPC event. Abnormal values for low-level quantity
 1569 in the data activates a series of alarms in the DQM; this quick feedback on the DAQ
 1570 and beam conditions is fundamental to assure a fast debugging of the detector and a
 1571 very efficient data taking during beam uptime.

1572 The online Event Viewer displays a two dimensional representation (Wire vs Time)
 1573 of LArIAT TPC events on both the Induction and the Collection planes in near real
 1574 time. The raw pulses collected by the DAQ on each wire are plotted as a function
 1575 of drift time, resulting in an image of the TPC event easily readable by the shifter.
 1576 This tool guarantees a particularly good check of the TPC operation which activate
 1577 an immediate feedback for troubleshooting a number of issues. For example, it is
 1578 easy for the shifter to spot high occupancy events and request a reduction of the
 1579 primary beam intensity, or to spot a decrease of the argon purity which requires the

1580 regeneration of filters, or to catch the presence of electronic noise and reboot the
1581 ASICs. An example of high occupancy event is shown in 3.16.

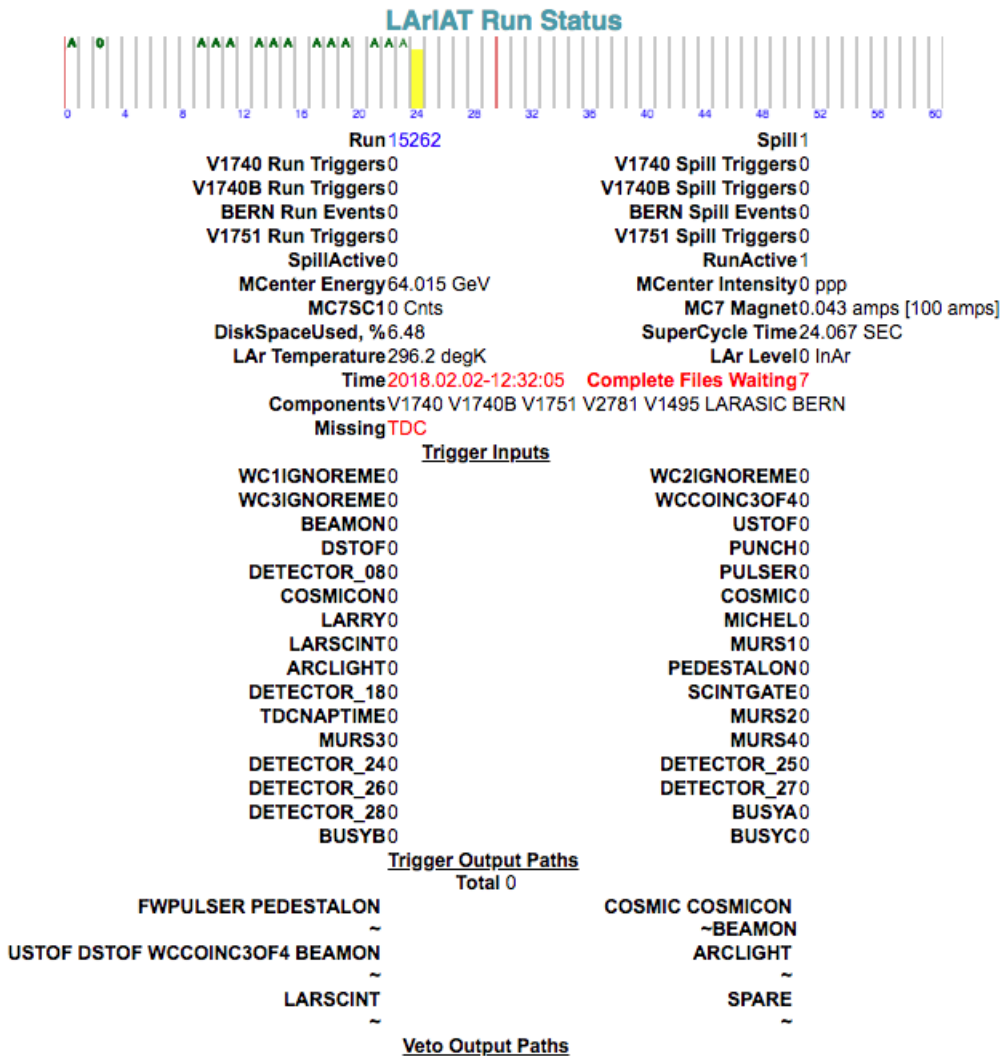


Figure 3.15: Run Status page at LArIAT downtime. At the top the yellow bar displays the current position in the Fermilab supercycle. Interesting information to be monitored by the shifter were the run number and number of spills, time elapsed from data taking (here in red), the energy of the secondary beam and the trigger paths.

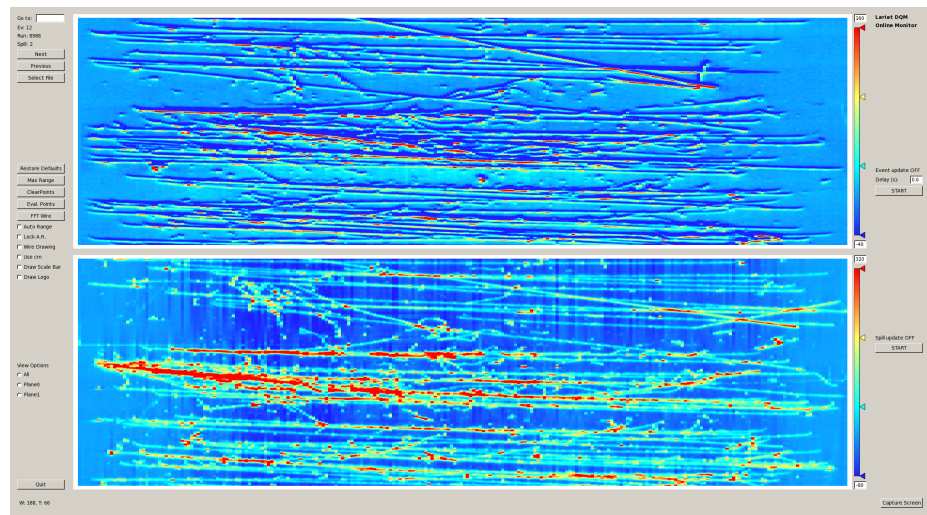


Figure 3.16: High occupancy event display: induction plane (top) and collection plane (bottom).

1582 **Chapter 4**

1583 **Total Hadronic Cross Section**

1584 **Measurement Methodology**

1585 “Like a lemon to the lime and the bubble to the bee”

1586 – Eazy-E, Gimmie that Nutt, 1993 –

1587 This chapter describes the general procedure employed to measure a total hadronic
1588 differential cross section in LArIAT. Albeit with small differences, both the
1589 (π^- ,Ar) and (K^+ ,Ar) total hadronic cross section measurements rely on the same
1590 procedure described in details in the following sections. We start by selecting the
1591 particle of interest using a combination of beamline detectors and TPC information
1592 (Section 4.1). We then perform a handshake between the beamline information and
1593 the TPC tracking to assure the selection of the right TPC track (Section 4.2). Finally,
1594 we apply the “thin slice” method and measure the “raw” hadronic cross section
1595 (Section 4.3). A series of corrections are then evaluated to obtain the “true” cross
1596 section (Section 4.3.3).

1597 At the end of this chapter, we show a sanity check of the methodology by applying
1598 the thin slice method employing only MC truth information and retrieving the Geant4
1599 tabulated cross section for pions and kaons (Section 4.4).

1600 4.1 Event Selection

1601 The measurement of the (π^- ,Ar) and (K^+ ,Ar) total hadronic cross section in LArIAT
1602 starts by selecting the pool of pion or kaon candidates and measuring their momen-
1603 tum. This is done through the series of selections on beamline and TPC information
1604 described in the next sections. The summary of the event selection in data is reported
1605 in Table 4.1.

1606 4.1.1 Selection of Beamline Events

1607 As shown in equation 4.5, we leverage the beamline particle identification and mo-
1608 mentum measurement before entering the TPC as input to evaluate the kinetic
1609 energy for the hadrons used in the cross sections measurements. Thus, we select the
1610 LArIAT data to keep only events whose wire chamber and time of flight information
1611 is registered (line 1 in Table 4.1). Additionally, we perform a check of the plausi-
1612 bility of the trajectory inside the beamline detectors: given the position of the hits
1613 in the four wire chambers, we make sure the particle's trajectory does not cross any
1614 impenetrable material such as the collimator and the magnets steel (line 2 in Table
1615 4.1).

	Run-II Neg Pol	Run-II Pos Pol
1. Events Reconstructed in Beamline	158396	260810
2. Events with Plausible Trajectory	147468	240954
3. Beamline $\pi^-/\mu^-/e^-$ Candidate	138481	N.A.
4. Beamline K^+ Candidate	N.A	2837
5. Events Surviving Pile Up Filter	108929	2389
6. Events with WC2TPC Match	41757	1081
7. Events Surviving Shower Filter	40841	N.A.
8. Available Events For Cross Section	40841	1081

Table 4.1: Number of data events for Run-II Negative and Positive polarity

1616 **4.1.2 Particle Identification in the Beamline**

1617 In data, the main tool to establish the identity of the hadron of interest is the LArIAT
1618 tertiary beamline, in its function of mass spectrometer. We combine the measurement
1619 of the time of flight, TOF , and the beamline momentum, p_{Beam} , to reconstruct the
1620 invariant mass of the particles in the beamline, m_{Beam} , as follows

$$m_{Beam} = \frac{p_{Beam}}{c} \sqrt{\left(\frac{TOF * c}{l}\right)^2 - 1}, \quad (4.1)$$

1621 where c is the speed of light and l is the length of the particle's trajectory between
1622 the time of flight paddles.

1623 Figure 4.1 shows the mass distribution for the Run II negative polarity runs on
1624 the left and positive polarity runs on the right. We perform the classification of events
1625 into the different samples as follows:

- 1626 • $\pi/\mu/e$: mass < 350 MeV
- 1627 • kaon: 350 MeV < mass < 650 MeV
- 1628 • proton: 650 MeV < mass < 3000 MeV.

1629 Lines 3 and 4 in Table 4.1 show the number of negative $\pi/\mu/e$ and positive K
1630 candidates which pass the mass selection for LArIAT Run-II data.

1631 **4.1.3 TPC Selection: Halo Mitigation**

1632 The secondary beam impinging on LArIAT secondary target produces a plethora of
1633 particles which propagates downstream. The presence of upstream and downstream
1634 collimators greatly abates the number of particles tracing down the LArIAT tertiary
1635 beamline. However, it is possible that more than one particle sneaks into the LArTPC
1636 during its readout time: the TPC readout is triggered by the particle firing the

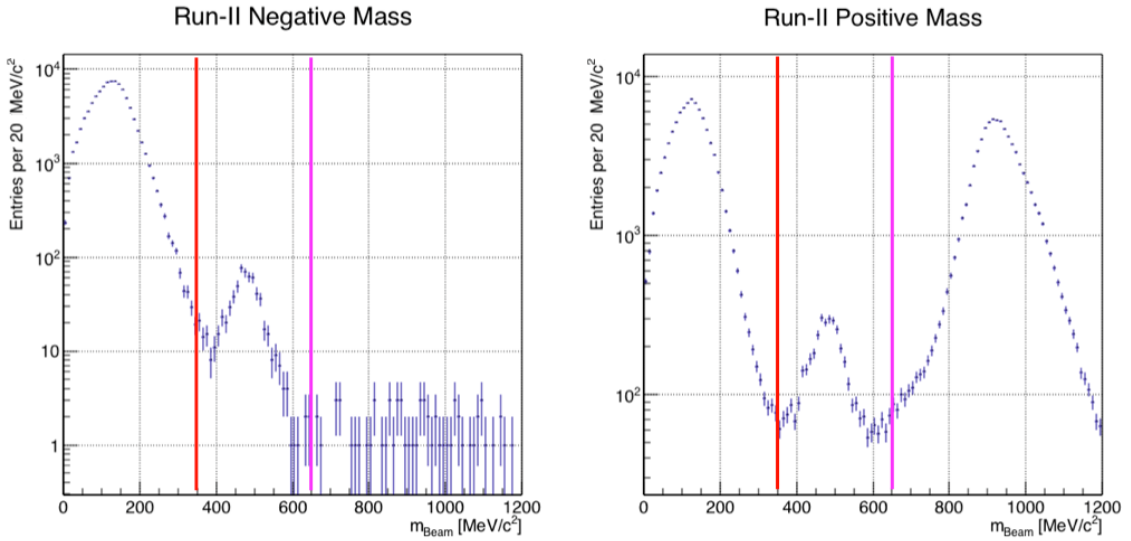


Figure 4.1: Distribution of the beamline mass as calculated according to equation 4.1 for the Run-II events reconstructed in the beamline, negative polarity runs on the left and positive polarity runs on the right. The classification of the events into $\pi^\pm/\mu^\pm/e^\pm$, K^\pm , or (anti)proton is based on these distributions, whose selection cut are represented by the vertical colored lines.

₁₆₃₇ beamline detectors, but particles from the beam halo might be present in the TPC at
₁₆₃₈ the same time. We call “pile up” the additional traces in the TPC. We adjusted the
₁₆₃₉ primary beam intensity between LArIAT Run I and Run II to reduce the presence of
₁₆₄₀ events with high pile up particles in the data sample. For the cross section analyses,
₁₆₄₁ we remove events with more than 4 tracks in the first 14 cm upstream portion of the
₁₆₄₂ TPC from the sample (line 5 in in Table 4.1).

₁₆₄₃ 4.1.4 TPC Selection: Shower Removal

₁₆₄₄ In the case of the (π^-, Ar) cross section, the resolution of beamline mass spectrometer
₁₆₄₅ is not sufficient to select a beam of pure pions. In fact, muons and electrons survive
₁₆₄₆ the selection on the beamline mass. It is important to notice that the composition of
₁₆₄₇ the negative polarity beam is mostly pions, as will be discussed in section 5.2.1. Still,
₁₆₄₈ we devise a selection on the TPC information to mitigate the presence of electrons

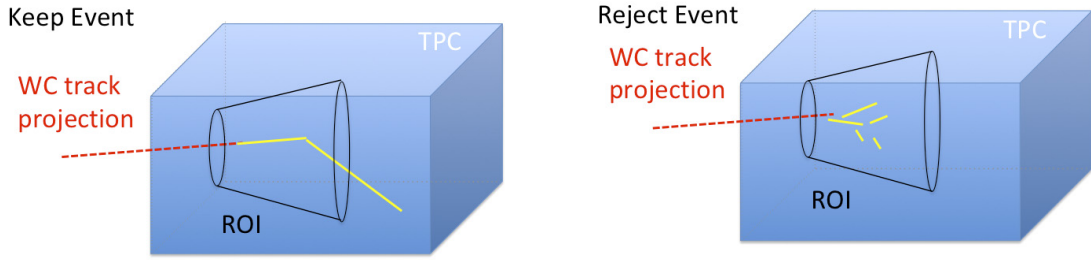


Figure 4.2: Visual rendering of the shower filter. The ROI is a cut cone, with a small radius of 4 cm, a big radius of 10 cm and an height of 42 cm (corresponding to 3 radiation lengths for electrons in Argon).

1649 in the sample used for the pion cross section. The selection relies on the different
 1650 topologies of a pion and an electron event in the argon: while the former will trace
 1651 a track inside the TPC active volume, the latter will tend to “shower”, i.e. interact
 1652 with the medium, producing bremsstrahlung photons which pair convert into several
 1653 short tracks. In order to remove the shower topology, we create a region of interest
 1654 (ROI) around the TPC track corresponding to the beamline particle. We look for
 1655 short tracks contained in the ROI, as depicted in figure 4.4: if more than 5 tracks
 1656 shorter than 10 cm are in the ROI, we reject the event. Line 7 in Table 4.1 shows
 1657 the number of events surviving this selection.

1658 **4.2 Beamline and TPC Handshake: the Wire Cham- 1659 ber to TPC Match**

1660 For each event passing the selection on its beamline information, we need to identify
 1661 the track inside the TPC corresponding to the particle which triggered the beamline
 1662 detectors, a procedure we refer to as “WC to TPC match” (WC2TPC for short).
 1663 In general, the TPC tracking algorithm will reconstruct more than one track in the
 1664 event, partially due to the fact that hadrons interact in the chamber and partially
 1665 because of pile up particles during the triggered TPC readout time, as shown in

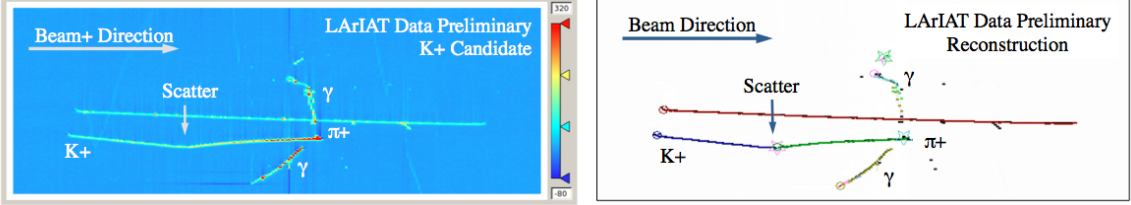


Figure 4.3: Kaon candidate event: on the right, event display showing raw quantities; on the left, event display showing reconstructed tracks. In the reconstructed event display, different colors represent different track objects. A kink is visible in the kaon ionization, signature of a hadronic interaction: the tracking correctly stops at the kink position and two tracks are formed. An additional pile-up track is so present in the event (top track in red).

1666 figure 4.3.

1667 We attempt to uniquely match one wire chamber track to one and only one recon-
 1668 structed TPC track. In order to determine if a match is present, we apply a geomet-
 1669 rical selection on the relative the position of the wire chamber and TPC tracks. We
 1670 start by considering only TPC tracks whose first point is in the first 2 cm upstream
 1671 portion of the TPC for the match. We project the wire chamber track to the TPC
 1672 front face where we define the coordinates of the projected point as x_{FF} and y_{FF} . For
 1673 each considered TPC track, we define ΔX as the difference between the x position of
 1674 the most upstream point of the TPC track and x_{FF} . ΔY is defined analogously. We
 1675 define the radius difference, ΔR , as $\Delta R = \sqrt{\Delta X^2 + \Delta Y^2}$. We define as α the angle
 1676 between the incident WC track and the TPC track in the plane that contains them.
 1677 If $\Delta R < 4$ cm, $\alpha < 8^\circ$, a match between WC-track and TPC track is found. We
 1678 describe how we determine the value for the radius and angular selection in Section
 1679 5.5.1. We discard events with multiple WC2TPC matches. We use only those TPC
 1680 tracks that are matched to WC tracks in the cross section calculation. Line 6 in Table
 1681 4.1 shows the number of events where a unique WC2TPC match was found.

1682 In MC, we mimic the matching between the WC and the TPC track by construct-
 1683 ing a fake WC track using truth information at wire chamber four. We then apply
 1684 the same WC to TPC matching algorithm as in data.

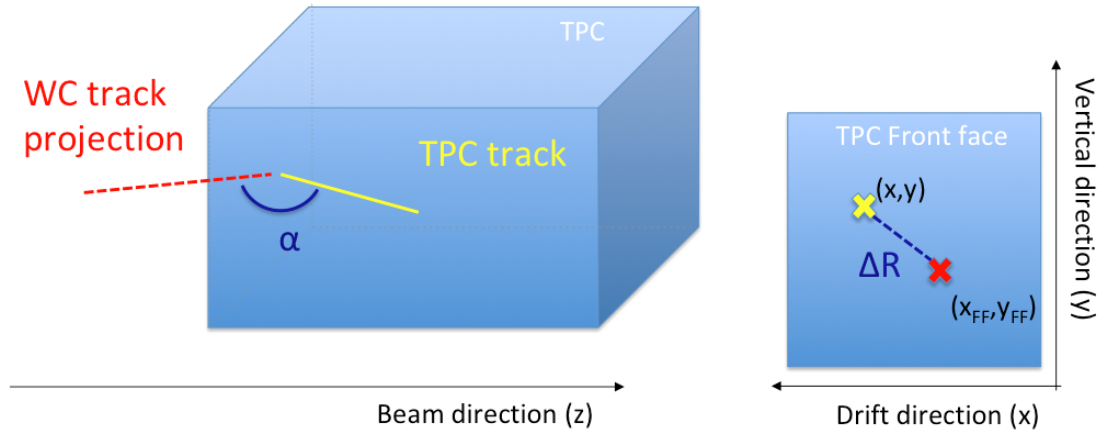


Figure 4.4: Visual rendering of the wire chamber to TPC match.

1685 4.3 The Thin Slice Method

1686 Once we have selected the pool of hadron candidates and we have identified the TPC
1687 track corresponding to the beamline event, we apply the thin slice method to measure
1688 the cross section, as the following sections describe.

1689 4.3.1 Cross Sections on Thin Target

1690 Cross section measurements on a thin target have been the bread and butter of
1691 nuclear and particle experimentalists since the Geiger-Marsden experiments [66]. At
1692 their core, this type of experiments consists in shooting a beam of particles with a
1693 known flux on a thin slab of material and recording the outgoing flux.

1694 In general, the target is not a single particle, but rather a slab of material con-
1695 taining many diffusion centers. The so-called “thin target” approximation assumes
1696 that the target centers are uniformly distributed in the material and that the target
1697 is thin compared to the projectile interaction length, so that no center of interaction
1698 sits in front of another. In this approximation, the ratio between the number of parti-
1699 cles interacting in the target N_{Int} and number of incident particles N_{Inc} on the target
1700 determines the interaction probability $P_{\text{Interacting}}$, which is the complementary to one

1701 of the survival probability $P_{Survival}$. Equation 4.2

$$P_{Survival} = 1 - P_{Interacting} = 1 - \frac{N_{Int}}{N_{Inc}} = e^{-\sigma_{TOT}n\delta X} \quad (4.2)$$

1702 describes the probability for a particle to survive the thin target. This formula relates
1703 the interaction probability to the total hadronic cross section (σ_{TOT}), the density of
1704 the target centers (n)¹ and the thickness of the target along the incident hadron
1705 direction (δX). If the target is thin compared to the interaction length of the process
1706 considered, we can Taylor expand the exponential function in equation 4.2 and find
1707 a simple proportionality relationship between the cross section and the number of
1708 incident and interacting particles, as shown in equation 4.3:

$$1 - \frac{N_{Int}}{N_{Inc}} = 1 - \sigma_{TOT}n\delta X + O(\delta X^2). \quad (4.3)$$

1709 Solving for the cross section, we find:

$$\sigma_{TOT} = \frac{1}{n\delta X} \frac{N_{Int}}{N_{Inc}}. \quad (4.4)$$

1710 4.3.2 Not-so-Thin Target: Slicing the Argon

1711 The interaction length of pions and kaons in argon is expected to be of the order
1712 of 50 cm for pions and 100 cm for kaons. Thus, the LArIAT TPC, with its 90 cm
1713 of length, is not a thin target. However, the fine-grained tracking of the LArIAT
1714 LArTPC allows us to treat the argon volume as a sequence of many adjacent thin
1715 targets.

1716 As described in Chapter 3, LArIAT wire planes consist of 240 wires each. The
1717 wires are oriented at +/- 60° from the vertical direction at 4 mm spacing, while the

1. The scattering center density in the target, n , relates to the argon density ρ , the Avogadro number N_A and the argon molar mass m_A as $n = \frac{\rho N_A}{m_A}$.

beam direction is oriented 3 degrees off the z axis in the XZ plane. The wires collect
 signals proportional to the energy loss of the hadron along its path in a $\delta X = 4$
 $\text{mm}/(\sin(60^\circ)\cos(3^\circ)) \approx 4.7$ mm slab of liquid argon. Thus, one can think to slice
 the TPC into many thin targets of $\delta X = 4.7$ mm thickness along the direction of the
 incident particle, making a measurement at each wire along the path.

Considering each slice j a “thin target”, we can apply the cross section calculation
 from Equation 6.1 iteratively, evaluating the kinetic energy of the hadron as it enters
 each slice, E_j^{kin} . For each WC2TPC matched particle, the energy of the hadron
 entering the TPC is known thanks to the momentum and mass determination by the
 tertiary beamline,

$$E_{FrontFace}^{kin} = \sqrt{p_{Beam}^2 - m_{Beam}^2} - m_{Beam} - E_{loss}, \quad (4.5)$$

where E_{loss} is a correction for the energy loss in the uninstrumented material between
 the beamline and the TPC front face. The energy of the hadron at each slab is
 determined by subtracting the energy released by the particle in the previous slabs.
 For example, at the j^{th} point of a track, the kinetic energy will be

$$E_j^{kin} = E_{FrontFace}^{kin} - \sum_{i < j} E_{Dep,i}, \quad (4.6)$$

where $E_{Dep,i}$ is the energy deposited at each argon slice before the j^{th} point as measured
 by the calorimetry associated with the tracking.

If the particle enters a slice, it contributes to $N_{Inc}(E^{kin})$ in the energy bin corresponding
 to its kinetic energy in that slice. If it interacts in the slice, it also contributes
 to $N_{Int}(E^{kin})$ in the appropriate energy bin. The cross section as a function of kinetic
 energy, $\sigma_{TOT}(E^{kin})$ will then be proportional to the ratio $\frac{N_{Int}(E^{kin})}{N_{Inc}(E^{kin})}$.

Our goal is to measure the total interaction cross section, independently from the
 topology of the interaction. Thus, we determine that a hadron interacted simply by

	min	max
X	1 cm	46 cm
Y	-15 cm	15 cm
Z	0 cm	86 cm

Table 4.2: Fiducial volume boundaries used to determine cross section interaction point.

requiring that the last point of the WC2TPC matched track lies inside the fiducial volume, whose boundaries are defined in Table 4.2. If the TPC track stops within the fiducial volume, its last point will be the interaction point; if the track crosses the boundaries of the fiducial volume, the track will be considered “through going” and no interaction point will be found. The only slabs considered to fill the N_{Inc}) and N_{Inc} plots are the slabs included the fiducial volume.

4.3.3 Corrections to the Raw Cross Section

Equation 6.1 is a prescription for measuring the cross section in case of a pure beam of the hadron of interest and 100% efficiency in the determination of the interaction point. For example, if LArIAT had a beam of pure pions and were 100% efficient in determining the interaction point within the TPC, the pion cross section in each energy bin would be given by

$$\sigma_{TOT}^{\pi^-}(E_i) = \frac{1}{n\delta X} \frac{N_{\text{Int}}^{\pi^-}(E_i)}{N_{\text{Inc}}^{\pi^-}(E_i)}. \quad (4.7)$$

Unfortunately, this is not the case. In fact, the selection used to isolate pions in the LArIAT beam allows for the presence of some muons and electrons as background. Also, the LArIAT TPC is not 100% efficient in determining the interaction point. Therefore we need to apply two corrections evaluated on the MC in order to extract the true cross section from LArIAT data: the background subtraction and the efficiency correction. Still using the pion case as example, we estimate the pion

1758 cross section in each energy bin changing Equation 4.7 into

$$\sigma_{TOT}^{\pi^-}(E_i) = \frac{1}{n\delta X} \frac{N_{Int}^{\pi^-}(E_i)}{N_{Inc}^{\pi^-}(E_i)} = \frac{1}{n\delta X} \frac{\epsilon^{Inc}(E_i)[N_{Int}^{TOT}(E_i) - B_{Int}(E_i)]}{\epsilon^{Int}(E_i)[N_{Inc}^{TOT}(E_i) - B_{Inc}(E_i)]}, \quad (4.8)$$

1759 where $N_{Int}^{TOT}(E_i)$ and $N_{Inc}^{TOT}(E_i)$ is the measured content of the interacting and
1760 incident histograms for events that pass the event selection, $B_{Int}(E_i)$ and $B_{Inc}(E_i)$
1761 represent the contributions from beamline background to the interacting and incident
1762 histograms respectively, and $\epsilon^{Int}(E_i)$ and $\epsilon^{Inc}(E_i)$ are the efficiency corrections for said
1763 histograms.

1764 As we will show in section 5.3, the background subtraction for the interacting
1765 and incident histograms can be translated into a corresponding relative pion content
1766 $C_{Interacting}^{\pi MC}(E_i)$ and $C_{Incident}^{\pi MC}(E_i)$ and the cross section re-written as follows

$$\sigma_{TOT}^{\pi^-}(E_i) = \frac{1}{n\delta X} \frac{\epsilon^{Inc}(E_i)}{\epsilon^{Int}(E_i)} \frac{C_{Int}^{\pi MC}(E_i)}{C_{Inc}^{\pi MC}(E_i)} \frac{N_{Int}^{TOT}(E_i)}{N_{Inc}^{TOT}(E_i)}. \quad (4.9)$$

1767 4.4 Procedure testing with truth quantities

1768 The (π^-, Ar) and (K^+, Ar) total hadronic cross section implemented in Geant4 can be
1769 used as a tool to validate the measurement methodology. We describe here a closure
1770 test done on Monte Carlo to prove that the methodology of slicing the TPC retrieves
1771 the underlying cross section distribution implemented in Geant4 within the statistical
1772 uncertainty.

1773 For pions and kaons in the considered energy range, the Geant4 inelastic model
1774 adopted is “BertiniCascade”; the pion elastic cross sections are modeled on Chips,
1775 while the kaon elastic cross sections are modeled on Gheisha and Chips.

1776 For the validation test, we fire a sample of pions and a sample of kaons inside
1777 the LArIAT TPC active volume using the Data Driven Monte Carlo (see section
1778 5.2.2). We apply the thin-sliced method using only true quantities to calculate the

hadron kinetic energy at each slab in order to decouple reconstruction effects from possible issues with the methodology. For each slab of 4.7 mm length along the path of the hadron, we integrate the true energy deposition as given by the Geant4 transportation model. Then, we recursively subtracted it from the hadron kinetic energy at the TPC front face to evaluate the kinetic energy at each slab until the true interaction point is reached. Since the MC is a pure beam of the hadron of interest and truth information is used to retrieve the interaction point, no correction is applied. Doing so, we obtain the true interacting and incident distributions for the considered hadron and we obtain the true MC cross section as a function of the hadron true kinetic energy.

Figure 4.5 shows the total hadronic cross section for argon implemented in Geant4 10.03.p1 (solid lines) overlaid with the true MC cross section as obtained with the sliced TPC method (markers) for pions on the left and kaons on the right; the total cross section is shown in green, the elastic cross section in blue and the inelastic cross section in red. The nice agreement with the Geant4 distribution and the cross section obtained with the sliced TPC method gives us confidence in the validity of the methodology.

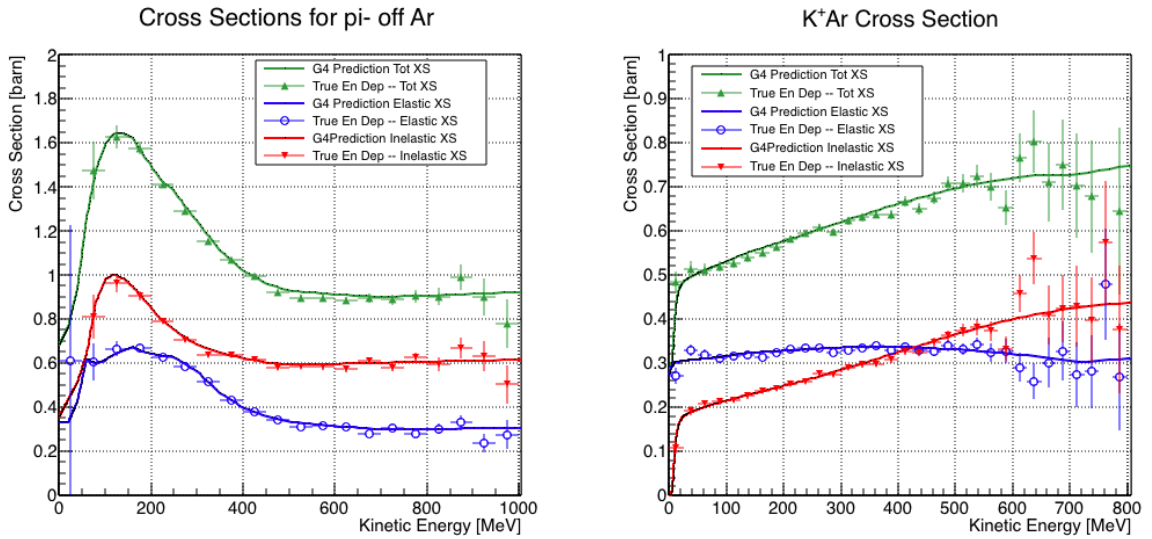


Figure 4.5: Hadronic cross sections for (π^- ,Ar) on the left and (K^+ ,Ar) on the right as implemented in Geant4 10.03.p1 (solid lines) overlaid the true MC cross section as obtained with the sliced TPC method (markers). The total cross section is shown in green, the elastic cross section in blue and the inelastic cross section in red.

1796 **Chapter 5**

1797 **Data and MC preparation for the**
1798 **Cross Section Measurements**

1799 “*Il dolce non lo mangi mai, ma qualche volta ti rifai.*
1800 *Abbracciami*”
1801 – Pietro Ciampi, L’amore e’ tutto qui, 1971 –

1802 This chapter describes the preparatory work done on the the data and Monte Carlo
1803 samples used for the cross section analyses. This entails the choice of the datasets
1804 and the production of the information needed to construct the Monte Carlo Simula-
1805 tion (section 5.1), the construction and use of said Monte Carlo simulation (section
1806 5.2), the study and optimization of the tracking in the TPC for the cross section
1807 analyses (section 5.5), the calibration of the calorimetry response and related energy
1808 studies (section 5.6).

1809 **5.1 Cross Section Analyses Data Sets**

1810 We choose LArIAT Run-II as the data period for the (π^- ,Ar) and (K^+ ,Ar) total
1811 hadronic cross section analyses. Data taking for the this period started on 03/15/2016

1812 and ended on 07/31/2016. Since we are interested in beamline and TPC information,
1813 we ask basic requirements on the operational status of the time of flight, wire chambers
1814 and TPC to form the good run list for this period, which we informally call “lovely
1815 runs”.

1816 The subset of lovely runs chosen for the (π^- ,Ar) total hadronic cross section
1817 analysis includes only the -60A and -100A magnet configurations in negative polarity,
1818 even if LArIAT explored several other beamline configurations during Run-II. The
1819 -60A and -100A combined data set accounts for approximately 90% of the total Run-
1820 II negative polarity runs. The choice of the main two beamline settings limits the
1821 need for the production of many MC sets and related corrections, still maintaining a
1822 high number of events.

1823 Similarly, the subset of lovely runs chosen for the (K^+ ,Ar) total hadronic cross
1824 section analysis includes only the +60A and +100A magnet configurations in positive
1825 polarity. It should be noted that kaons are extremely rare in the +60A sample, thus
1826 the data sample for the (K^+ ,Ar) cross section after the mass selection is about 90%
1827 +100A runs, as shown in Table 5.1.

1828 For the first measurements in LArIAT that uses both beamline and TPC infor-
1829 mation, we choose strict requirements on the reconstruction of the WC tracks, the
1830 so-called “Picky Track” sample (see Section 3.2.2). This choice presents two ad-
1831 vantages: the uncertainty on the momentum reconstruction for the “Picky Tracks”
1832 sample is smaller compared to the “High Yield” sample, and the comparison with
1833 the beamline MC results is straightforward. A possible future update and cross check
1834 of these analysis would be the use of the High Yield sample, where the statistics is
1835 about three times higher.

1836 The breakdown of beamline events as a function of the magnets settings is shown
1837 in Table 5.1. The choice of the data sets determines the production of beamline MC
1838 and serves as basis for the production of Data Driven MC, as shown in the next

1839 sections.

1840 **5.2 Construction of a Monte Carlo Simulation for** 1841 **LArIAT**

1842 For the simulation of LArIAT events and for the simulation of the datasets' particle
1843 make up, we use a combination of two MC generators: the G4Beamline Monte Carlo
1844 and the Data Driven single particle Monte Carlo (DDMC). We use the G4Beamline
1845 MC to simulate the particle transportation in the beamline and calculate the particle
1846 composition of the beam just after the fourth Wire Chamber (WC4). In order to
1847 simulate the beamline particles after WC4 and in the TPC, we use the DDMC.

1848 **5.2.1 G4Beamline**

1849 G4Beamline simulates the beam collision with the LArIAT secondary target, the
1850 energy deposited by the particles in the LArIAT beamline detectors, and the action
1851 of the LArIAT magnets, effectively accounting for particle transportation through the
1852 beamline from the LArIAT target until “Big Disk”, a fictional, void detector located
1853 just before the LArIAT cryostat. At the moment of this writing, G4Beamline does
1854 not simulated the responses of the beamline detectors. It is possible to interrogate the
1855 truth level information of the simulated particles in several points of the geometry.
1856 In order to ease the handshake between G4Beamline and the DDMC, we ask for
1857 the beam composition just after WC4. Since LArIAT data are taken under different

	I = 60 A	I = 100 A	Total
Data Events after $\pi/\mu/e$ Mass Selection	67068	71413	138481
Data Events after K Mass Selection	274	2563	2837

Table 5.1: Number of data events which fit the $\pi/\mu/e$ or K mass hypothesis as a function of magnet settings.

beam conditions, we need to simulate separately the beam composition according to the magnets' settings and the secondary beam intensity with G4Beamline. For the pion cross section analysis the relevant beam conditions are secondary beam energy of 64 GeV, negative polarity magnet with current of 100 A and 60 A. For the kaon cross section analysis the relevant beam conditions is a secondary beam energy of 64 GeV, positive polarity magnet with current of 100 A.

Beam Composition for Negative Pion Cross Section

Even if pions are by far the biggest beam component in negative polarity runs, the LArIAT tertiary beam is not a pure pion beam. While useful to discriminate between pions, kaons, and protons, the beamline detectors are not sensitive enough to discriminate among the lighter particles in the beam: electrons, muons and pions fall under the same mass hypothesis. Thus, we need to assess the contamination from beamline particles other than pions in the event selections used for the pion cross section analysis and correct for its effects. The first step of this process is assessing the percentage of electrons and muons in the $\pi/\mu/e$ beamline candidates via the G4Beamline MC. Since the beamline composition is a function of the magnet settings, we simulate separately events for magnet current of -60A and -100A. Figure 5.1 shows the momentum predictions from G4Beamline overlaid with data for the 60A runs (left) and for the 100A runs (right). The predictions for electrons, muons and pions have been staggered and their sum is area normalized to data. Albeit not perfect, these plots show a reasonable agreement between the momentum shapes in data and MC. We attribute the difference in shape to the lack of simulation of the WC efficiency in the MC which is momentum dependent and leads to enhance the number events in the center of the momentum distribution.

Table 5.2 shows the beam composition per magnet setting after the mass selection according to the G4Beamline simulation.

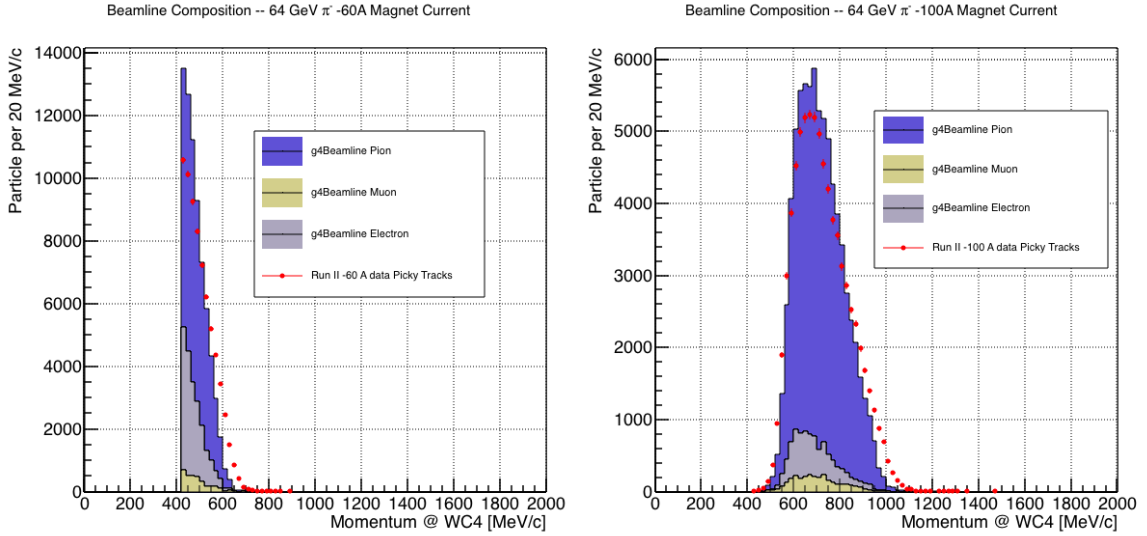


Figure 5.1: Beam composition for the -60A runs (left) and -100A runs (right). The solid blue plot represents the simulated pion content, the yellow plot represents the simulated muon content and the grey plot represents the simulated electron content. The plots are area normalized to the number of data events, shown in red.

	I = -60 A	I = -100 A
G4Pions	68.8 %	87.4 %
G4Muons	4.6 %	3.7 %
G4Electrons	26.6 %	8.9 %

Table 5.2: Simulated beamline composition per magnet settings

1884 The estimated beam composition is used as a basis to estimate the background
1885 contamination in the (π^- ,Ar) cross section measurement, whose full treatment is
1886 described in section 5.3.

1887 **Beam Composition for Positive Kaon Cross Section**

1888 In the positive polarity runs, the tertiary beam composition is mainly pions and
1889 protons. The left side of Figure 5.2 shows the predictions for the momentum spectra
1890 for the 100A positive runs according to G4Beamline (solid colors) overlaid with data
1891 (black points). Since the LArIAT beamline detectors can discriminate between kaons
1892 and other particles, we do not rely on the G4Beamline simulation to estimate the
1893 beamline contamination in the pool of kaon candidates (as in the case of the pion
1894 cross section), but rather we use a data drive approach. The basic idea of this data
1895 driven approach is to estimate the bleed over from high and low mass peaks under the
1896 kaon peak by fitting the tails of the $\pi/\mu/e$ and proton mass distributions, as shown
1897 in Figure 5.2 right side. Since the shape of the tails is unknown, the estimate is done
1898 multiple times varying the range and shape for reasonable functions. For example, to
1899 estimate the proton content under the kaon peak, we start by fitting the left tail of
1900 the proton mass distribution with a gaussian function between $650 \text{ MeV}/c^2$ and $750 \text{ MeV}/c^2$. We extend the fit function under the kaon peak and integrate the extended
1901 fit function between $350-650 \text{ MeV}/c^2$. We integrate the mass histogram in the same
1902 range and calculate the proton contamination as the ratio between the two integrals.
1903 We repeat this procedure for several fit shapes (gaussian, linear and exponential
1904 functions) and tail ranges. Finally, we calculate the contamination as the weighted
1905 average of single estimates, where the weights are calculated to be the $1/\chi^2$ of the
1906 tail fits. The procedure is repeated for lighter particles mass peak independently.
1907 With 12 iterations of this method we find a proton contamination of $0.2 \pm 0.5 \%$
1908 and a contamination from the lighter particles of $5 \pm 2 \%$. The estimate of the

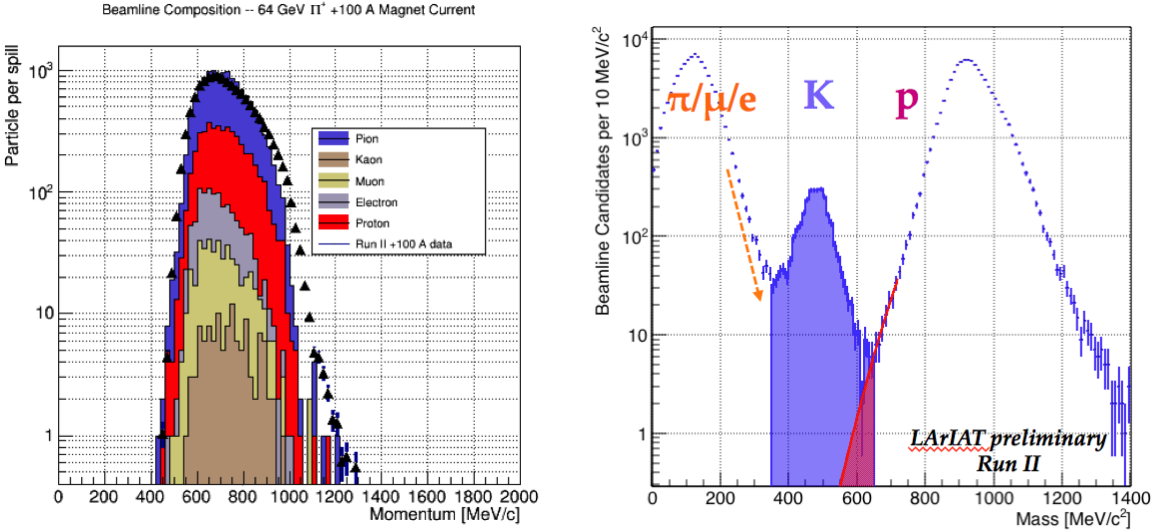


Figure 5.2: *Left:* Beam composition for the +100A runs after WC4 (no mass selection applied). The solid colors represent the contributions from the G4Beamline simulated particles: blue plot represents the simulated pion content, the yellow plot represents the simulated muon content and the grey plot represents the simulated positron content, the red the proton content and the mustard the kaon content. The plots are area normalized to the number of data events, shown in black. *Right:* Mass distribution for the Run-II positive runs, where the area under the kaon mass peak is highlighted in purple. The area under the extension of a possible fit for the proton tail is highlighted in red.

1910 proton background is currently not used in the kaon cross section analysis, but it is
 1911 a fundamental step to retrieve the true kaon cross section which will be implemented
 1912 in the analysis next step.

1913 5.2.2 Data Driven MC

1914 The Data Driven single particle Monte Carlo (DDMC) is a single particle gun which
 1915 simulates the particle transportation from WC4 into the TPC leveraging on the beam-
 1916 line data information. The DDMC uses the data momentum and position at WC4
 1917 to derive the event generation: a general sketch of the DDMC workflow is shown in
 1918 Figure 5.3.

1919 When producing a DDMC sample, beamline data from a particular running pe-
 1920 riod and/or running condition are selected first. For example, data for the negative

1921 60A runs and for the negative 100A runs inform the event generation stage of two
1922 different DDMC samples. Figure 5.4 schematically shows the data quantities of in-
1923 terest leveraged from data: the momentum (P_x, P_y, P_z) and position (X, Y) at WC4.
1924 For each data event, we obtain the particle position (X, Y) at WC4 directly from
1925 the data measurement; we calculate the components of the momentum using the
1926 beamline measurement of the momentum magnitude in conjunction with the hits on
1927 WC3 and WC4 to determine the direction of the momentum vector, as described in
1928 section 3.2.2. The momentum and position of the selected data form a 5-dimensional
1929 tuple, which we sample thousands of times through a 5-dimensional hit-or-miss sam-
1930 pling procedure to generate the MC events. This generates MC events with the same
1931 momentum and position distributions as data, with the additional benefit of account-
1932 ing for the correlations between the P_x, P_y, P_z, X, Y variables. As an example, the
1933 results of the DDMC generation compared to data for the kaon +100A sample are
1934 shown in figure 5.5 for the P_z, X and Y distributions; as expected, MC and data agree
1935 within the statistical uncertainty by construction. A LArSoft simulation module then
1936 launches single particle MC from $z = -100$ cm (the location of the WC4) using the
1937 MC generated events. The particles are free to decay and interact in their path from
1938 WC4 to the TPC according to the Geant4 simulation.

1939 Using the DDMC technique ensures that the MC and data particles have very
1940 similar momentum, position and angular distributions at WC4 and allows us to use
1941 the MC sample in several occasions: to calibrate the energy loss upstream of the TPC
1942 (see Section 5.4), to estimate the background contamination to the pion cross section
1943 (see Section 5.3), or to study the tracking and the calorimetric performance (sections
1944 5.5 and 5.6). A small caveat is in order here: the DDMC is a single particle Monte
1945 Carlo, which means that the beam pile-up is not simulated.

1946 Six samples are the basis fo the MC used in the pion cross section measurement:
1947 three samples of ~ 340000 pions, muons and electrons to simulate the negative 60A

1948 runs, and three samples of ~ 340000 pions, muons and electrons for the negative 100A

1949 runs.

1950 The MC used for the kaon cross section analysis is a sample of **NUMBERS** kaons.

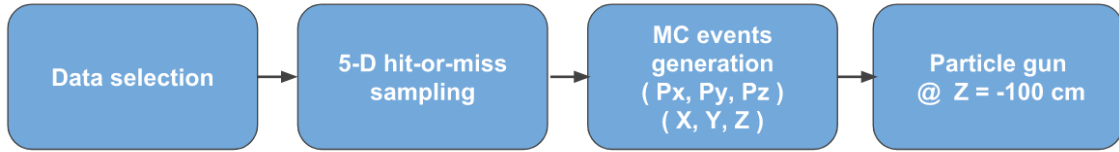


Figure 5.3: Workflow for Data Driven single particle Monte Carlo production.

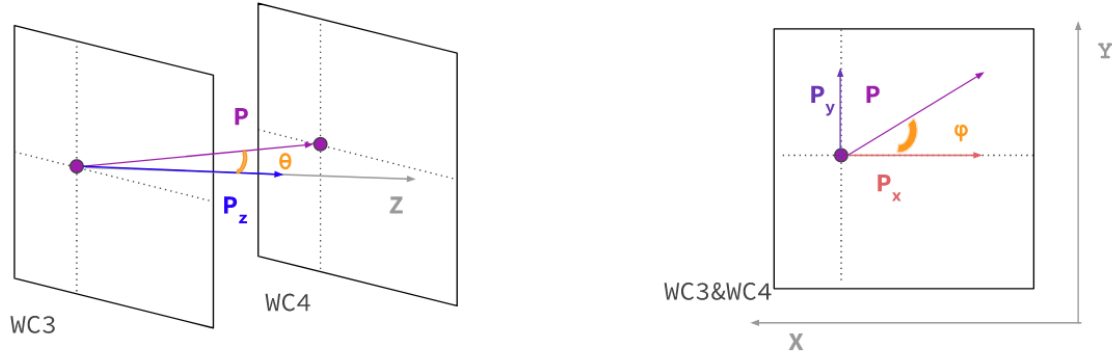


Figure 5.4: Scheme of the quantities of interest for the DDMC event generation:
 P_x, P_y, P_z, X, Y at WC4.

1951 5.3 Estimate of Backgrounds in the Pion Cross 1952 Section

1953 We use the beamline simulation and the DDMC simulation to estimate the back-
1954 ground in the total hadronic pion cross section. Two categories of background exists
1955 for the negative pion cross section measurement: the one related to the pion interac-
1956 tion in the chamber, discussed in Section 5.3.1 and the one related to the beamline
1957 contamination, discussed in Section 5.3.2.

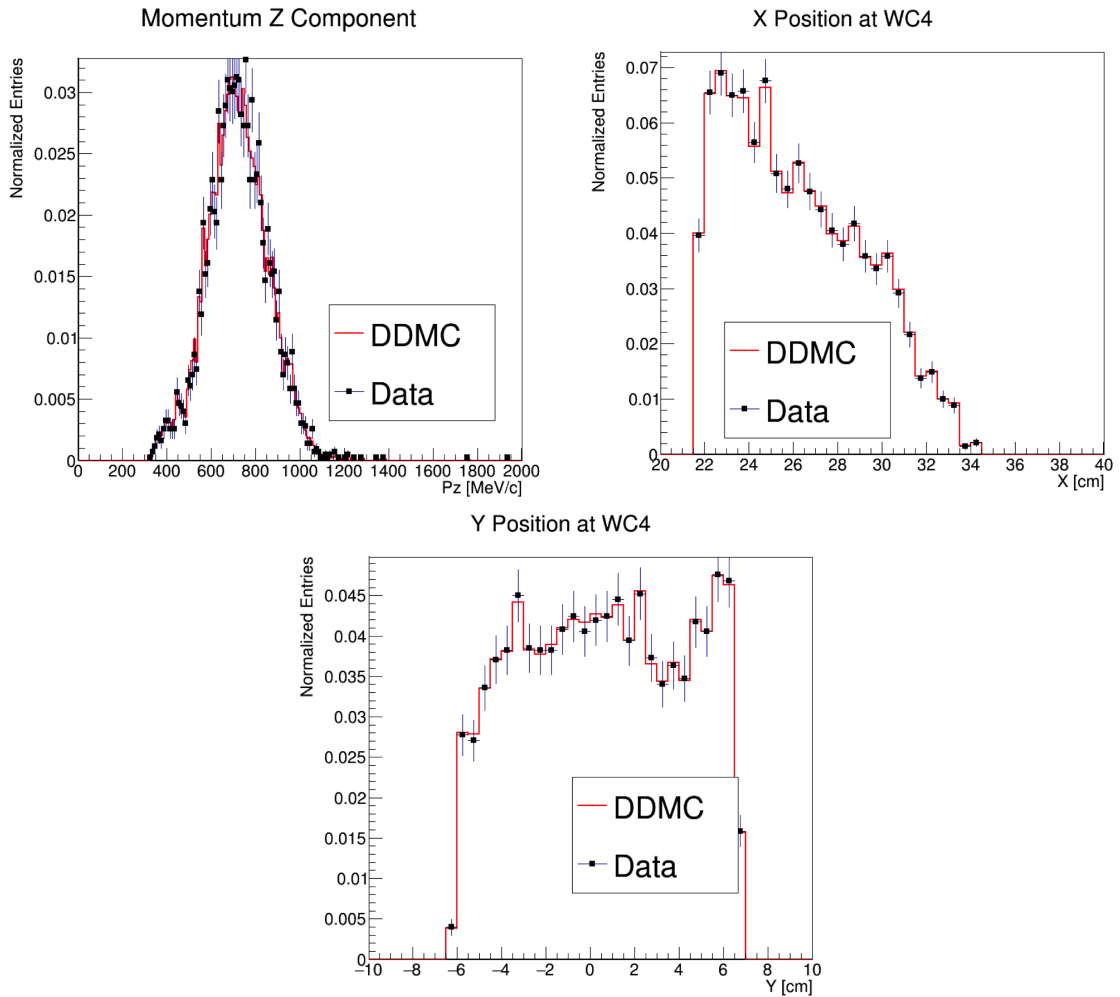


Figure 5.5: Comparison between generated quantities and data distributions for the 100A kaon sample: Z component of the momentum at WC4 (top left), X position at Wire Chamber 4 (top right), Y position at Wire Chamber 4 (bottom).

1958 **5.3.1 Background from Pion Capture and Decay**

1959 Our goal is to measure the total hadronic cross section for negative pions in argon.
1960 Since pion capture can be classified as an electromagnetic process and pion decay is a
1961 week process, capture and decay represent unwanted interactions. We present here a
1962 study of capture and decay in Monte Carlo and the solution we adopted to mitigate
1963 their occurrence in the data sample.

1964 For this MC study, we use a sample of MC pions generated according to the
1965 -60A beam profile with the DDMC (see Section 5.2.2). It is important to notice
1966 that capture occurs predominantly at rest, while decay may occur both in flight and
1967 at rest. Thus, we can highly mitigate capture and decay at rest by removing pions
1968 which would release all their energy in the TPC and stop. This translates into a
1969 momentum selection, where we keep only events whose WC momentum is above a
1970 certain threshold. Figure 5.6 shows the true momentum distribution for the primary
1971 pions¹ that arrive to the TPC (pink), that capture (green) or decay (blue) inside the
1972 TPC, on a linear and log scale vertical axis.

1973 In order to choose the selection value for the wire chamber momentum, it is
1974 beneficial to estimate the ratio of events which capture or decay that survive the
1975 selection in MC as a function of the momentum threshold, and compare it with the
1976 survival ratio for all events. This is done in figure 5.7. We define the survival ratio
1977 simply as the number of events surviving the true momentum selection divided by
1978 the number of events of that category. We calculate the survival ratio separately for
1979 the three event categories explained above: total (pink), capture (green) and decay
1980 (blue). Selecting pions with momentum greater than 420 MeV/c reduces the capture
1981 events by 99% while maintaining about 80% of the total data sample. Figure 5.8

1. We use here the Geant4 denomination “primary” to indicate that the pion considered does not undergo interactions modifying its energy before getting to the TPC. In fact, not every pion shot from wire chamber four will arrive to the TPC as primary, some will decay or interact before the TPC.

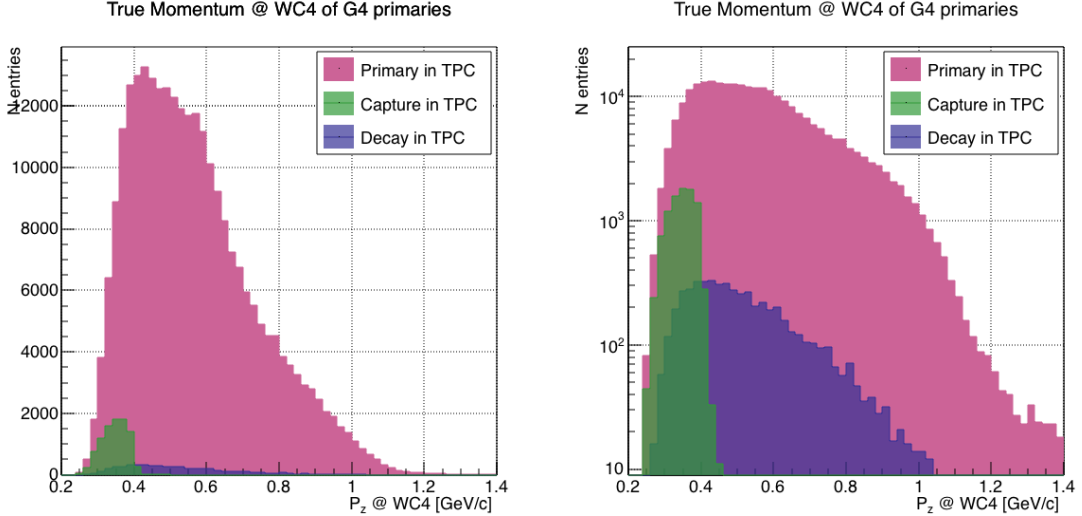


Figure 5.6: True momentum distribution at wire chamber 4 for every simulated pion arriving in the TPC (pink), ending its life in capture (green) or in decay (blue) in the TPC, linear vertical axis on the left, logarithmic on the right.

1982 shows the ratio of events which end their life in capture (green) or decay (blue) over
 1983 the total number of events as a function of the true momentum at wire chamber
 1984 four. This ratio is slightly dependent on the inelastic cross section implemented in
 1985 Geant4, as we are able to register a pion capture (or decay) only if it did not interact
 1986 inelastically in the TPC. We choose a momentum threshold of 420 MeV/c because the
 1987 percentage of capture events drops below 1% and the percentage of decays is never
 1988 above 2% for momenta greater than 420 MeV/c. After the momentum selection, we
 1989 evaluate the contribution of capture and decay to be a negligibly small background to
 1990 the cross section measurement compared to the background related to the beamline.

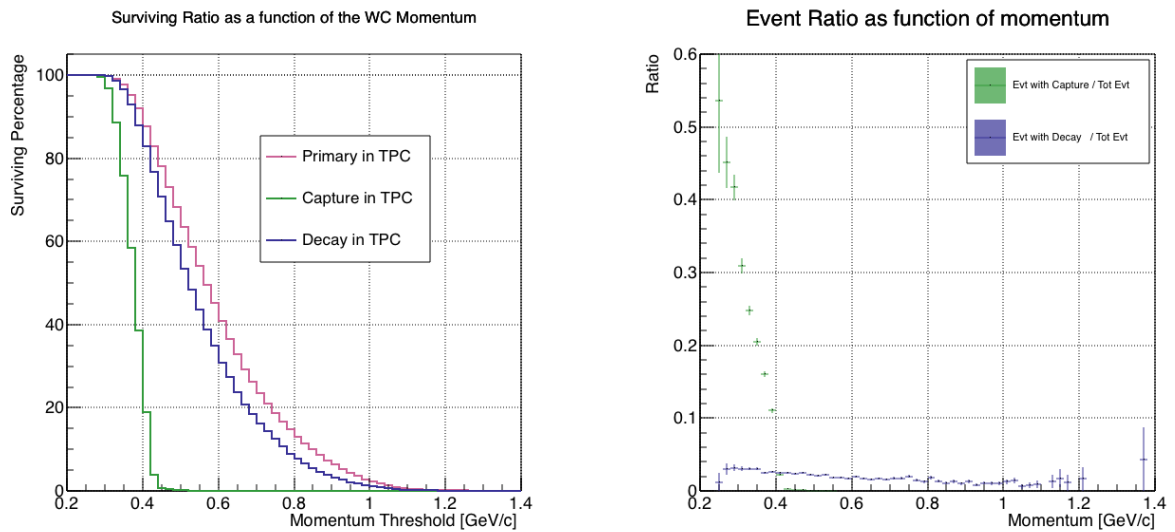


Figure 5.7: Survival ratio as a function of selection threshold on true momentum at wire chamber four for every simulated pion arriving in the TPC (pink), capture (green) or in decay (blue).

Figure 5.8: Ratio between the capture (green) and decay (blue) events over the total number of events as a function of the true momentum at wire chamber four.

1991 **5.3.2 Contributions from the Beamline Background**

1992 We define beamline background every TPC track matched to the WC track which is
1993 not a primary pion. Potentially, there are 4 different types of beamline background:

1994 1) electrons,

1995 2) muons,

1996 3) secondaries from pion events,

1997 4) matched pile up events.

1998 The first step to quantify the effect of the beamline background on the pion cross
1999 section is to estimate what percentage of events used in the cross section calculation
2000 is not a primary pion. We start by noting that the last type of background, the
2001 “matched pile up” events, is a negligible fraction, because of the definition of the
2002 WC2TPC match: we deem the probability of a single match with a halo particle in
2003 the absence of a beamline particle² negligibly small. As shown in Section 5.2.1, we
2004 use G4Beamline to estimate the percentage of pions, muons and electrons at WC4,
2005 obtaining the composition shown in Table 5.2. The next step is to simulate those
2006 pions, muons and electrons from WC4 to the TPC with the DDMC and evaluate their
2007 contribution to the cross section. To do so, we start by simulating the same number of
2008 electrons, muons and pions with the DDMC and we apply the same selection filters on
2009 the three samples. The number of events per particle species surviving this selection
2010 is shown on table 5.3. In order to reproduce the closest make up of the beam to data,
2011 we weight each event of a given particle species according to the estimated beam
2012 composition. In case of 60A runs, for example, the weights are 0.688 for pions, 0.046
2013 for muons and 0.266 for electrons.

2. Events with multiple WC2TPC matches are always rejected.

	Magnet Current -60A			Magnet Current -100 A		
	MC π^-	MC μ^-	MC e^-	MC π^-	MC μ^-	MC e^-
Total Initial events	334500	334500	334500	344500	344500	344500
After Multiplicity Rejection	330668	333420	198065	326576	344208	201380
After WC2TPC Selection	218239	296333	91139	230418	300228	98834
Evts After Shower Rejection	208063	288914	20293	219882	293585	17780
Selection Survival Rate	62.3%	86.6%	6.1%	63.8%	85.5%	5.2%
Beam Composition @WC4	68.8%	4.6 %	26.6 %	87.4 %	3.7 %	8.9 %
Beam Composition @TPC FF	88.5%	8.2%	3.3 %	94.0%	5.3%	0.7%

Table 5.3: MC selection flow per particle species.

2014 It should be noted that pions may interact hadronically in the steel or in the
 2015 non-instrumented argon upstream to the TPC front face while travelling the length
 2016 of between WC4 and the TPC. Or, they could decay in flight between WC4 and the
 2017 TPC. One of the interaction products can leak into the TPC and be matched with the
 2018 WC track, contributing to the pool of events used for the cross section calculation. We
 2019 call this type of particles “secondaries” from pion events, with a terminology inspired
 2020 by Geant4. We estimate the number of secondaries using the DDMC pion sample.
 2021 The percentage of secondaries is given by the number of matched WC2TPC tracks
 2022 whose corresponding particle is not flagged as primary by Geant4. The secondary to
 2023 pion ratio is 4.9% in the 60A sample and 4.3% in the 100A sample.

2024 We evaluate the beamline background contribution to the cross section by pro-
 2025 ducing the interacting and incident histograms for the events surviving the selection,
 2026 staggering the contributions for each particle species, as shown in Figure 5.9. From
 2027 those histograms, we are able to evaluate the contribution of pions and beamline
 2028 backgrounds to each bin of the interacting and incident histograms separately and
 2029 obtain the relative pion content. The relative pion content in each bin for the inter-
 2030 acting and incident histograms represents the correction applied to data. We take

here the interacting histogram as example, noting that the derivation of the correction for the incident histogram is identical. The number of entries in each bin of the interacting plot (Figure 5.9 left) is $N_{\text{Int}}^{\text{TOT}}(E_i)$, equal to the sum of the pions and beamline backgrounds in that bin, namely

$$N_{\text{Int}}^{\text{TOT}}(E_i) = N_{\text{Int}}^{\pi}(E_i) + \underbrace{N_{\text{Int}}^{\mu}(E_i) + N_{\text{Int}}^e(E_i) + N_{\text{Int}}^{\text{Secondary}}(E_i)}_{B_{\text{Int}}(E_i)}. \quad (5.1)$$

Thus, the relative pion content to each bin in MC can be calculated as follows

$$C_{\text{Int}}^{\pi MC}(E_i) = \frac{N_{\text{Int}}^{\pi MC}}{N_{\text{Int}}^{\text{TOTMC}}(E_i)} = \frac{N_{\text{Int}}^{\text{TOTMC}}(E_i) - B_{\text{Int}}^{MC}(E_i)}{N_{\text{Int}}^{\text{TOTMC}}(E_i)}. \quad (5.2)$$

In order to evaluate the pion content of each bin in data, we scale the measured bin by the corresponding relative pion content found in MC, as follows

$$N_{\text{Int}}^{\pi RecoData} = N_{\text{Int}}^{\text{TOTData}}(E_i) - B_{\text{Int}}^{\text{Data}}(E_i) = C_{\text{Int}}^{\pi MC}(E_i)N_{\text{Int}}^{\text{TOTData}}(E_i). \quad (5.3)$$

The pion content is evaluated separately in the interacting and incident histograms. Their ratio determines a correction to the measured raw cross section. For example, the measured raw cross section of a sample with enhanced muons content will tend to be lower than the raw cross section of a muon free sample. This is because most of the muons will cross the TPC without stopping, thus contributing almost exclusively to the incident histogram, forcing the pion content to be lower in the incident histogram than in the interacting; thus, the correction will tend to enhance the cross section.

2046 5.4 Estimate of Energy Loss before the TPC

2047 The beamline particles travel a path from where their momentum is measured in
2048 the beamline until they are tracked again inside the TPC. In the LArIAT geometry,
2049 a particle leaving the WC4 will encounter the materials listed in Table 5.4 before
2050 being registered again. The energy lost by the particle in this non-instrumented
2051 material modifies the particle’s kinetic energy and directly affects the cross section
2052 measurement, as shown in equation 4.5.

Material	density [g/cm ³]	width [cm]
Fiberglass laminate (G10)	1.7	1.28
Liquid Argon	1.4	3.20
Stainless Steel	7.7	0.23
Titanium	4.5	0.04
Air	$1.2 \cdot 10^{-3}$	89.43
Plastic Scintillator	1.03	1.20 (+ 1.30)

Table 5.4: LArIAT material budget from WC4 to the TPC Front Face.

We derive an estimate of the energy loss between the beamline momentum measurement and the TPC (E_{loss}) from the pion and kaon DDMC samples, since this quantity is not measurable directly on data. The E_{loss} distribution for the 60A and 100A pion sample is shown in figure 5.10, left and right respectively. A clear double peaked structure is visible, which is due to the particles either missing or hitting the HALO paddle: a schematic rendering of this occurrence is shown in figure 5.11. The kinematic at WC4 determines the trajectory of a particle and whether or not it will hit the halo paddle. In figure 5.12 , we plot the true horizontal component of the momentum P_x versus the true X position at WC4 for pions missing the halo paddle (left) and for pions hitting the halo paddle (right) for the 60A MC simulation runs – analogous plots are obtained with the 100A simulation. These distributions can be separated drawing a line in this position-momentum space. We use a logistic regression [13] as a classifier to find the best separating line, shown in both plots as the red

line. We classify as “hitting the halo paddle” all pions whose P_x and X are such that

$$P_x + 0.02 * X - 0.4 < 0$$

and as “missing the halo paddle” all pions whose P_x and X are such that

$$P_x + 0.02 * X - 0.4 > 0,$$

where the coefficients of the line are empirically found by the logistic regression estimation. Overall, this simple method classifies in the right category (hit or miss) about 86% of the pion events. In MC, we assign $E_{loss} = 32 \pm 4$ MeV for pion events classified as “hitting the halo paddle”; we assign $E_{loss} = 24 \pm 3$ MeV for pion events classified as “missing the halo paddle”. We apply the same classifier on data. A scan of the simulated geometry showed an excess of 3 cm of uninstrumented argon compared with the surveyed detector geometry. We account for this difference by assigning in data $E_{loss} = 24 \pm 6$ MeV for pion events classified as “hitting the halo paddle” and $E_{loss} = 17 \pm 6$ MeV for pion events classified as “missing the halo paddle”, where the uncertainty is derived as the standard deviation of the double peaked distribution.

The summary of the values for used for E_{Loss} for the pion sample is listed in table 5.5 with the analogous results for the study on the kaon case.

	E_{loss} [MeV]	
	Hitting Halo	Missing Halo
Pion MC	32 ± 4	24 ± 3
Pion Data	25 ± 6	17 ± 6
Kaon MC	37 ± 5	31 ± 4
Kaon Data	26 ± 6	22 ± 6

Table 5.5: Energy loss for pions and kaons.

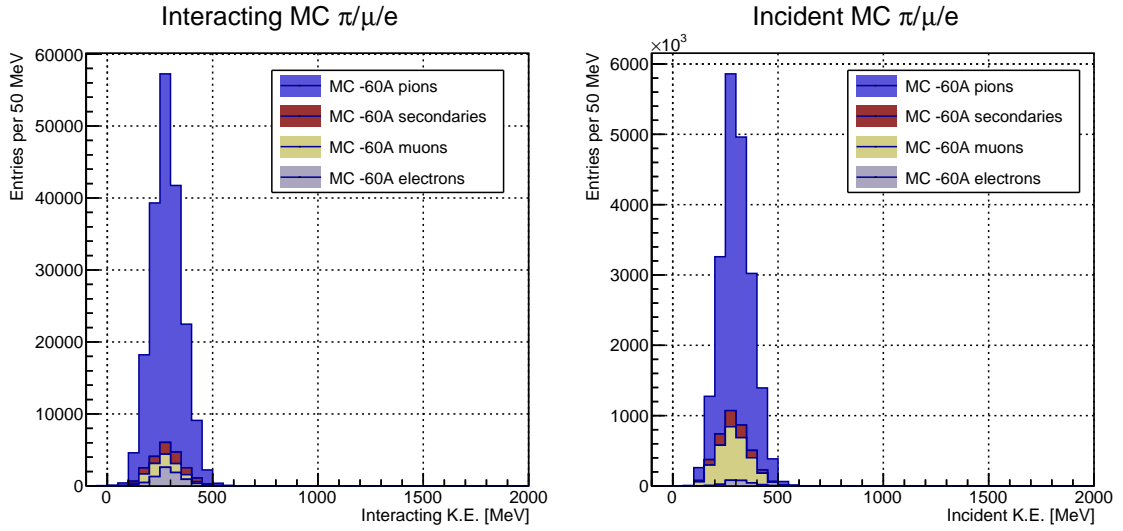


Figure 5.9: Left: staggered contributions to the interacting kinetic energy distribution for electron (grey), muons (yellow) and pion (blue) in the 60A simulation sample. Right: staggered contributions to the incident kinetic energy distribution for electron (grey), muons (yellow) and pion (blue) in the 60A simulation sample.

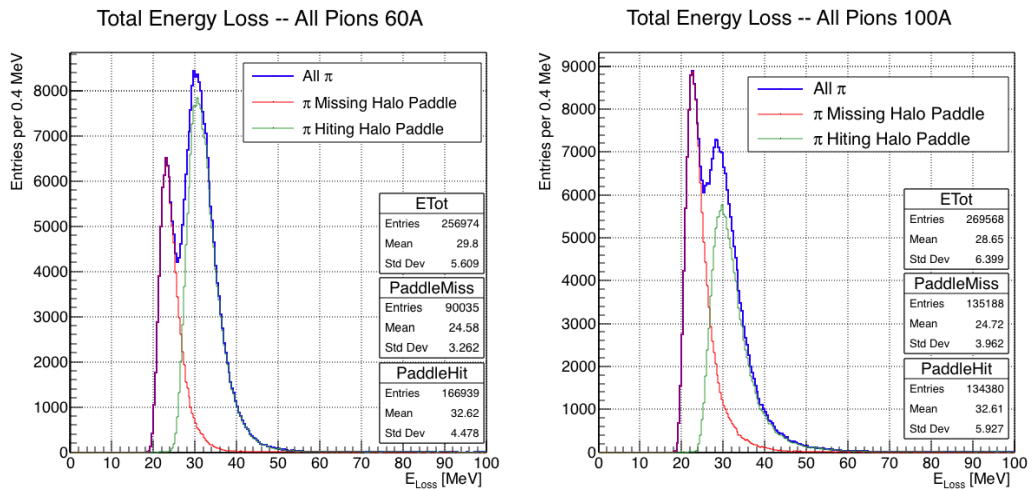


Figure 5.10: True energy loss between WC4 and the TPC front face according to the MC simulation of negative pions of the 60A runs (left) and of the 100A runs (right). The distribution for the whole data sample is shown in blue, the distribution for the pions missing the halo is shown in red, and the distribution for the pions hitting the halo is shown in green.

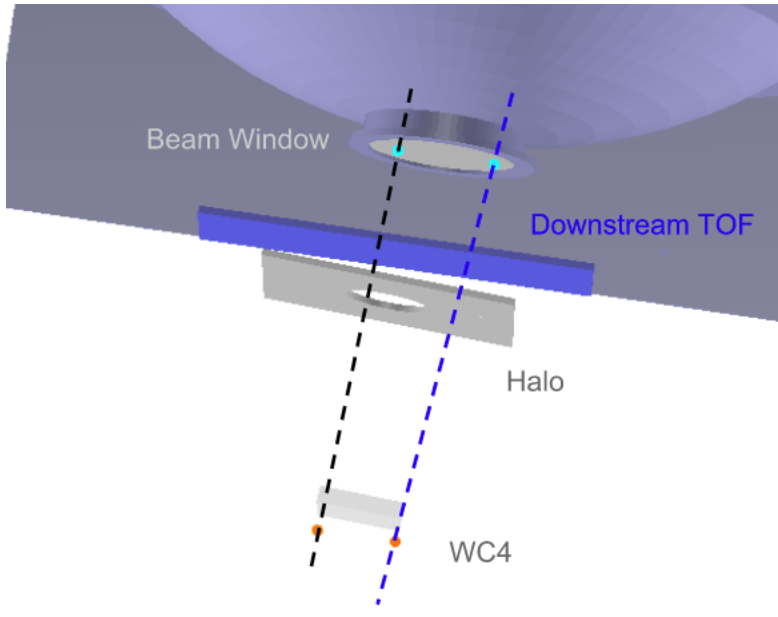


Figure 5.11: Schematic rendering of the particle path between WC4 and the TPC front face. The paddle with the hollow central circle represents the Halo paddle. We illustrate two possible trajectories: in black, a trajectory that miss the paddle and goes through the hole in the Halo, in blue a trajectory that hits the Halo paddle and goes through the scintillation material.

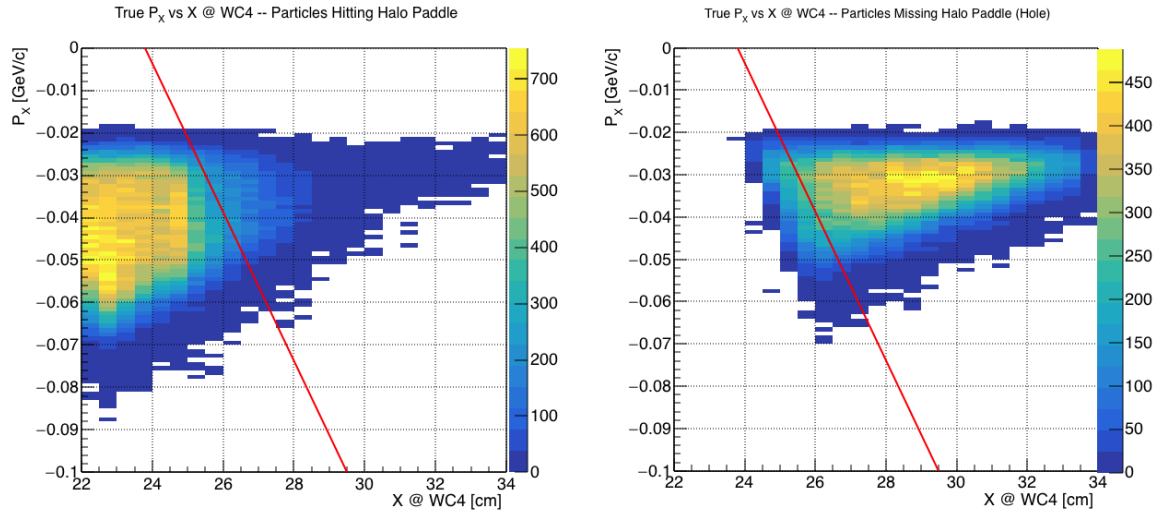


Figure 5.12: Horizontal component of the true momentum vs the horizontal position at WC4 for MC simulated pions of the 60A runs. The plot on the left shows the distribution for pion that miss the halo paddle and the plot on the right shows the distributions for pions that hit the halo. The form of the classifier is overlaid to both plots (red line).

2066 5.5 Tracking Studies

2067 In this section, we describe three studies. The first is a justification of the selection
2068 criteria for the beamline handshake with the TPC information. We perform this
2069 study to boost the correct identification of the particles in the TPC associated with
2070 the beamline information, while maintaining sufficient statistics for the cross section
2071 measurement. The second study is an optimization of the tracking algorithm, with
2072 the scope of maximizing the identification of the hadronic interaction point inside the
2073 TPC. These two studies are related, since the optimization of the tracking is per-
2074 formed on TPC tracks which have been matched to the wire chamber track; in turn,
2075 the tracking algorithm for TPC tracks determines the number of reconstructed tracks
2076 in each event used to try the matching with the wire chamber track. Starting with
2077 a sensible tracking reconstruction, we perform the WC2TPC matching optimization
2078 first, then the tracking optimization. The WC2TPC match purity and efficiency are
2079 then calculated again with the optimized tracking.

2080 The third study is an evaluation of the angular resolution of the tracking algorithm
2081 in data and MC, which is particularly important in the context of the cross section
2082 analyses.

2083 5.5.1 Study of WC to TPC Match

2084 Plots I want in this section:

2085 1. WC2TPC MC DeltaX, DeltaY and α

2086 Scope of this study is assessing the goodness of the wire chamber to TPC match
2087 on Monte Carlo and decide the selection values we will use on data. A word of caution
2088 is necessary here. With this study, we want to minimize pathologies associated with
2089 the presence of the primary hadron itself, e.g. the incorrect association between the

2090 beamline hadron and its decay products inside the TPC. Assessing the contamination
2091 from pile-up³, albeit related, is beyond the scope of this study.

2092 In MC, we are able to define a correct WC2TPC match using the Geant4 truth
2093 information. We are thus able to count how many times the WC tracks is associated
2094 with the wrong TPC reconstructed track.

2095 We define a correct match if the all following conditions are met:

- 2096 - the length of the true primary Geant4 track in the TPC is greater than 2 cm,
2097 - the length of the reconstructed track length is greater than 2 cm,
2098 - the Z position of the first reconstructed point is within 2 cm from the TPC
2099 front face
2100 - the distance between the reconstructed track and the true entering point is the
2101 minimum compared with all the other reconstructed tracks.

2102 In order to count the wrong matches, we consider all the reconstructed tracks
2103 whose Z position of the first reconstructed point lies within 2 cm from the TPC front
2104 face. Events with true length in TPC < 2 cm are included. Since hadrons are shot
2105 100 cm upstream from the TPC front face, the following two scenarios are possible
2106 from a truth standpoint:

- 2107 [Ta] the primary hadron decays or interact strongly before getting to the TPC,
2108 [Tb] the primary hadron enters the TPC.

2109 As described in Section 4.2, we define a WC2TPC match according to the relative
2110 position of the WC and TPC track parametrized with ΔR and the angle between

3. We remind the reader that the DDMC is a single particle Monte Carlo, where the beam pile up is not simulated.

them, parametrized with α . Once we choose the selection values r_T and α_T to determine a reconstructed WC2TPC match, the following five scenarios are possible in the truth to reconstruction interplay :

- 1) only the correct track is matched
- 2) only one wrong track is matched
- 3) the correct track and one (or more) wrong tracks are matched
- 4) multiple wrong tracks matched.
- 5) no reconstructed tracks are matched

Since we keep only events with one and only one match, we discard cases 3), 4) and 5) from the events used in the cross section measurement. For each set of r_T and α_T selection value, we define purity and efficiency of the selection as follows:

$$\text{Efficiency} = \frac{\text{Number of events correctly matched}}{\text{Number of events with primary in TPC}}, \quad (5.4)$$

$$\text{Purity} = \frac{\text{Number of events correctly matched}}{\text{Total number of matched events}}. \quad (5.5)$$

Figure 5.13 shows the efficiency (left) and purity (right) for WC2TPC match as a function of the radius, r_T , and angle, α_T , selection value. It is apparent how both efficiency and purity are fairly flat as a function of the radius selection value at a given angle. This is not surprising. Since we are studying a single particle gun Monte Carlo sample, the wrong matches can occur only for mis-tracking of the primary or for association with decay products; decay products will tend to be produced at large angles compared to the primary, but could be fairly close to the in x and y projection of the primary. The radius cut would play a key role in removing pile up events.

2130 For LArIAT cross section measurements, we generally prefer purity over efficiency,
 2131 since a sample of particles of a pure species will lead to a better measurement. Ob-
 2132 viously, purity should be balanced with a sensible efficiency to avoid rejecting the
 2133 whole sample.

2134 We choose $(\alpha_T, r_T) = (8 \text{ deg}, 4 \text{ cm})$ and get a MC 85% efficiency and 98% purity
 2135 for the kaon sample and a MC 95% efficiency and 90% purity for the pion sample.

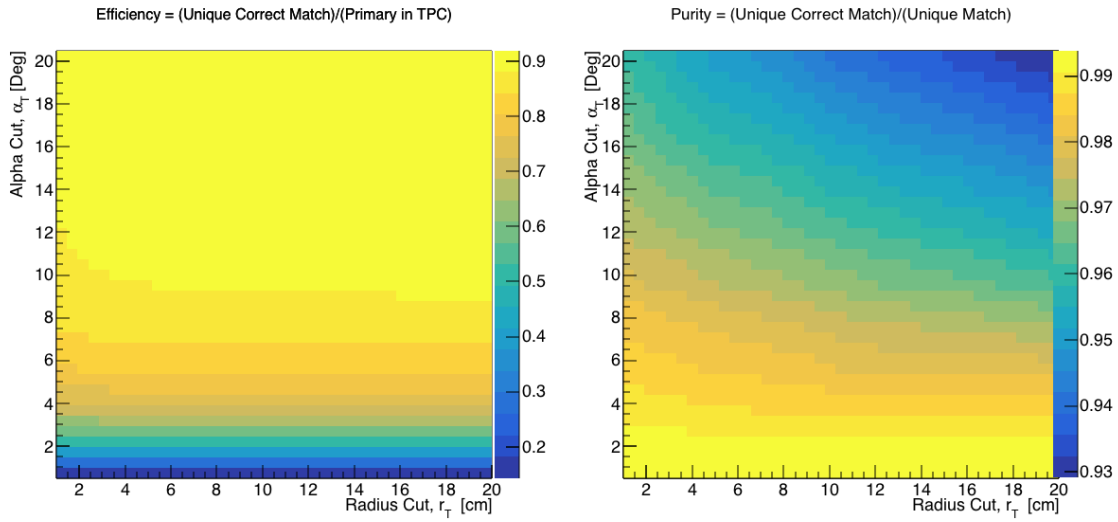


Figure 5.13: Efficiency (left) and purity (right) for WC2TPC match as a function of the radius and angle selections for the kaon sample.

2136 5.5.2 Tracking Optimization

2137 5.5.3 Angular Resolution

2138 Scope of this study is to understand and compare the tracking performances and
 2139 angular resolution of the TPC tracking on data and MC. We use the angular resolution
 2140 of the tracking to determine the value of smallest angle that we can reconstruct with
 2141 a non-zero efficiency, effectively determining a selection on the angular distribution
 2142 of the cross section measurement due to the tracking performance. This study is
 2143 performed on the pion sample, but its results are extrapolated to the kaon case.

2144 We start by selecting all the WC2TPC matched tracks used for the cross section
 2145 analysis. These tracks can contain from a minimum of 3 3D-space points to a maxi-
 2146 mum of 240 3D-space points. We fit a line to all the 3D-space points associated with
 2147 the track. For each track we calculate the average distance between each point in
 2148 space and the fit line as follows

$$\bar{d} = \frac{\sum_i^N d_i}{N}, \quad (5.6)$$

2149 where N is the number of 3D-space points of the track and d_i is the distance of the
 2150 i -th space point to the line fit. Several tests to compare the goodness of fit between
 2151 data and MC have been considered. We decided to use \bar{d} for its straightforward
 2152 interpretation. The \bar{d} distribution for data and MC is shown in Figure 5.14 and
 2153 shows a relatively good agreement between data and MC.

2154 A visual representation of the procedure used to evaluate the angular resolution is
 2155 shown in Figure 5.16. For each track, we order the space points according to their Z
 2156 position along the positive beam direction (panel a) and we split them in two sets: the
 2157 first set contains all the points belonging to the first half of the track and the second
 2158 set contains all the points belonging the second half of the track. We remove the last
 2159 four points in the first set and the first four points in the second set, so to have a
 2160 gap in the middle of the original track (panel b). We fit the first and the second set
 2161 of points with two lines (panel c). We then calculate the angle between the fit of the
 2162 first and second half α (panel d). The angle α determines the spatial resolution of
 2163 the tracking. The distributions for data and MC for α are given in Figure 5.15. The
 2164 mean of the data and MC angular resolution are respectively

$$\bar{\alpha}_{Data} = (5.0 \pm 4.5) \text{ deg}, \quad (5.7)$$

$$\bar{\alpha}_{MC} = (4.5 \pm 3.9) \text{ deg}. \quad (5.8)$$

2165 Interaction angles smaller than the angle resolution are indistinguishable for the
2166 reconstruction. Therefore, we assess our ability to measure the cross section to be
2167 limited to interaction angles greater than 5.0 deg. More accurate studies of the angular
2168 resolution as a function of the kinetic energy and track length, albeit interesting, are
2169 left for an improvement of the analysis.

2170 It is beneficial to take a moment to describe the definition of interaction angle.
2171 In case of elastic scattering, the definition is straightforward: the interaction angle is
2172 the angle between the incoming and outgoing pion, i.e.

$$\theta = \cos^{-1} \left(\frac{\vec{p}_{\text{incoming}} \cdot \vec{p}_{\text{outgoing}}}{|\vec{p}_{\text{incoming}}| |\vec{p}_{\text{outgoing}}|} \right). \quad (5.9)$$

2173 In case of inelastic scattering, the presence of several topologies requires a more
2174 complex definition, as shown in figure 5.17. We define the scattering angle as the
2175 biggest of the angles between the incoming pion and the visible daughters, where the
2176 visible daughters are charged particles that travel more than 0.47 cm in the detector
2177 (see panel a); in case all the daughters are invisible, the angle is assigned to be 90
2178 deg (see panel b). We chose this working definition of scattering angle for inelastic
2179 scattering keeping in mind how our tracking reconstruction works: the tracking will
2180 stop correctly in case of all the daughters are not visible in the detector and it is
2181 likely to stop correctly if multiple daughters form an interaction vertex. The only
2182 “dangerous” case is the production of one charged daughter plus neutrals, which we
2183 can study with this working definition of scattering angle (see panel c).

2184 We can see the effects of the angular resolution on the cross section by plotting the
2185 true Geant4 cross section for interaction angles greater than a minimum interaction
2186 angle. Figure 5.18 shows the true Geant4 cross section for interaction angles greater
2187 than 0 deg (green), 4.5 deg (red), 5.0 deg (blue) and 9.0 deg (yellow). A small 0.5 deg
2188 systematic shift between the mean of the data and MC angular resolution is present.

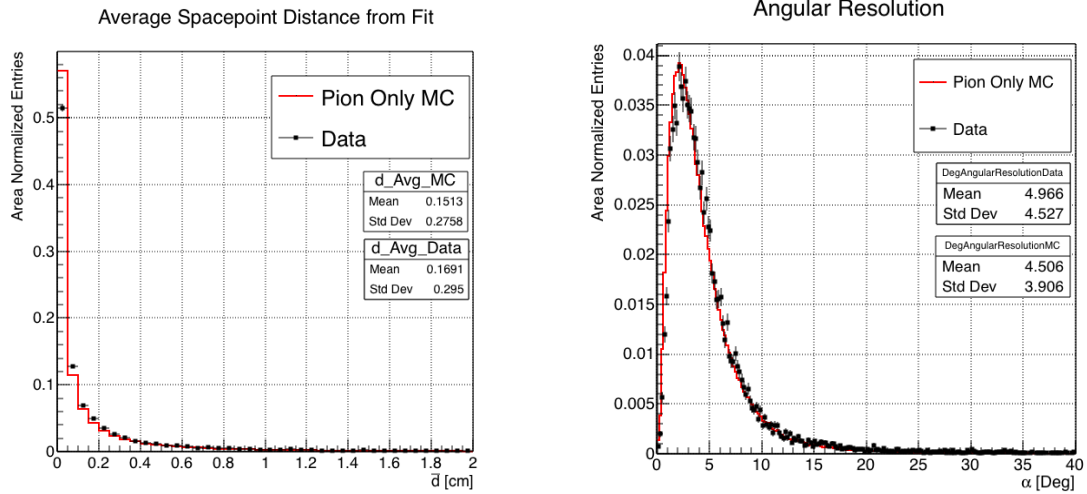


Figure 5.14: Distributions of the average distance between each 3D point in space and the fit line, \bar{d} for the data used in the pion cross section analysis and the pion only DDMC. The distributions are area normalized.

Figure 5.15: Distributions of angular resolution α for data used in the pion cross section analysis and pion only DDMC. The distributions are area normalized.

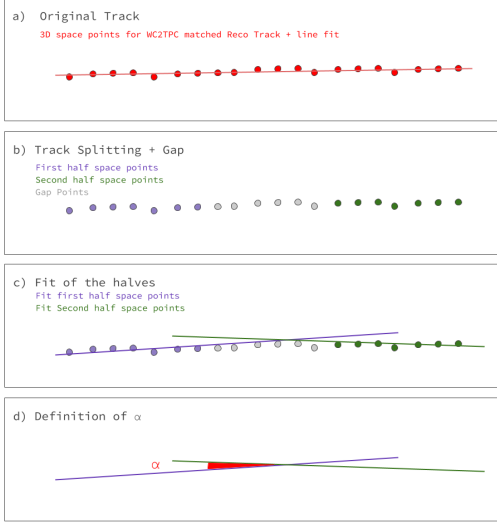


Figure 5.16: A visual representation of the procedure used to evaluate the angular resolution.

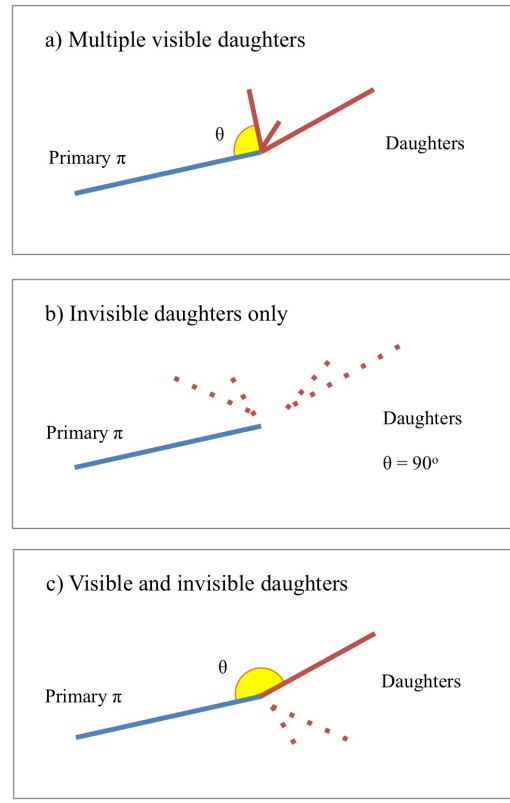


Figure 5.17: A visual representation of the scattering angle definition in case of inelastic scattering.

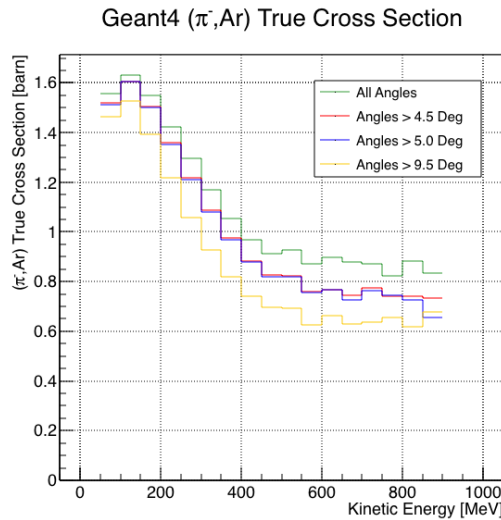


Figure 5.18: True (π^- , Ar) cross section for interaction angles greater than 0 deg (green), 4.5 deg (red), 5.0 deg (blue) and 9.0 deg (yellow).

2189 **5.6 Calorimetry Studies**

2190 The ability to measure the kinetic energy of hadrons in the TPC is fundamental
2191 for the cross section analyses. Thus, we describe first how we calibrate the TPC
2192 calorimetric response (Section 5.6.1) and how we measure the kinetic energy of the
2193 hadrons in the TPC (Section 5.6.2).

2194 **5.6.1 Energy Calibration**

2195 Scope of the energy calibration is to identify the factors which convert the charge
2196 collected (dQ) to energy deposited in the chamber (dE). As described in section
2197 2.1.5, this is a multi-step procedure. In LArIAT, we first correct the raw charge by
2198 the electronic noise on the considered wire [102], then by the electron lifetime [103],
2199 and then by the recombination using the ArgoNeut recombination values. Lastly, we
2200 apply overall calibration of the energy, i.e. we determine the “calorimetry constants”
2201 using the procedure described in this section.

2202 We independently determine the calorimetry constants for Data and Monte Carlo
2203 in the LArIAT Run-II Data samples using a parametrization of the stopping power
2204 (a.k.a. energy deposited per unit length, dE/dX) as a function of momentum. This is
2205 done by comparing the stopping power measured on reconstructed quantities against
2206 the Bethe-Bloch theoretical prediction for various particle species (see Equation 2.1).
2207 We obtain the theoretical expectation for the dE/dX most probable value of pions
2208 (π), muons (μ), kaons (K), and protons (p) in the momentum range most relevant
2209 for LArIAT (Figure 5.19) using the tables provided by the Particle Data Group [100]
2210 for liquid argon [1].

2211 The basic idea of this calibration technique is to utilize a sample of beamline
2212 events with known particle species and momentum to measure the dE/dX of the
2213 corresponding tracks in the TPC. In particular, we decided to use positive pions as

2214 calibration sample and samples from all the other particle species as cross check. Once
2215 the dE/dX of the positive pion sample has been measured at various momenta, we
2216 tune to calorimetry constants within the reconstruction software to align the measured
2217 values to match the theoretical ones found in Figure 5.19.

2218 In data, we start by selecting a sample of beamline positive pion beamline can-
2219 didates without any restriction on their measured momentum⁴. We then apply the
2220 WC2TPC match and subtract the energy loss upstream to the TPC front face, de-
2221 termining the momentum at the TPC front face. For each surviving pion candidate,
2222 we measure the dE/dx at each of the first 12 spacepoints associated the 3D recon-
2223 structed track, corresponding to a ~ 5 cm portion. These dE/dX measurements are
2224 then put into a histogram that corresponds to measured momentum of the track.
2225 The dE/dX histograms are sampled every 50 MeV/c in momentum (e.g. 150 MeV/c
2226 $< P <$ 200 MeV/c, 200 MeV/c $< P <$ 250/c MeV, etc...). This process of selecting,
2227 sampling, and recording the dE/dX for various momentum bins is repeated over the
2228 entire sample of events, allowing us to collect sufficient statistic in most of the mo-
2229 mentum bins between 150 MeV/c and 1100 MeV/c. On average, pions and muons
2230 only lose ~ 10 MeV in this 5 cm section of the track and protons lose ~ 20 MeV. Thus
2231 choosing 50 MeV/c size bins for our histograms covers the energy spread within those
2232 bins due to energy loss from ionization for all the particle species identifiable in the
2233 beamline. Each 50 MeV/c momentum binned dE/dX histogram is now fit with a
2234 simple Landau function. The most probable value (MPV) and the associated error
2235 on the MPV from the fit are extracted and plotted against the theoretical prediction
2236 Figure 5.19. Depending on the outcome of the data-prediction comparison, we modify
2237 the calorimetry constants and we repeat the procedure until a qualitative agreement
2238 is achieved. We perform this tuning for the collection and induction plane separately.
2239 As a cross check to the calorimetry constants determined using the positive pions,

4. it should be noted that some muon and position contamination is present in the π^+ sample

we lock the constants and plot the dE/dx versus momentum distribution of all the other particle species identifiable in the beamline data ($\pi/\mu/e$, K , p, in both polarities) against the corresponding Beth-Bloch prediction. The agreement between data from the other particle species and the predictions is the expected result of this cross check. The results of the tuning and cross check for Run-II data on the collection plane is shown in Figure 5.20 negative polarity data on top, positive polarity data on the bottom.

In MC, we simulate the corresponding positive pion sample with the DDMC (see section 5.2.2) and follow the same steps as in data. More details on the calorimetry tuning can be found in [78].

Add agreement between data and MC for dedx for pions

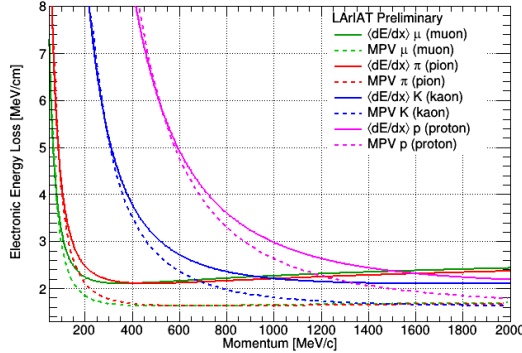


Figure 5.19: Stopping power for pions, muons, kaons, and protons in liquid argon over the momentum range most relevant for LArIAT according to the Beth-Bloch equation. The solid lines represent the prediction for the mean energy dE/dX , while the dashed lines are the predictions for the MPV.

5.6.2 Kinetic Energy Measurement

The measured kinetic energy of a hadron candidate at each argon slab determines which bins of the interacting and incident histograms a selected event is going to fill. In this section, we define the measurement on the kinetic energy and determine the related uncertainty. We will propagate this uncertainty into the cross section

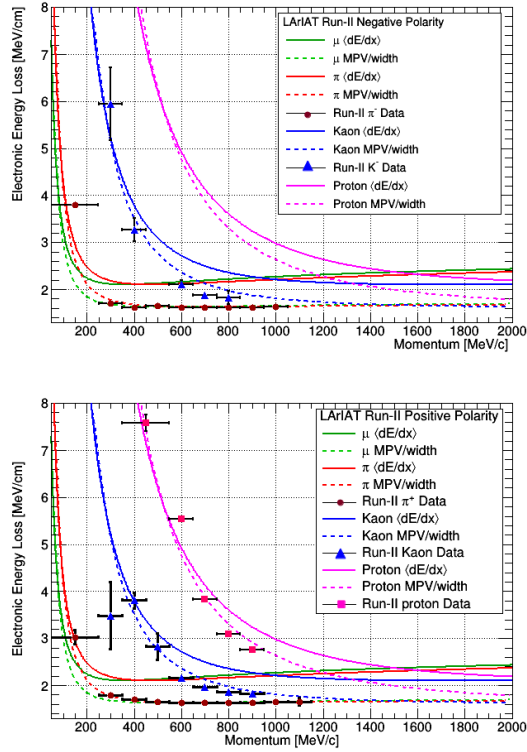


Figure 5.20: Stopping power versus Momentum for Run-II negative (top) and positive (bottom) polarity data. We achieve the agreement between the Bethe-Bloch predictions and the distribution obtained with of the positive pions (top plot, red dots) by tuning the calorimetry constants. Once the calorimetry constants are locked in, the agreement between the other particle species and the Bethe-Bloch predictions follows naturally.

measurement, as discussed in Section 6.1.2 for the pion cross section and in Section ?? for the kaon cross section.

The kinetic energy of a hadron at the j^{th} slice of argon in the TPC is given by

$$KE_j = \sqrt{p_{\text{Beam}}^2 + m_{\text{Beam}}^2} - m_{\text{Beam}}^2 - E_{\text{Loss}} - E_{\text{FF-j}}, \quad (5.10)$$

where p_{Beam} is the momentum measured by the beamline detectors, m_{Beam} is the mass of the hadron as reported in the PDG, E_{Loss} is the energy loss between the beamline and the TPC, and $E_{\text{FF-j}}$ is the energy that the hadron deposited from the

2262 TPC front face until the j^{th} slice. The uncertainty on KE_j is then given by

$$\delta KE_j = \sqrt{\delta p_{Beam}^2 + \delta E_{Loss}^2 + \delta E_{\text{dep FF-j}}^2}, \quad (5.11)$$

2263 where we have dropped the uncertainty on the mass, since it is orders of magnitude
2264 smaller than the other uncertainties. We assume the relative uncertainty on p_{Beam} to
2265 be 2%, and the uncertainty on the energy loss upstream to be 7 MeV, as calculated
2266 in Section 5.4. We describe the estimate of the uncertainty on $E_{\text{FF-j}}$ in the rest of
2267 this section.

2268 The energy deposited by the hadron from the TPC front face until the j^{th} slice is
2269 the sum of the measured energy deposited in each previous slabs E_i , i.e.

$$E_{\text{FF-j}} = \sum_{i < j} E_i, \quad (5.12)$$

2270 where E_i is measured in each slab as the product of the stopping power, dE/dX_i ,
2271 and the track pitch, $Pitch_i$, for that point. If we assume conservatively that the
2272 measurements of E_i are not independent from one another, the uncertainty on $E_{\text{FF-j}}$
2273 becomes

$$\delta E_{\text{FF-j}} = (j - 1)\delta E_i, \quad (5.13)$$

2274 where δE_i is the uncertainty on the energy loss in one slab of argon.

2275 The left side of Figure 5.21 shows the distribution of the energy deposited in each
2276 slab of argon, for the 60A negative pion dataset in black and for the pion only MC
2277 in blue. The analogous plot for the -100A negative pion data set is show on the right
2278 side of Figure 5.21. The distributions are fitted with a landau displayed in red for
2279 data and in teal for MC. The uncertainty on E_i is given by the width of the Landau
2280 fit to the data. A small systematic uncertainty is given by a 1.0% difference between
2281 the most probable value of the landau fits in data and MC.

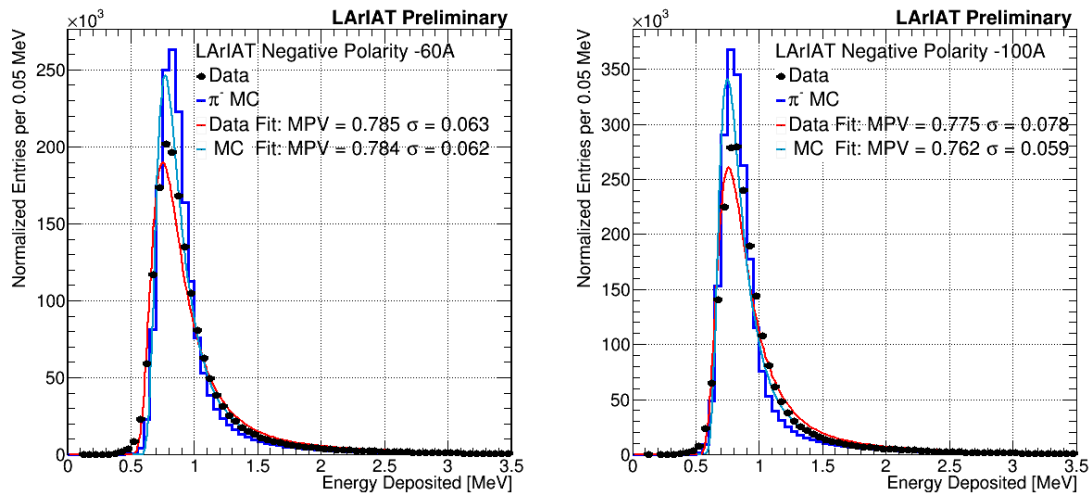


Figure 5.21: Energy deposited E_i in a single slab of argon for the pion -60A runs (left) and -100A runs (right). The data is shown in black, the MC in blue. The distributions are fitted with a landau displayed in red for data and in teal for MC.

2282 **Chapter 6**

2283 **Negative Pion Cross Section**

2284 **Measurement**

2285 “*Y ella es flama que se eleva, Y es un pájaro a volar.*
2286 *En la noche que se incendia, estrella de oscuridad*
2287 *que busca entre la tiniebla, la dulce hoguera del beso.*”
2288 – Lila Downs, Benediction And Dream, 2002 –

2289 In this chapter, we show the result of the thin slice method to measure the (π^- -
2290 Ar) total hadronic cross section. In Section 6.1, we start by measuring the raw
2291 cross section, i.e. the cross section obtained exclusively using data reconstruction,
2292 without any additional corrections. In Section 6.2, we apply a statistical subtraction
2293 of the background contributions based on simulation and a correction for detection
2294 inefficiency. The final results are presented in Section 6.3.

2295 **6.1 Raw Cross Section**

2296 We measure the raw (π^- -Ar) total hadronic cross section as a function of the kinetic
2297 energy in the two chosen data sets, the -60A and -100A negative runs. As we will

clarify in Section 6.2, the corrections to the raw cross section depend on the beam conditions and need to be calculated independently for the two datasets. Thus, we present here the measurement of the raw cross section on the two datasets separately.

As stated in section 4.3.2, the raw cross section is given by the equation

$$\sigma_{TOT}(E_i) = \frac{1}{n\delta X} \frac{N_{Int}^{TOT}(E_i)}{N_{Inc}^{TOT}(E_i)}, \quad (6.1)$$

where N_{Int}^{TOT} is the measured number of particles interacting at kinetic energy E_i , N_{Inc}^{TOT} is the measured number of particles incident on an argon slice at kinetic energy E_i , n is the density of the target centers and δX is the thickness of the argon slice. The density of the target centers and the slab thickness are $n = 0.021 \cdot 10^{24} \text{ cm}^{-3}$ and $\delta X = 0.47 \text{ cm}$, respectively.

Figure 6.1 shows the distribution of N_{Int}^{TOT} as a function of the kinetic energy for the 60A dataset on the left and for the 100A dataset on the right. The data central points are represented by black dots, the statistical uncertainty is shown in black, while the systematic uncertainty is shown in red. Data is displayed over the N_{Int}^{TOT} distribution obtained with a MC mixed sample of pions, muon and electrons (additional details on the composition will be provided in Section ??). The contribution from the simulated pions is shown in blue, the one from secondaries in red, the one from muons in yellow and the ones from electrons in gray. The simulated pion's and backgrounds' contributions are stacked; the sum of the integrals from each particle species is normalized to the integral of the data.

Figure 6.2 shows the distribution of N_{Inc}^{TOT} for the 60A dataset on the left and for the 100A dataset on the right. Data is displayed over the MC. The same color scheme and normalization procedure is used for both the interacting and incident histograms.

Figure 6.3 shows the raw cross section for the 60A dataset on the left and for the 100A dataset on the right, statistical uncertainty in black and systematic uncertainty

2322 in red. The raw data cross section is overlaid to the reconstructed cross section for
 2323 the MC mixed sample, displayed in azure. Since the background contributions and
 2324 the detector effects for the 60A and 100A sample are different, it is premature to
 2325 compare the raw cross sections obtained from the two samples at this point.

2326 We describe the calculation of the statistical uncertainty for the interacting, in-
 2327 cident and cross section distributions in Section 6.1.1; we describe the procedure to
 2328 calculate the corresponding systematics uncertainty on Section 6.1.2.

2329 6.1.1 Statistical Uncertainty

2330 The statistical uncertainty for a given kinetic energy bin of the cross section is cal-
 2331 culated by error propagation from the statistical uncertainty on $N_{\text{Inc}}^{\text{TOT}}$ and $N_{\text{Int}}^{\text{TOT}}$
 2332 correspondent bin. Since the number of incident particles in each energy bin is given
 2333 by a simple counting, we assume that $N_{\text{Inc}}^{\text{TOT}}$ is distributed as a poissonian with mean
 2334 and variance equal to $N_{\text{Inc}}^{\text{TOT}}$ in each bin. On the other hand, $N_{\text{Int}}^{\text{TOT}}$ follows a bino-
 2335 mial distribution: a particle in a given energy bin might or might not interact. The
 2336 variance for the binomial is given by

$$\text{Var}[N_{\text{Int}}^{\text{TOT}}] = \mathcal{N}P_{\text{Interacting}}(1 - P_{\text{Interacting}}). \quad (6.2)$$

2337 Since the interaction probability $P_{\text{Interacting}}$ is $\frac{N_{\text{Int}}^{\text{TOT}}}{N_{\text{Inc}}^{\text{TOT}}}$ and the number of tries \mathcal{N} is
 2338 $N_{\text{Inc}}^{\text{TOT}}$, equation 6.2 translates into

$$\text{Var}[N_{\text{Int}}^{\text{TOT}}] = N_{\text{Inc}}^{\text{TOT}} \frac{N_{\text{Int}}^{\text{TOT}}}{N_{\text{Inc}}^{\text{TOT}}} \left(1 - \frac{N_{\text{Int}}^{\text{TOT}}}{N_{\text{Inc}}^{\text{TOT}}}\right) = N_{\text{Int}}^{\text{TOT}} \left(1 - \frac{N_{\text{Int}}^{\text{TOT}}}{N_{\text{Inc}}^{\text{TOT}}}\right). \quad (6.3)$$

2339 $N_{\text{Inc}}^{\text{TOT}}$ and $N_{\text{Int}}^{\text{TOT}}$ are not independent. The statistical uncertainty on the cross
 2340 section is thus calculated as

$$\delta\sigma_{\text{TOT}}(E) = \sigma_{\text{TOT}}(E) \left(\frac{\delta N_{\text{Int}}^{\text{TOT}}}{N_{\text{Int}}^{\text{TOT}}} + \frac{\delta N_{\text{Inc}}^{\text{TOT}}}{N_{\text{Inc}}^{\text{TOT}}} \right) \quad (6.4)$$

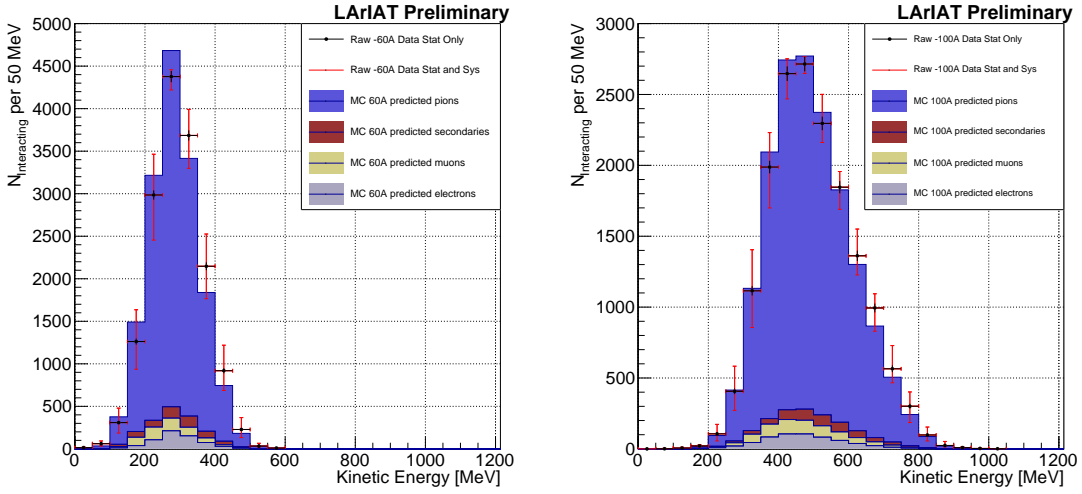


Figure 6.1: Raw number of interacting pion candidates as a function of the reconstructed kinetic energy for the 60A runs (left) and for the 100A runs (right). The statistical uncertainties are shown in black, the systematic uncertainties in red.

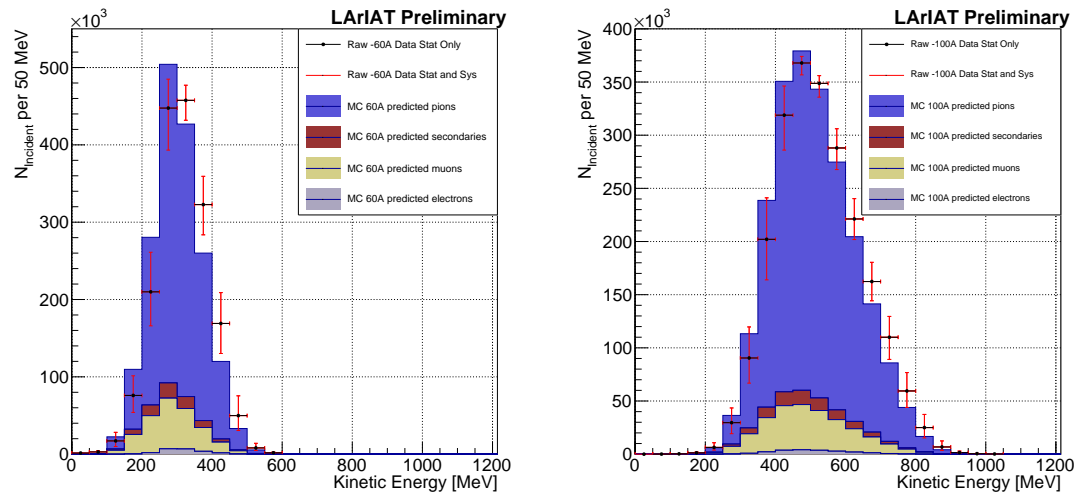


Figure 6.2: Raw number of incident pion candidates as a function of the reconstructed kinetic energy for the 60A runs (left) and for the 100A runs (right). The statistical uncertainty is shown in black, the systematic uncertainties in red.

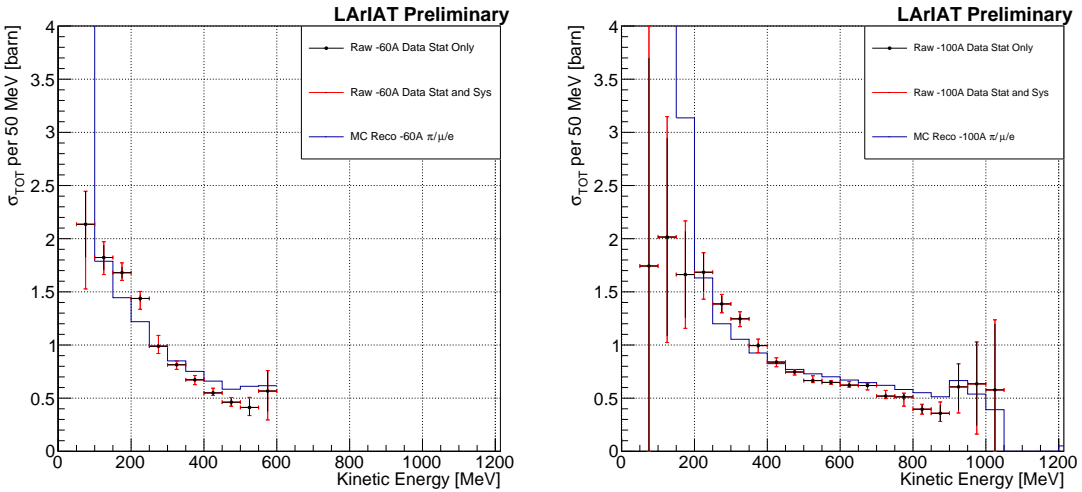


Figure 6.3: Raw (π^- -Ar) total hadronic cross section for the 60A runs (left) and for the 100A runs (right). The statistical uncertainty is shown in black, the systematic uncertainties in red. The raw cross section obtained with a MC mixed sample of pions, muon and electrons in the percentage predicted by G4Beamline is shown in azure.

2341 where:

$$\delta N_{\text{Inc}}^{\text{TOT}} = \sqrt{N_{\text{Inc}}^{\text{TOT}}} \quad (6.5)$$

$$\delta N_{\text{Int}}^{\text{TOT}} = \sqrt{N_{\text{Int}}^{\text{TOT}} \left(1 - \frac{N_{\text{Int}}^{\text{TOT}}}{N_{\text{Inc}}^{\text{TOT}}}\right)}. \quad (6.6)$$

2342 6.1.2 Treatment of Systematics

2343 The only systematic effect considered in the measurement of the raw cross section
 2344 results from the propagation of the uncertainty associate with the measurement of
 2345 the kinetic energy at each argon slab. As shown in Section 5.6.2, the uncertainty on
 2346 the kinetic energy of a pion candidate at the j^{th} slab of argon is given by

$$\delta KE_j = \sqrt{\delta p_{\text{Beam}}^2 + \delta E_{\text{Loss}}^2 + \delta E_{\text{dep FF-j}}^2} \quad (6.7)$$

$$= \sqrt{(2\% p_{\text{Beam}})^2 + (\sim 6 \text{ [MeV]})^2 + (j-1)^2(\sim 0.08 \text{ [MeV]})^2}. \quad (6.8)$$

2347 We propagate this uncertainty by varying the energy measurement KE_j at each
 2348 argon slab. We measure $N_{\text{Inc}}^{\text{TOT}}$, $N_{\text{Int}}^{\text{TOT}}$ and the cross section in three cases: first
 2349 assigning the measured KE_j at each kinetic energy sampling, then assigning $KE_j +$
 2350 δKE_j , and finally assigning $KE_j - \delta KE_j$. The difference between the values obtained
 2351 using the KE_j sampling and the maximum and minimum values in each kinetic energy
 2352 bin determines the systematic uncertainty.

2353 **6.2 Corrections to the Raw Cross Section**

2354 As described in section 4.3.3, we need to apply a background correction and an
 2355 efficiency correction in order to derive the true pion cross section from the raw cross
 2356 section. The true cross section is given in equation 4.9,

$$\sigma_{\text{TOT}}^{\pi^-}(E_i) = \frac{1}{n\delta X} \frac{\epsilon^{\text{Inc}}(E_i)}{\epsilon^{\text{Int}}(E_i)} \frac{C_{\text{Int}}^{\pi MC}(E_i)}{C_{\text{Inc}}^{\pi MC}(E_i)} \frac{N_{\text{Int}}^{\text{TOT}}(E_i)}{N_{\text{Inc}}^{\text{TOT}}(E_i)}. \quad (4.9)$$

2357 Section 6.2.1 describes the evaluation of pion content in the interacting and inci-
 2358 dent histograms, ($C_{\text{Int}}^{\pi MC}(E_i)$ and $C_{\text{Inc}}^{\pi MC}(E_i)$) and the propagation to the cross section
 2359 measurement of the relative systematic uncertainties.

2360 Section 6.2.2 describes the procedure employed to obtain the efficiency corrections
 2361 $\epsilon^{\text{Int}}(E_i)$ and $\epsilon^{\text{Inc}}(E_i)$ and the propagation to the cross section measurement of the
 2362 relative uncertainties.

2363 **6.2.1 Background subtraction**

2364 We use the procedure described in 5.3.2 to evaluate the relative pion content in
 2365 the interacting histogram $C_{\text{Int}}^{\pi MC}(E_i)$ and the relative pion content in the incident
 2366 $C_{\text{Inc}}^{\pi MC}(E_i)$. We start by evaluating the relative pion content assuming the beamline
 2367 composition simulated by G4Beamline, whose pion, muon and electron percentages
 2368 per beam condition are reported again in the first line of Table 6.1. The left side of

2369 Figure 6.4 shows the MC estimated relative pion content for the interacting histogram
2370 as function of kinetic energy for the 60A runs (top) and 100A runs (bottom). The
2371 right side of the same figure shows the MC estimated relative pion content for the
2372 incident histogram as function of kinetic energy for the 60A runs (top) and 100A
2373 runs (bottom). In Figure 6.4 the central curves displayed in light blue are obtained
2374 using the beamline composition as predicted by G4Beamline: these are the correction
2375 curves for the relative pion content applied to data.

2376 So, the question now becomes: how well do we know the beamline composition?
2377 In absence of additional data constraints, we take a 100% systematic uncertainty on
2378 the electron content, reported in lines 3 and 4 of Table 6.1. The effect of doubling or
2379 halving the electron percentage in the beam on the pion relative content is displayed
2380 in red in Figure 6.4. We reserve a slightly different treatment for the muon content.
2381 Since G4Beamline tracks only particles which cross all the wire chambers, pion events
2382 that decay in flight from WC1 to WC4 are not recorded by G4Beamline. Pion decays
2383 in the beamline could be trigger the beamline detectors in data, if the produced muon
2384 proceeds in the beamline. Thus, we take the G4Beamline prediction for muons as a
2385 lower bound in the composition: the effect of doubling the muon content (line 2 in
2386 Table 6.1) is shown in blue on Figure 6.4. A future study of data from additional
2387 beamline detectors such as the Aerogel Chernkov detectors [42] or the muon range
2388 stack (see Section 3.2.4) has the potential of a narrowing the systematics uncertainty
2389 coming from the beamline composition.

2390 We propagate the uncertainty on the beamline composition as a systematic un-
2391 certainty to the cross section by varying the beam composition for all the cases listed
2392 in Table 6.1 and evaluating variation of obtained data cross sections in each bin. This
2393 systematic uncertainty is summed in quadrature with the statistical uncertainty and
2394 the systematic uncertainty related to the kinetic energy measurement.

	Magnet Current -60A			Magnet Current -100 A		
	MC π^-	MC μ^-	MC e^-	MC π^-	MC μ^-	MC e^-
Expected Composition	68.8 %	4.6 %	26.6 %	87.4 %	3.7 %	8.9 %
Composition 2x Muons	64.2 %	9.2 %	26.6 %	83.7 %	7.4 %	8.9 %
Composition 2x Electrons	42.2 %	4.6 %	53.2 %	78.5 %	3.7 %	17.8 %
Composition 0.5x Electrons	82.1 %	4.6 %	13.3 %	91.9 %	3.7 %	4.4 %

Table 6.1: Beam composition variation for the study of systematics due to beam contamination.

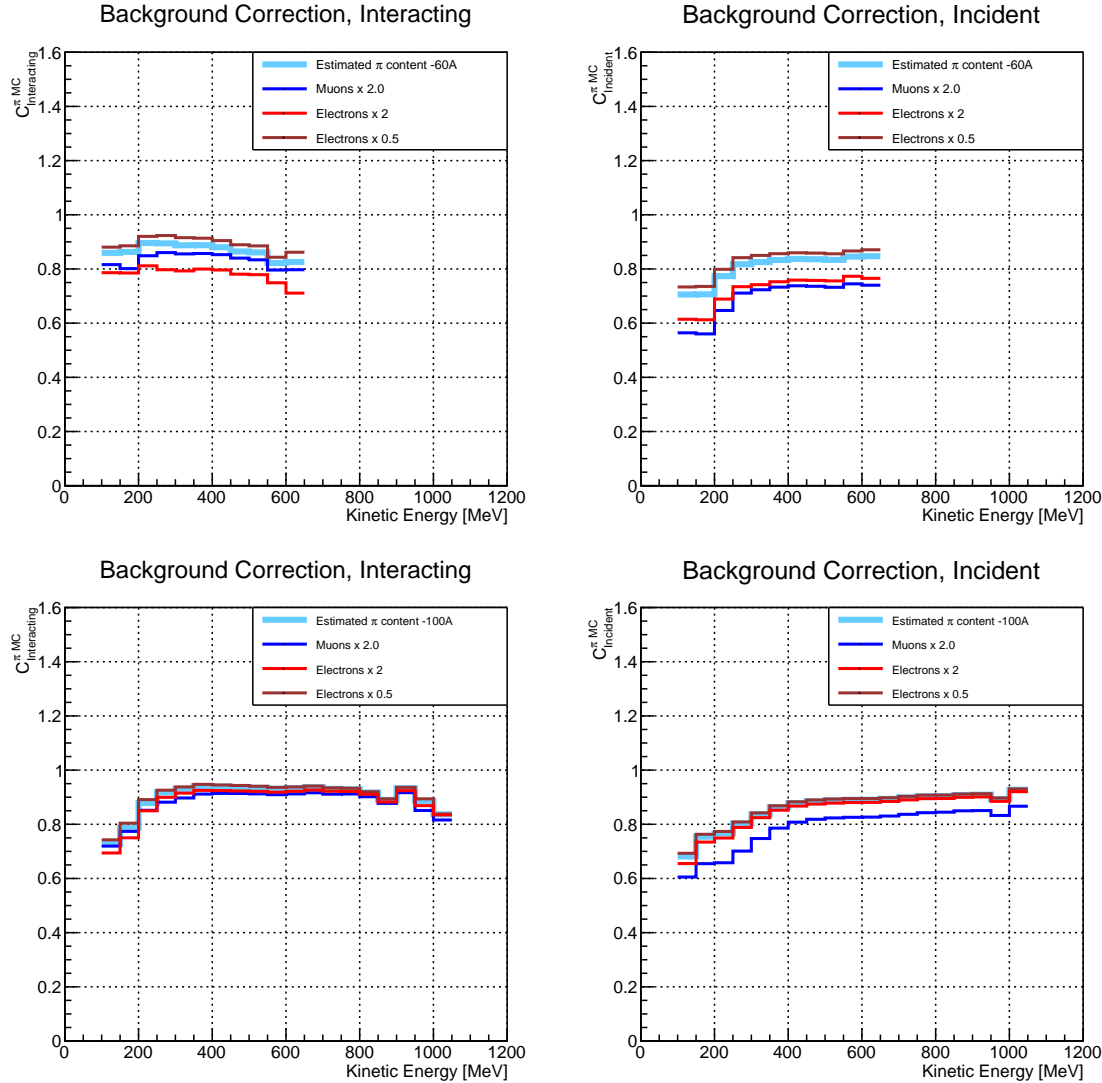


Figure 6.4: *Left:* MC estimated relative pion content for interacting histogram a function of kinetic energy for the 60A runs (top) and 100A runs (bottom), statistics uncertainty in azure and systematic uncertainty in blue. *Right:* MC estimated relative pion content for incident histogram a function of kinetic energy for the 60A runs (top) and 100A (bottom), statistics uncertainty in azure and systematic uncertainty in blue.

2395 6.2.2 Efficiency Correction

2396 The interaction point for a track used in the total hadronic cross section analysis
2397 is defined to be the last point of the WC2TPC matched track which lies inside the
2398 fiducial volume. This definition is independent from the topology of the interaction.
2399 If the TPC track stops within the fiducial volume, its last point will be the interaction
2400 point, no matter what the products of the interaction look like; if the track crosses the
2401 boundaries of the fiducial volume, the track will be considered “through going” and no
2402 interaction point will be found. Given this definition, it is evident that we rely on the
2403 tracking algorithm to discern where the interaction occurred in the TPC and correctly
2404 stop the tracking. The tracking algorithm has an intrinsic angle resolution as shown
2405 in section 5.5.3, which limits its efficiency, especially in the case of elastic scattering
2406 occurring at low angles. Thus, we need to apply an efficiency correction to data in order
2407 to retrieve the true cross section. The efficiency correction is evaluated separately for
2408 the interacting and incident histograms, namely ϵ_i^{int} and ϵ_i^{inc} , and propagated to the
2409 cross section as shown in equation 4.9.

2410 Efficiency Correction: Procedure

2411 We describe here the procedure to calculate the efficiency correction taking the in-
2412 teracting histogram as example and noting that the procedure is identical for the
2413 incident histogram.

2414 We derive the correction on a set of pure pion MC, calculating its value bin by
2415 bin as the ratio between the true bin content and the correspondent reconstructed
2416 bin content. The correction is then applied to the relevant bin in data. In formulae,
2417 the efficiency correction is calculated to be

$$\epsilon^{\text{Int}}(E_i) = \frac{N_{\text{Interacting}}^{\pi \text{ Reco MC}}(E_i)}{N_{\text{Interacting}}^{\pi \text{ True MC}}(E_i)}, \quad (6.9)$$

2418 where $N_{\text{Int}}^{\pi \text{ True MC}}(E_i)$ is the content of the i -th bin in for the true interacting
 2419 histogram, and $N_{\text{Int}}^{\pi \text{ Reco MC}}(E_i)$ is the content of the i -th bin in for the reconstructed
 2420 interacting histogram. The correction is applied to data as follows

$$N_{\text{Int}}^{\pi \text{ True Data}}(E_i) = \frac{N_{\text{Int}}^{\pi \text{ Reco Data}}(E_i)}{\epsilon^{\text{Int}}(E_i)} = N_{\text{Int}}^{\pi \text{ Reco Data}}(E_i) \frac{N_{\text{Int}}^{\pi \text{ True MC}}(E_i)}{N_{\text{Int}}^{\pi \text{ Reco MC}}(E_i)}. \quad (6.10)$$

2421 where $N_{\text{Int}}^{\pi \text{ Reco Data}}(E_i)$ is the background subtracted bin content of the i -th bin in
 2422 for the reconstructed interacting histogram for data, i.e.

$$N_{\text{Int}}^{\pi \text{ Reco Data}}(E_i) = N_{\text{Int}}^{\text{TOT Data}}(E_i) - B_{\text{Int}}^{\text{Data}}(E_i) = C_{\text{Int}}^{\pi \text{ MC}}(E_i) N_{\text{Int}}^{\text{TOT Data}}(E_i). \quad (6.11)$$

2423 In section 5.5.3, we estimated the angular resolution for data and MC to be
 2424 $\bar{\alpha}_{\text{Data}} = (5.0 \pm 4.5)$ deg and $\bar{\alpha}_{\text{MC}} = (4.5 \pm 3.9)$ deg, respectively. Most interaction
 2425 angles smaller than the angular resolution will thus be indistinguishable for the re-
 2426 construction. Thus, we claim we are able to measure the cross section for interaction
 2427 angles greater than 5.0 deg. Geant4 simulates interactions at all angles, as shown in
 2428 figure 6.7. In order to calculate the efficiency correction, we select events which have
 2429 an interaction angle greater than a given α_{res} to construct the true interacting and
 2430 incident histograms (the denominator of the efficiency correction). The systematics
 2431 on the efficiency correction is estimated by varying the value of α_{res} between 0 deg
 2432 and 4.5 deg and propagating the uncertainty on the cross section.

2433 Figure 6.5 shows $\epsilon^{\text{Int}}(E_i)$ in the left side and $\epsilon^{\text{Inc}}(E_i)$ on the right as a function of
 2434 the kinetic energy for the 60A runs and their systematic uncertainty. Similarly, figure
 2435 6.6 shows $\epsilon^{\text{Int}}(E_i)$ in the left side and $\epsilon^{\text{Inc}}(E_i)$ on the right as a function of the kinetic
 2436 energy for the 100A runs and their systematic uncertainty.

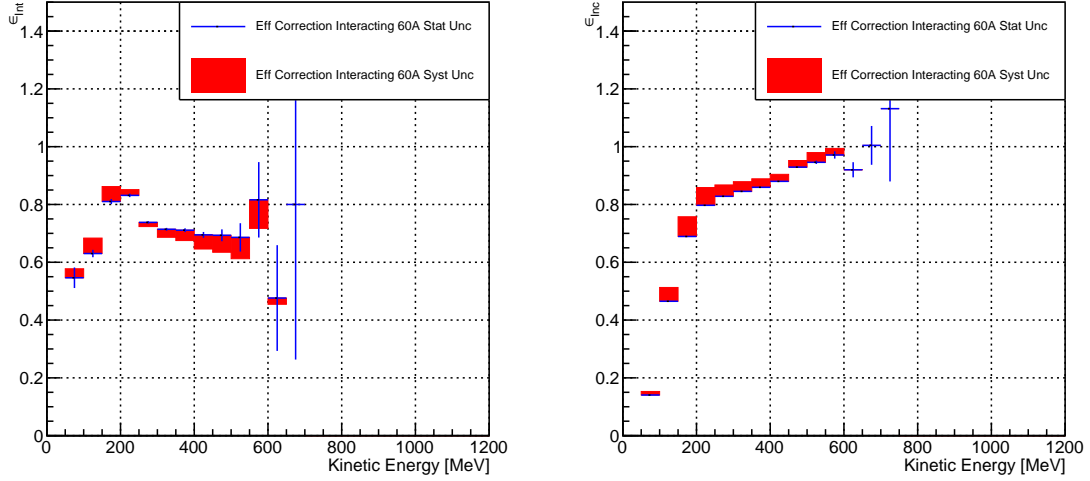


Figure 6.5: *Left:* Efficiency correction on the 60A interacting histogram, statistical uncertainty in blue, systematic uncertainty in red. *Right:* Efficiency correction on the 60A incident histogram, statistical uncertainty in blue, systematic uncertainty in red.

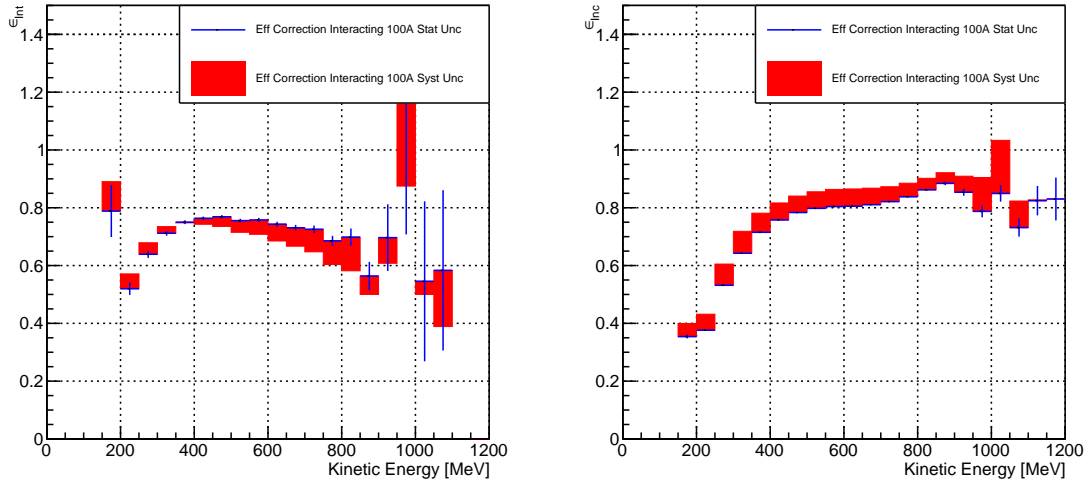


Figure 6.6: *Left:* Efficiency correction on the 100A interacting histogram, statistical uncertainty in blue, systematic uncertainty in red. *Right:* Efficiency correction on the 100A incident histogram, statistical uncertainty in blue, systematic uncertainty in red.

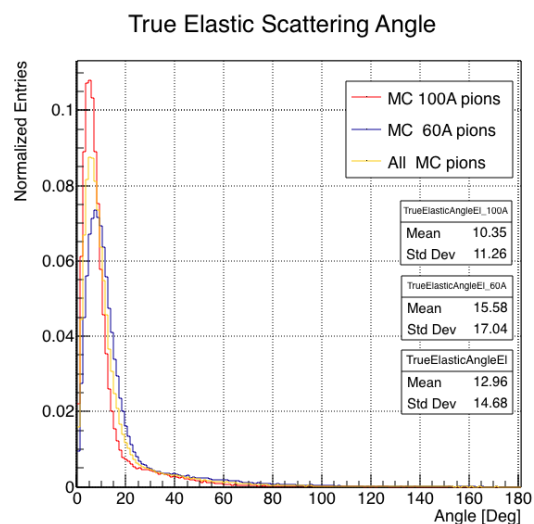


Figure 6.7: Distribution of the true scattering angle for a pion elastic scattering off the argon nucleus as simulated by Geant4.

2437 **6.3 Results**

2438 Figure 6.8 show the measurement of the (π^- -Ar) total hadronic cross section for
2439 scattering angles greater than 5° , as the result of the background subtraction and
2440 efficiency correction to the raw cross section. The top left plot is the measurement
2441 obtained on the 60A data, statistical uncertainty in black and systematic uncertainty
2442 in red. The top right plot is the measurement obtained on the 100A data, statistical
2443 uncertainty in black and systematic uncertainty in blue. The bottom plot shows the
2444 two measurements overlaid. In all three plot, the Geant4 prediction for the total
2445 hadronic cross section for angle scattering greater than 5° is displayed in green.

2446 The systematic uncertainty on the cross section is the sum in quadrature of the
2447 statistical uncertainty, the systematic uncertainty related to the kinetic energy mea-
2448 surement, the systematic uncertainty related to the beam composition and the sys-
2449 tematic uncertainty related to the efficiency correction.

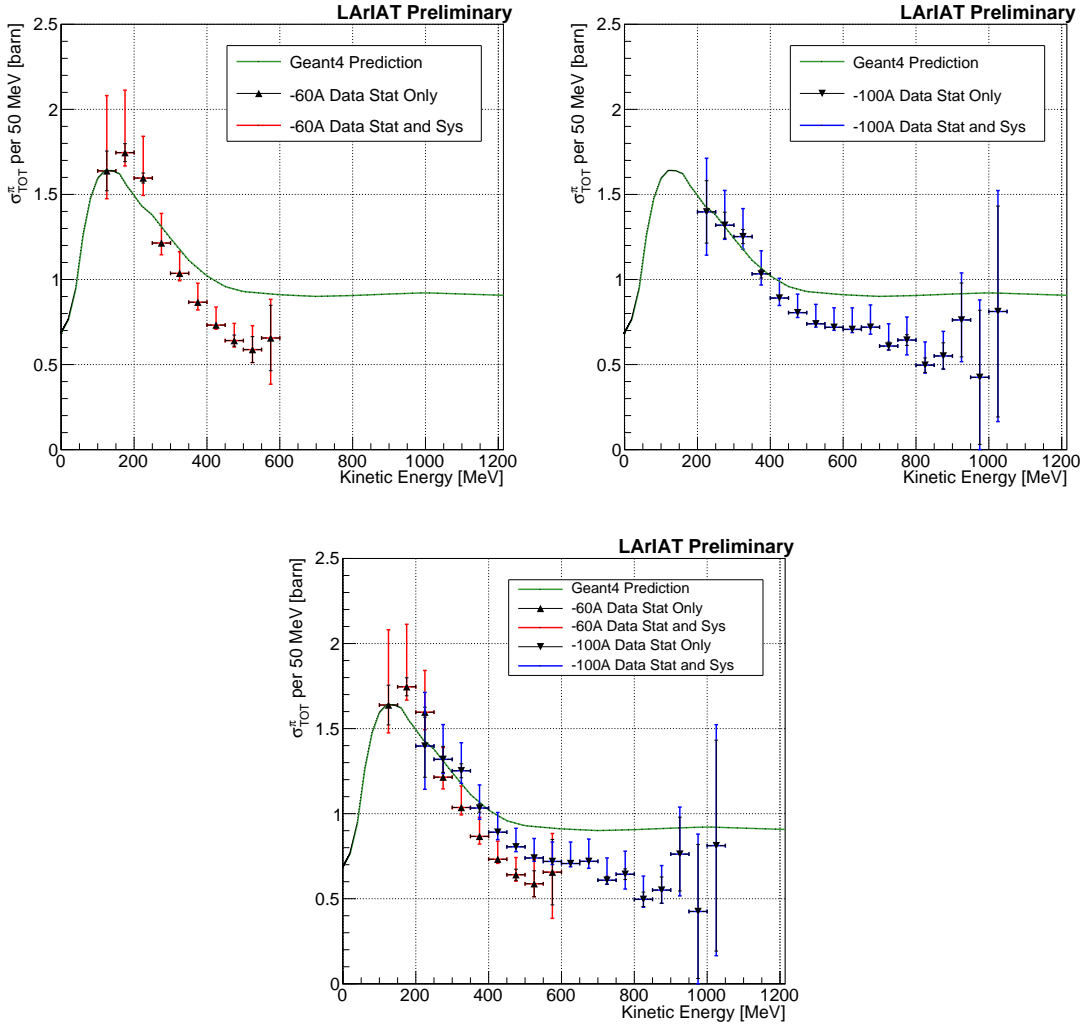


Figure 6.8: *Top Left:* (π^- -Ar) total hadronic cross section for scattering angles greater than 5° measured in the 60A sample, statistical uncertainty in black and systematic uncertainty in red. The Geant4 prediction for the total hadronic cross section for angle scattering greater than 5° is displayed in green.

Top Right: (π^- -Ar) total hadronic cross section for scattering angles greater than 5° measured in the 100A sample, statistical uncertainty in black and systematic uncertainty in blue. The Geant4 prediction for the total hadronic cross section for angle scattering greater than 5° is displayed in green.

Bottom: (π^- -Ar) total hadronic cross section measurements in the 60A and 100A samples overlaid with the Geant4 prediction (green).

2450 Chapter 7

2451 Positive Kaon Cross Section
2452 Measurement

2453 7.1 Raw Cross Section

2454 **Appendix A**

2455 **Measurement of LArIAT Electric**
2456 **Field**

2457 The electric field of a LArTPC in the drift volume is a fundamental quantity for
2458 the proper functionality of this technology, as it affects almost every reconstructed
2459 quantity such as the position of hits or their collected charge. Given its importance,
2460 we calculate the electric field for LArIAT with a single line diagram from our HV
2461 circuit and we cross check the obtained value with a measurement relying only on
2462 TPC data.

2463 Before getting into the details of the measurement procedures, it is important to
2464 explicit the relationship between some quantities in play. The electric field and the
2465 drift velocity (v_{drift}) are related as follows

$$v_{drift} = \mu(E_{field}, T)E_{field}, \quad (\text{A.1})$$

2466 where μ is the electron mobility, which depends on the electric field and on the
2467 temperature (T). The empirical formula for this dependency is described in [?] and
2468 shown in Figure A.1 for several argon temperatures.

2469 The relationship between the drift time (t_{drift}) and the drift velocity is trivially

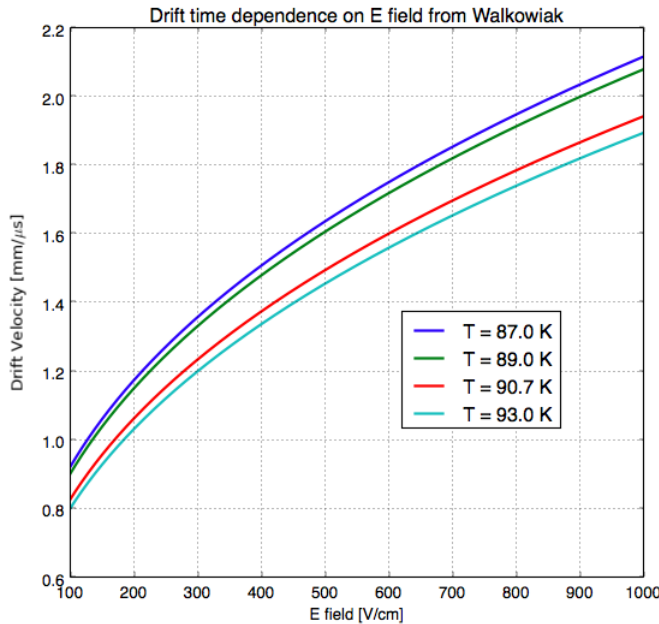


Figure A.1: Drift velocity dependence on electric field for several temperatures. The slope of the line at any one point represents the electron mobility for that given temperature and electric field.

Table A.1: Electric field and drift velocities in LArIAT smaller drift volumes

	Shield-Induction	Induction-Collection
E_{field}	700.63 V/cm	892.5 V/cm
v_{drift}	1.73 mm/μs	1.90 mm/μs
t_{drift}	2.31 μs	2.11 μs

2470 given by

$$t_{drift} = \Delta x / v_{drift}, \quad (\text{A.2})$$

2471 where Δx is the distance between the edges of the drift region. Table A.1 reports the
2472 values of the electric field, drift velocity, and drift times for the smaller drift volumes.

2473 With these basic parameters established, we can now move on to calculating the
2474 electric field in the main drift region (between the cathode and the shield plane).

2475 Single line diagram method

2476 The electric field strength in the LArIAT main drift volume can be determined know-
 2477 ing the voltage applied to the cathode, the voltage applied at the shield plane, and the
 2478 distance between them. We assume the distance between the cathode and the shield
 2479 plane to be 470 mm and any length contraction due to the liquid argon is negligibly
 2480 small (~ 2 mm).

2481 The voltage applied to the cathode can be calculated using Ohm's law and the
 2482 single line diagram shown in Figure A.2. A set of two of filter pots for emergency
 2483 power dissipation are positioned between the Glassman power supply and the cathode,
 2484 one at each end of the feeder cable, each with an internal resistance of $40 \text{ M}\Omega$.

2485 Given the TPC resistor chain, the total TPC impedance is $6 \text{ G}\Omega$. Since the total
 2486 resistance on the circuit is driven by the TPC impedance, we expect the resulting
 2487 current to be

$$I = V_{PS}/R_{tot} = -23.5 \text{ kV}/6 \text{ G}\Omega \sim 4 \mu\text{A}, \quad (\text{A.3})$$

2488 which we measure with the Glassman power supply, shown in Figure A.3.

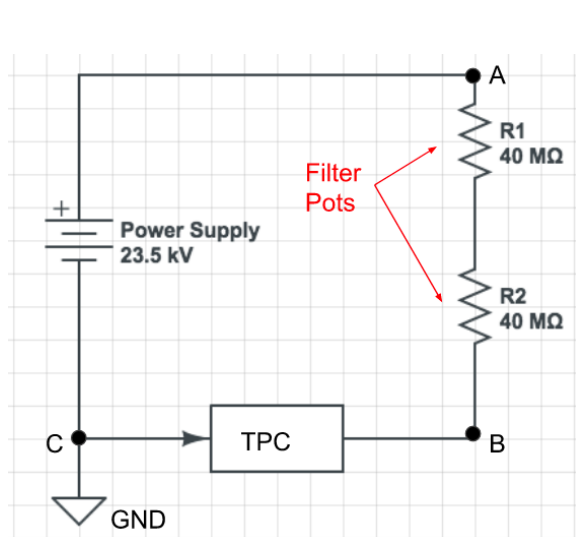


Figure A.2: LArIAT HV simple schematics.

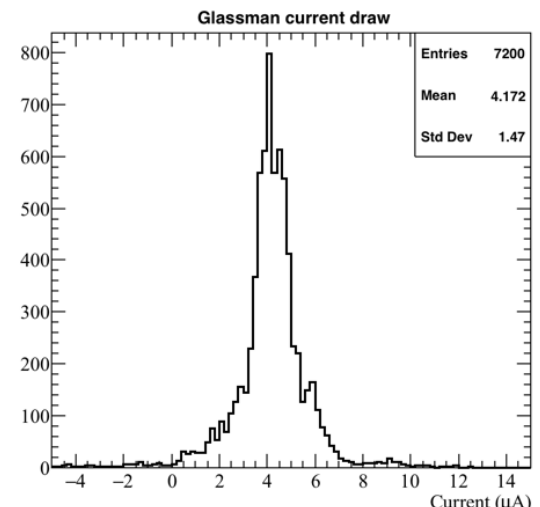


Figure A.3: Current reading from the Glassman between May 25th and May 30th, 2016 (typical Run-II conditions).

2489 Using this current, the voltage at the cathode is calculated as

$$V_{BC} = V_{PS} - (I \times R_{eq}) = -23.5 \text{ kV} + (0.00417 \text{ mA} \times 80 \text{ M}\Omega) = -23.17 \text{ kV}, \quad (\text{A.4})$$

2490 where I is the current and R_{eq} is the equivalent resistor representing the two filter
2491 pots. The electric field is then calculated to be

$$E_{\text{field}} = \frac{V_{BC} - V_{\text{shield}}}{\Delta x} = 486.54 \text{ V/cm}. \quad (\text{A.5})$$

2492 **E field using cathode-anode piercing tracks**

2493 We devise an independent method to measure the drift time (and consequently drift
2494 velocity and electric field) using TPC cathode to anode piercing tracks. We use this
2495 method as a cross check to the single line method. The basic idea is simple:

- 2496 0. Select cosmic ray events with only 1 reconstructed track
- 2497 1. Reduce the events to the one containing tracks that cross both anode and cath-
2498 ode
- 2499 2. Identify the first and last hit of the track
- 2500 3. Measure the time difference between these two hits (Δt).

2501 This method works under the assumptions that the time it takes for a cosmic particle
2502 to cross the chamber ($\sim \text{ns}$) is small compared to the charge drift time ($\sim \text{hundreds}$
2503 of μs).

2504 We choose cosmic events to allow for a high number of anode to cathode piercing
2505 tracks (ACP tracks), rejecting beam events where the particles travel almost perpen-
2506 dicularly to drift direction. We select events with only one reconstructed track to
2507 maximize the chance of selecting a single crossing muon (no-michel electron). We
2508 utilize ACP tracks because their hits span the full drift length of the TPC, see figure

2509 A.4, allowing us to define where the first and last hit of the tracks are located in space
2510 regardless of our assumption of the electric field.

2511 One of the main features of this method is that it doesn't rely on the measurement
2512 of the trigger time. Since Δt is the time difference between the first and last hit of a
2513 track and we assume the charge started drifting at the same time for both hits, the
2514 measurement of the absolute beginning of drift time t_0 is unnecessary. We boost the
2515 presence of ACP tracks in the cosmic sample by imposing the following requirements
2516 on tracks:

- 2517 • vertical position (Y) of first and last hits within ± 18 cm from TPC center
2518 (avoid Top-Bottom tracks)
- 2519 • horizontal position (Z) of first and last hits within 2 and 86 cm from TPC front
2520 face (avoid through going tracks)
- 2521 • track length greater than 48 cm (more likely to be crossing)
- 2522 • angle from the drift direction (phi in figure A.5) smaller than 50 deg (more
2523 reliable tracking)
- 2524 • angle from the beam direction (theta in figure A.5) greater than 50 deg (more
2525 reliable tracking)

2526 Tracks passing all these selection requirements are used for the Δt calculation.

2527 For each track passing our selection, we loop through the associated hits to retrieve
2528 the timing information. The analysis is performed separately on hits on the collection
2529 plane and induction plane, but lead to consistent results. As an example of the time
2530 difference, figures A.6 and A.7 represent the difference in time between the last and
2531 first hit of the selected tracks for Run-II Positive Polarity sample on the collection
2532 and induction plane respectively. We fit with a Gaussian to the peak of the Δt
2533 distributions to extract the mean drift time and the uncertainty associated with it.

2534 The long tail at low Δt represents contamination of non-ACP tracks in the track
2535 selection. We apply the same procedure to Run-I and Run-II, positive and negative
2536 polarity alike.

2537 To convert Δt recorded for the hits on the induction plane to the drift time we
2538 employ the formula

$$t_{drift} = \Delta t - t_{S-I} \quad (\text{A.6})$$

2539 where t_{drift} is the time the charge takes to drift in the main volume between the
2540 cathode and the shield plane and t_{S-I} is the time it takes for the charge to drift from
2541 the shield plane to the induction plane. In Table A.1 we calculated the drift velocity
2542 in the S-I region, thus we can calculate t_{S-I} as

$$t_{S-I} = \frac{l_{S-I}}{v_{S-I}} = \frac{4mm}{1.73mm/\mu s} \quad (\text{A.7})$$

2543 where l_{S-I} is the distance between the shield and induction plane and v_{S-I} is the drift
2544 velocity in the same region. A completely analogous procedure is followed for the hits
2545 on the collection plane, taking into account the time the charge spent in drifting from
2546 shield to induction as well as between the induction and collection plane. The value
2547 for Δt_{drift} , the calculated drift velocity (v_{drift}), and corresponding drift electric field
2548 for the various run periods is given in Table A.2 and are consistent with the electric
2549 field value calculated with the single line diagram method.

Delta t_{drift} , drift v and E field with ACP tracks

Data Period	Δt_{Drift} [μs]	Drift velocity [mm/ μs]	E field [V/cm]
RunI Positive Polarity Induction	311.1 ± 2.4	1.51 ± 0.01	486.6 ± 21
RunI Positive Polarity Collection	310.9 ± 2.6	1.51 ± 0.01	487.2 ± 21
RunII Positive Polarity Induction	315.7 ± 2.8	1.49 ± 0.01	467.9 ± 21
RunII Positive Polarity Collection	315.7 ± 2.7	1.49 ± 0.01	467.9 ± 21
RunII Negative Polarity Induction	315.9 ± 2.6	1.49 ± 0.01	467.1 ± 21
RunII Negative Polarity Collection	315.1 ± 2.8	1.49 ± 0.01	470.3 ± 21
Average Values	314.1	1.50 ± 0.01	474.3 ± 21

Table A.2: Δt for the different data samples used for the Anode-Cathode Piercing tracks study.

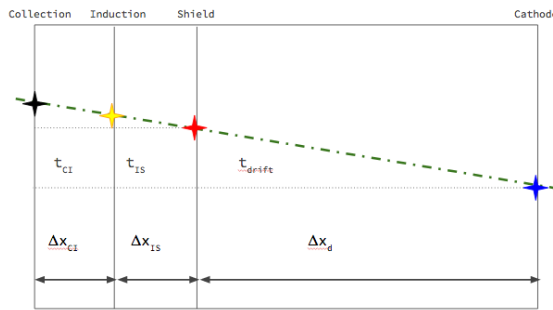


Figure A.4: Pictorial representation of the YX view of the TPC. The distance within the anode planes and between the shield plane and the cathode is purposely out of proportion to illustrate the time difference between hits on collection and induction. An ACP track is shown as an example.

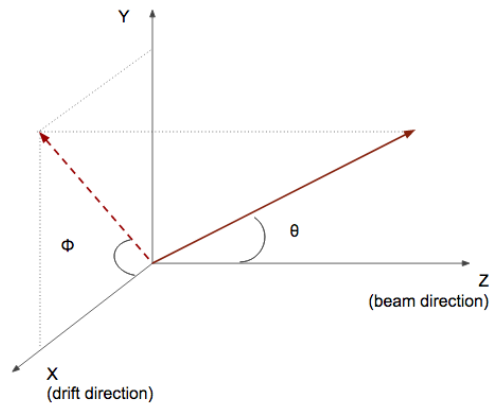


Figure A.5: Angle definition in the context of LArIAT coordinate system.

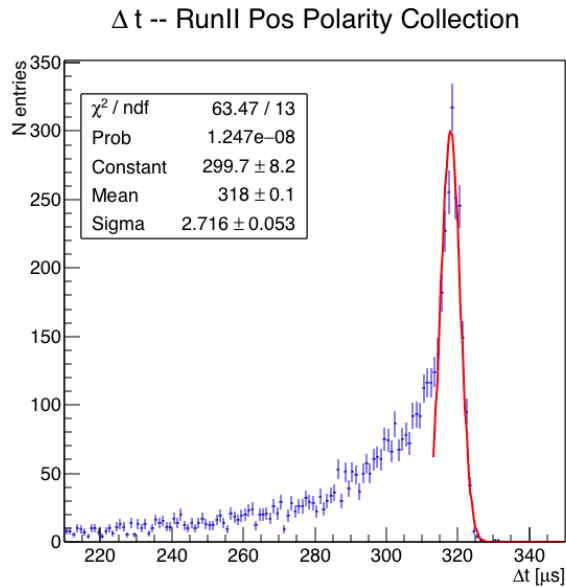


Figure A.6: Collection plane Δt fit for Run II positive polarity ACP data selected tracks.

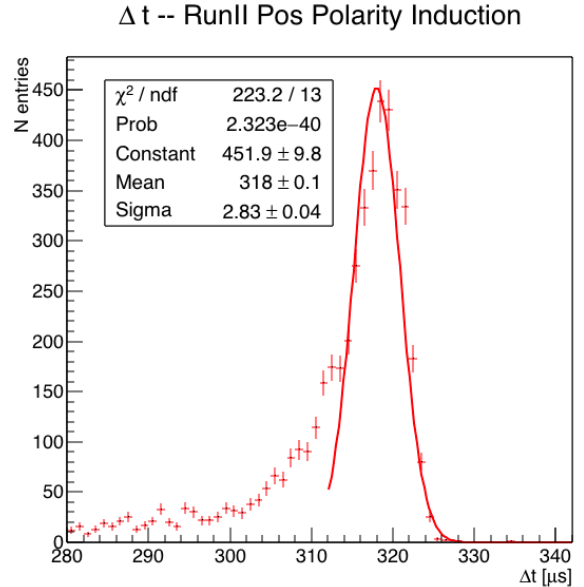


Figure A.7: Induction plane Δt fit for Run II positive polarity ACP data selected tracks.

2550 **Bibliography**

- 2551 [1] PDG Tables for Liquid Argon. . Technical report.
- 2552 [2] Precision electroweak measurements on the Z resonance. *Physics Reports*,
2553 427(5):257 – 454, 2006.
- 2554 [3] K. Abe, J. Amey, C. Andreopoulos, M. Antonova, S. Aoki, A. Ariga, D. Au-
2555 tiero, S. Ban, M. Barbi, G. J. Barker, G. Barr, C. Barry, P. Bartet-Friburg,
2556 M. Batkiewicz, V. Berardi, S. Berkman, S. Bhadra, S. Bienstock, A. Blondel,
2557 S. Bolognesi, S. Bordoni, S. B. Boyd, D. Brailsford, A. Bravar, C. Bronner,
2558 M. Buizza Avanzini, R. G. Calland, T. Campbell, S. Cao, S. L. Cartwright,
2559 M. G. Catanesi, A. Cervera, C. Checchia, D. Cherdack, N. Chikuma,
2560 G. Christodoulou, A. Clifton, J. Coleman, G. Collazuol, D. Coplowe, A. Cudd,
2561 A. Dabrowska, G. De Rosa, T. Dealtry, P. F. Denner, S. R. Dennis, C. Densham,
2562 D. Dewhurst, F. Di Lodovico, S. Di Luise, S. Dolan, O. Drapier, K. E. Duffy,
2563 J. Dumarchez, M. Dziewiecki, S. Emery-Schrenk, A. Ereditato, T. Feusels,
2564 A. J. Finch, G. A. Fiorentini, M. Friend, Y. Fujii, D. Fukuda, Y. Fukuda,
2565 V. Galymov, A. Garcia, C. Giganti, F. Gizzarelli, T. Golan, M. Gonin, D. R.
2566 Hadley, L. Haegel, M. D. Haigh, D. Hansen, J. Harada, M. Hartz, T. Hasegawa,
2567 N. C. Hastings, T. Hayashino, Y. Hayato, R. L. Helmer, A. Hillairet, T. Hiraki,
2568 A. Hiramoto, S. Hirota, M. Hogan, J. Holeczek, F. Hosomi, K. Huang, A. K.
2569 Ichikawa, M. Ikeda, J. Imber, J. Insler, R. A. Intonti, T. Ishida, T. Ishii, E. Iwai,
2570 K. Iwamoto, A. Izmaylov, B. Jamieson, M. Jiang, S. Johnson, P. Jonsson,

2571 C. K. Jung, M. Kabirnezhad, A. C. Kaboth, T. Kajita, H. Kakuno, J. Kameda,
2572 D. Karlen, T. Katori, E. Kearns, M. Khabibullin, A. Khotjantsev, H. Kim,
2573 J. Kim, S. King, J. Kisiel, A. Knight, A. Knox, T. Kobayashi, L. Koch, T. Koga,
2574 A. Konaka, K. Kondo, L. L. Kormos, A. Korzenev, Y. Koshio, K. Kowalik,
2575 W. Kropp, Y. Kudenko, R. Kurjata, T. Kutter, J. Lagoda, I. Lamont, M. Lam-
2576 oureux, E. Larkin, P. Lasorak, M. Laveder, M. Lawe, M. Licciardi, T. Lindner,
2577 Z. J. Liptak, R. P. Litchfield, X. Li, A. Longhin, J. P. Lopez, T. Lou, L. Ludovici,
2578 X. Lu, L. Magaletti, K. Mahn, M. Malek, S. Manly, A. D. Marino, J. F. Martin,
2579 P. Martins, S. Martynenko, T. Maruyama, V. Matveev, K. Mavrokordis, W. Y.
2580 Ma, E. Mazzucato, M. McCarthy, N. McCauley, K. S. McFarland, C. McGrew,
2581 A. Mefodiev, C. Metelko, M. Mezzetto, P. Mijakowski, A. Minamino, O. Mi-
2582 neev, S. Mine, A. Missent, M. Miura, S. Moriyama, Th. A. Mueller, J. Myslik,
2583 T. Nakadaira, M. Nakahata, K. G. Nakamura, K. Nakamura, K. D. Nakamura,
2584 Y. Nakanishi, S. Nakayama, T. Nakaya, K. Nakayoshi, C. Nantais, C. Nielsen,
2585 M. Nirko, K. Nishikawa, Y. Nishimura, P. Novella, J. Nowak, H. M. O'Keeffe,
2586 K. Okumura, T. Okusawa, W. Oryszczak, S. M. Oser, T. Ovsyannikova, R. A.
2587 Owen, Y. Oyama, V. Palladino, J. L. Palomino, V. Paolone, N. D. Patel,
2588 P. Paudyal, M. Pavin, D. Payne, J. D. Perkin, Y. Petrov, L. Pickard, L. Pick-
2589 ering, E. S. Pinzon Guerra, C. Pistillo, B. Popov, M. Posiadala-Zezula, J.-M.
2590 Poutissou, R. Poutissou, P. Przewlocki, B. Quilain, T. Radermacher, E. Radi-
2591 cioni, P. N. Ratoff, M. Ravonel, M. A. Rayner, A. Redij, E. Reinherz-Aronis,
2592 C. Riccio, P. A. Rodrigues, E. Rondio, B. Rossi, S. Roth, A. Rubbia, A. Rychter,
2593 K. Sakashita, F. Sánchez, E. Scantamburlo, K. Scholberg, J. Schwehr, M. Scott,
2594 Y. Seiya, T. Sekiguchi, H. Sekiya, D. Sgalaberna, R. Shah, A. Shaikhiev,
2595 F. Shaker, D. Shaw, M. Shiozawa, T. Shirahige, S. Short, M. Smy, J. T.
2596 Sobczyk, H. Sobel, M. Sorel, L. Southwell, J. Steinmann, T. Stewart, P. Stowell,
2597 Y. Suda, S. Suvorov, A. Suzuki, S. Y. Suzuki, Y. Suzuki, R. Tacik, M. Tada,

- 2598 A. Takeda, Y. Takeuchi, H. K. Tanaka, H. A. Tanaka, D. Terhorst, R. Terri,
2599 T. Thakore, L. F. Thompson, S. Tobayama, W. Toki, T. Tomura, C. Touramani,
2600 T. Tsukamoto, M. Tzanov, Y. Uchida, M. Vagins, Z. Vallari, G. Vasseur,
2601 T. Vladislavljevic, T. Wachala, C. W. Walter, D. Wark, M. O. Wascko, A. We-
2602 ber, R. Wendell, R. J. Wilkes, M. J. Wilking, C. Wilkinson, J. R. Wilson, R. J.
2603 Wilson, C. Wret, Y. Yamada, K. Yamamoto, M. Yamamoto, C. Yanagisawa,
2604 T. Yano, S. Yen, N. Yershov, M. Yokoyama, K. Yoshida, T. Yuan, M. Yu, A. Za-
2605 lewska, J. Zalipska, L. Zambelli, K. Zaremba, M. Ziembicki, E. D. Zimmerman,
2606 M. Zito, and J. Źmuda. Combined analysis of neutrino and antineutrino oscil-
2607 lations at t2k. *Phys. Rev. Lett.*, 118:151801, Apr 2017.
- 2608 [4] K. Abe, Y. Haga, Y. Hayato, M. Ikeda, K. Iyogi, J. Kameda, Y. Kishimoto,
2609 M. Miura, S. Moriyama, M. Nakahata, T. Nakajima, Y. Nakano, S. Nakayama,
2610 A. Orii, H. Sekiya, M. Shiozawa, A. Takeda, H. Tanaka, T. Tomura, R. A. Wen-
2611 dell, R. Akutsu, T. Irvine, T. Kajita, K. Kaneyuki, Y. Nishimura, E. Richard,
2612 K. Okumura, L. Labarga, P. Fernandez, J. Gustafson, C. Kachulis, E. Kearns,
2613 J. L. Raaf, J. L. Stone, L. R. Sulak, S. Berkman, C. M. Nantais, H. A.
2614 Tanaka, S. Tobayama, M. Goldhaber, W. R. Kropp, S. Mine, P. Weatherly,
2615 M. B. Smy, H. W. Sobel, V. Takhistov, K. S. Ganezer, B. L. Hartfiel, J. Hill,
2616 N. Hong, J. Y. Kim, I. T. Lim, R. G. Park, A. Himmel, Z. Li, E. O’Sullivan,
2617 K. Scholberg, C. W. Walter, T. Wongjirad, T. Ishizuka, S. Tasaka, J. S. Jang,
2618 J. G. Learned, S. Matsuno, S. N. Smith, M. Friend, T. Hasegawa, T. Ishida,
2619 T. Ishii, T. Kobayashi, T. Nakadaira, K. Nakamura, Y. Oyama, K. Sakashita,
2620 T. Sekiguchi, T. Tsukamoto, A. T. Suzuki, Y. Takeuchi, T. Yano, S. V. Cao,
2621 T. Hiraki, S. Hirota, K. Huang, T. Kikawa, A. Minamino, T. Nakaya, K. Suzuki,
2622 Y. Fukuda, K. Choi, Y. Itow, T. Suzuki, P. Mijakowski, K. Frankiewicz, J. Hig-
2623 night, J. Imber, C. K. Jung, X. Li, J. L. Palomino, M. J. Wilking, C. Yanag-
2624 isawa, D. Fukuda, H. Ishino, T. Kayano, A. Kibayashi, Y. Koshio, T. Mori,

- 2625 M. Sakuda, C. Xu, Y. Kuno, R. Tacik, S. B. Kim, H. Okazawa, Y. Choi,
2626 K. Nishijima, M. Koshiba, Y. Totsuka, Y. Suda, M. Yokoyama, C. Bronner,
2627 M. Hartz, K. Martens, Ll. Marti, Y. Suzuki, M. R. Vagins, J. F. Martin, A. Kon-
2628 aka, S. Chen, Y. Zhang, and R. J. Wilkes. Search for proton decay via $p \rightarrow e^+ \pi^0$
2629 and $p \rightarrow \mu^+ \pi^0$ in 0.31 megaton · years exposure of the super-kamiokande water
2630 cherenkov detector. *Phys. Rev. D*, 95:012004, Jan 2017.
- 2631 [5] R Acciarri, C Adams, J Asaadi, B Baller, T Bolton, C Bromberg, F Ca-
2632 vanna, E Church, D Edmunds, A Ereditato, S Farooq, B Fleming, H Greenlee,
2633 G Horton-Smith, C James, E Klein, K Lang, P Laurens, D McKee, R Mehdiyev,
2634 B Page, O Palamara, K Partyka, G Rameika, B Rebel, M Soderberg, J Spitz,
2635 A M Szelc, M Weber, M Wojcik, T Yang, and G P Zeller. A study of electron
2636 recombination using highly ionizing particles in the argoneut liquid argon tpc.
2637 *Journal of Instrumentation*, 8(08):P08005, 2013.
- 2638 [6] R Acciarri, M Antonello, B Baibussinov, M Baldo-Ceolin, P Benetti,
2639 F Calaprice, E Calligarich, M Cambiaghi, N Canci, F Carbonara, F Cavanna,
2640 S Centro, A G Cocco, F Di Pompeo, G Fiorillo, C Galbiati, V Gallo, L Grandi,
2641 G Meng, I Modena, C Montanari, O Palamara, L Pandola, G B Piano Mortari,
2642 F Pietropaolo, G L Raselli, M Roncadelli, M Rossella, C Rubbia, E Segreto,
2643 A M Szelc, S Ventura, and C Vignoli. Effects of nitrogen contamination in
2644 liquid argon. *Journal of Instrumentation*, 5(06):P06003, 2010.
- 2645 [7] R. Acciarri et al. Demonstration and Comparison of Operation of Photomulti-
2646 plier Tubes at Liquid Argon Temperature. *JINST*, 7:P01016, 2012.
- 2647 [8] R. Acciarri et al. Design and Construction of the MicroBooNE Detector. *JINST*,
2648 12(02):P02017, 2017.

- 2649 [9] R. Acciarri et al. First Observation of Low Energy Electron Neutrinos in a
2650 Liquid Argon Time Projection Chamber. *Phys. Rev.*, D95(7):072005, 2017.
2651 [Phys. Rev.D95,072005(2017)].
- 2652 [10] M Adamowski, B Carls, E Dvorak, A Hahn, W Jaskierny, C Johnson, H Jostlein,
2653 C Kendziora, S Lockwitz, B Pahlka, R Plunkett, S Pordes, B Rebel, R Schmitt,
2654 M Stancari, T Tope, E Voirin, and T Yang. The liquid argon purity demon-
2655 strator. *Journal of Instrumentation*, 9(07):P07005, 2014.
- 2656 [11] C. Adams et al. The Long-Baseline Neutrino Experiment: Exploring Funda-
2657 mental Symmetries of the Universe. 2013.
- 2658 [12] P. Adamson, L. Aliaga, D. Ambrose, N. Anfimov, A. Antoshkin, E. Arrieta-
2659 Diaz, K. Augsten, A. Aurisano, C. Backhouse, M. Baird, B. A. Bambah,
2660 K. Bays, B. Behera, S. Bending, R. Bernstein, V. Bhatnagar, B. Bhuyan,
2661 J. Bian, T. Blackburn, A. Bolshakova, C. Bromberg, J. Brown, G. Brunetti,
2662 N. Buchanan, A. Butkevich, V. Bychkov, M. Campbell, E. Catano-Mur, S. Chil-
2663 dress, B. C. Choudhary, B. Chowdhury, T. E. Coan, J. A. B. Coelho, M. Colo,
2664 J. Cooper, L. Corwin, L. Cremonesi, D. Cronin-Hennessy, G. S. Davies, J. P.
2665 Davies, P. F. Derwent, R. Dharmapalan, P. Ding, Z. Djurcic, E. C. Dukes,
2666 H. Duyang, S. Edayath, R. Ehrlich, G. J. Feldman, M. J. Frank, M. Gabrielyan,
2667 H. R. Gallagher, S. Germani, T. Ghosh, A. Giri, R. A. Gomes, M. C. Goodman,
2668 V. Grichine, R. Group, D. Grover, B. Guo, A. Habig, J. Hartnell, R. Hatcher,
2669 A. Hatzikoutelis, K. Heller, A. Himmel, A. Holin, J. Hylen, F. Jediny, M. Judah,
2670 G. K. Kafka, D. Kalra, S. M. S. Kasahara, S. Kasetti, R. Keloth, L. Kolupaeva,
2671 S. Kotelnikov, I. Kourbanis, A. Kreymer, A. Kumar, S. Kurbanov, K. Lang,
2672 W. M. Lee, S. Lin, J. Liu, M. Lokajicek, J. Lozier, S. Luchuk, K. Maan, S. Mag-
2673 ill, W. A. Mann, M. L. Marshak, K. Matera, V. Matveev, D. P. Méndez, M. D.
2674 Messier, H. Meyer, T. Miao, W. H. Miller, S. R. Mishra, R. Mohanta, A. Moren,

- 2675 L. Mualem, M. Muether, S. Mufson, R. Murphy, J. Musser, J. K. Nelson,
2676 R. Nichol, E. Niner, A. Norman, T. Nosek, Y. Oksuzian, A. Olshevskiy, T. Ol-
2677 son, J. Paley, P. Pandey, R. B. Patterson, G. Pawloski, D. Pershey, O. Petrova,
2678 R. Petti, S. Phan-Budd, R. K. Plunkett, R. Poling, B. Potukuchi, C. Principato,
2679 F. Psihas, A. Radovic, R. A. Rameika, B. Rebel, B. Reed, D. Rocco, P. Rojas,
2680 V. Ryabov, K. Sachdev, P. Sail, O. Samoylov, M. C. Sanchez, R. Schroeter,
2681 J. Sepulveda-Quiroz, P. Shanahan, A. Sheshukov, J. Singh, J. Singh, P. Singh,
2682 V. Singh, J. Smolik, N. Solomey, E. Song, A. Sousa, K. Soustruznik, M. Strait,
2683 L. Suter, R. L. Talaga, M. C. Tamsett, P. Tas, R. B. Thayyullathil, J. Thomas,
2684 X. Tian, S. C. Tognini, J. Tripathi, A. Tsaris, J. Urheim, P. Vahle, J. Vasel,
2685 L. Vinton, A. Vold, T. Vrba, B. Wang, M. Wetstein, D. Whittington, S. G. Wo-
2686 jcicki, J. Wolcott, N. Yadav, S. Yang, J. Zalesak, B. Zamorano, and R. Zwaska.
2687 Constraints on oscillation parameters from ν_e appearance and ν_μ disappearance
2688 in nova. *Phys. Rev. Lett.*, 118:231801, Jun 2017.
- 2689 [13] Alan Agresti. *Categorical Data Analysis*. Wiley Series in Probability and Statis-
2690 tics. Wiley, 2013.
- 2691 [14] A. Aguilar-Arevalo et al. Evidence for neutrino oscillations from the observation
2692 of anti-neutrino(electron) appearance in a anti-neutrino(muon) beam. *Phys.*
2693 *Rev.*, D64:112007, 2001.
- 2694 [15] A. A. Aguilar-Arevalo et al. Improved Search for $\bar{\nu}_\mu \rightarrow \bar{\nu}_e$ Oscillations in the
2695 MiniBooNE Experiment. *Phys. Rev. Lett.*, 110:161801, 2013.
- 2696 [16] S. Amoruso et al. Study of electron recombination in liquid argon with the
2697 ICARUS TPC. *Nucl. Instrum. Meth.*, A523:275–286, 2004.
- 2698 [17] C. Anderson et al. The ArgoNeuT Detector in the NuMI Low-Energy beam
2699 line at Fermilab. *JINST*, 7:P10019, 2012.

- 2700 [18] C. Andreopoulos et al. The GENIE Neutrino Monte Carlo Generator. *Nucl.*
2701 *Instrum. Meth.*, A614:87–104, 2010.
- 2702 [19] Timofei Bolshakov Andrey Petrov. Java synoptic toolkit. Technical report,
2703 Sept 2010.
- 2704 [20] M. Antonello, B. Baibussinov, P. Benetti, E. Calligarich, N. Canci, S. Cen-
2705 tro, A. Cesana, K. Cieslik, D. B. Cline, A. G. Cocco, A. Dabrowska, D. De-
2706 qual, A. Dermenev, R. Dolfini, C. Farnese, A. Fava, A. Ferrari, G. Fiorillo,
2707 D. Gibin, S. Gninenko, A. Guglielmi, M. Haranczyk, J. Holeczek, A. Ivashkin,
2708 J. Kisiel, I. Kochanek, J. Lagoda, S. Mania, A. Menegolli, G. Meng, C. Monta-
2709 nari, S. Otwinowski, A. Piazzoli, P. Picchi, F. Pietropaolo, P. Plonski, A. Rap-
2710 poldi, G. L. Raselli, M. Rossella, C. Rubbia, P. Sala, A. Scaramelli, E. Seg-
2711 reto, F. Sergiampietri, D. Stefan, J. Stepaniak, R. Sulej, M. Szarska, M. Ter-
2712 rani, F. Varanini, S. Ventura, C. Vignoli, H. Wang, X. Yang, A. Zalewska,
2713 and K. Zaremba. Precise 3d track reconstruction algorithm for the ICARUS
2714 t600 liquid argon time projection chamber detector. *Advances in High Energy*
2715 *Physics*, 2013:1–16, 2013.
- 2716 [21] M. Antonello et al. A Proposal for a Three Detector Short-Baseline Neutrino
2717 Oscillation Program in the Fermilab Booster Neutrino Beam. 2015.
- 2718 [22] D. Ashery, I. Navon, G. Azuelos, H. K. Walter, H. J. Pfeiffer, and F. W.
2719 Schlepütz. True absorption and scattering of pions on nuclei. *Phys. Rev. C*,
2720 23:2173–2185, May 1981.
- 2721 [23] C. Athanassopoulos et al. Evidence for $\nu(\mu) \rightarrow \nu(e)$ neutrino oscillations
2722 from LSND. *Phys. Rev. Lett.*, 81:1774–1777, 1998.

- 2723 [24] Borut Bajc, Junji Hisano, Takumi Kuwahara, and Yuji Omura. Threshold
2724 corrections to dimension-six proton decay operators in non-minimal {SUSY}
2725 $\text{su}(5)$ {GUTs}. *Nuclear Physics B*, 910:1 – 22, 2016.
- 2726 [25] B. Baller. Trajcluster user guide. Technical report, apr 2016.
- 2727 [26] Gary Barker. Neutrino event reconstruction in a liquid argon TPC. *Journal of*
2728 *Physics: Conference Series*, 308:012015, jul 2011.
- 2729 [27] BASF Corp. 100 Park Avenue, Florham Park, NJ 07932 USA.
- 2730 [28] R. Becker-Szendy, C. B. Bratton, D. R. Cady, D. Casper, R. Claus, M. Crouch,
2731 S. T. Dye, W. Gajewski, M. Goldhaber, T. J. Haines, P. G. Halverson, T. W.
2732 Jones, D. Kielczewska, W. R. Kropp, J. G. Learned, J. M. LoSecco, C. Mc-
2733 Grew, S. Matsuno, J. Matthews, M. S. Mudah, L. Price, F. Reines, J. Schultz,
2734 D. Sinclair, H. W. Sobel, J. L. Stone, L. R. Sulak, R. Svoboda, G. Thornton,
2735 and J. C. van der Velde. Search for proton decay into $e^+ + \pi^0$ in the imb-3
2736 detector. *Phys. Rev. D*, 42:2974–2976, Nov 1990.
- 2737 [29] J B Birks. Scintillations from organic crystals: Specific fluorescence and relative
2738 response to different radiations. *Proceedings of the Physical Society. Section A*,
2739 64(10):874, 1951.
- 2740 [30] A. Bodek and J. L. Ritchie. Further studies of fermi-motion effects in lepton
2741 scattering from nuclear targets. *Phys. Rev. D*, 24:1400–1402, Sep 1981.
- 2742 [31] Mark G. Boulay and A. Hime. Direct WIMP detection using scintillation time
2743 discrimination in liquid argon. 2004.
- 2744 [32] D. V. Bugg, R. S. Gilmore, K. M. Knight, D. C. Salter, G. H. Stafford, E. J. N.
2745 Wilson, J. D. Davies, J. D. Dowell, P. M. Hattersley, R. J. Homer, A. W. O'dell,

- 2746 A. A. Carter, R. J. Tapper, and K. F. Riley. Kaon-nucleon total cross sections
2747 from 0.6 to 2.65 gev/ *c. Phys. Rev.*, 168:1466–1475, Apr 1968.
- 2748 [33] W. M. Burton and B. A. Powell. Fluorescence of tetraphenyl-butadiene in the
2749 vacuum ultraviolet. *Applied Optics*, 12(1):87, jan 1973.
- 2750 [34] CAEN. Caen v1495 data sheet. Technical report, jan 2018.
- 2751 [35] CAEN. Caen v1740 data sheet. Technical report, jan 2018.
- 2752 [36] A. S. Carroll, I. H. Chiang, C. B. Dover, T. F. Kycia, K. K. Li, P. O. Mazur,
2753 D. N. Michael, P. M. Mockett, D. C. Rahm, and R. Rubinstein. Pion-nucleus
2754 total cross sections in the (3,3) resonance region. *Phys. Rev. C*, 14:635–638,
2755 Aug 1976.
- 2756 [37] D. Casper. The nuance neutrino physics simulation, and the future. *Nuclear
2757 Physics B - Proceedings Supplements*, 112(1-3):161–170, nov 2002.
- 2758 [38] A. Cervera, A. Donini, M.B. Gavela, J.J. Gomez Cádenas, P. Hernández,
2759 O. Mena, and S. Rigolin. Golden measurements at a neutrino factory. *Nu-
2760 clear Physics B*, 579(1-2):17–55, jul 2000.
- 2761 [39] E. Church. LArSoft: A Software Package for Liquid Argon Time Projection
2762 Drift Chambers. 2013.
- 2763 [40] ATLAS Collaboration. Observation of a new particle in the search for the
2764 standard model higgs boson with the ATLAS detector at the LHC. *Physics
2765 Letters B*, 716(1):1–29, sep 2012.
- 2766 [41] CMS Collaboration. Observation of a new boson at a mass of 125 gev with the
2767 cms experiment at the lhc. *Physics Letters B*, 716(1):30 – 61, 2012.
- 2768 [42] The LArIAT Collaboration. The liquid argon in a testbeam (lariat) experiment.
2769 Technical report, In Preparation 2018.

- 2770 [43] Stefano Dell’Oro, Simone Marcocci, Matteo Viel, and Francesco Vissani. Neu-
2771 trinoless double beta decay: 2015 review. *Advances in High Energy Physics*,
2772 2016:1–37, 2016.
- 2773 [44] S.E. Derenzo, A.R. Kirschbaum, P.H. Eberhard, R.R. Ross, and F.T. Solmitz.
2774 Test of a liquid argon chamber with 20 m rms resolution. *Nuclear Instruments
2775 and Methods*, 122:319 – 327, 1974.
- 2776 [45] Savas Dimopoulos, Stuart Raby, and Frank Wilczek. Proton Decay in Super-
2777 symmetric Models. *Phys. Lett.*, B112:133, 1982.
- 2778 [46] D. Drakoulakos et al. Proposal to perform a high-statistics neutrino scattering
2779 experiment using a fine-grained detector in the NuMI beam. 2004.
- 2780 [47] A Ereditato, C C Hsu, S Janos, I Kreslo, M Messina, C Rudolf von Rohr,
2781 B Rossi, T Strauss, M S Weber, and M Zeller. Design and operation of
2782 argontube: a 5 m long drift liquid argon tpc. *Journal of Instrumentation*,
2783 8(07):P07002, 2013.
- 2784 [48] Torleif Ericson and Wolfram Weise. *Pions and Nuclei (The International Series
2785 of Monographs on Physics)*. Oxford University Press, 1988.
- 2786 [49] A.A. Aguilar-Arevalo et al. The miniboone detector. *Nuclear Instruments and
2787 Methods in Physics Research Section A: Accelerators, Spectrometers, Detectors
2788 and Associated Equipment*, 599(1):28 – 46, 2009.
- 2789 [50] Antonio Bueno et al. Nucleon decay searches with large liquid argon TPC de-
2790 tectors at shallow depths: atmospheric neutrinos and cosmogenic backgrounds.
2791 *Journal of High Energy Physics*, 2007(04):041–041, apr 2007.
- 2792 [51] A.S. Clough et al. Pion-nucleus total cross sections from 88 to 860 MeV. *Nuclear
2793 Physics B*, 76(1):15–28, jul 1974.

- 2794 [52] B.W. Allardyce et al. Pion reaction cross sections and nuclear sizes. *Nuclear*
2795 *Physics A*, 209(1):1 – 51, 1973.
- 2796 [53] C Athanassopoulos et al. The liquid scintillator neutrino detector and LAMPF
2797 neutrino source. *Nuclear Instruments and Methods in Physics Research Section*
2798 *A: Accelerators, Spectrometers, Detectors and Associated Equipment*, 388(1-
2799 2):149–172, mar 1997.
- 2800 [54] F. Binon et al. Scattering of negative pions on carbon. *Nuclear Physics B*,
2801 17(1):168 – 188, 1970.
- 2802 [55] L. Aliaga et al. Minerva neutrino detector response measured with test beam
2803 data. *Nuclear Instruments and Methods in Physics Research Section A: Ac-*
2804 *celerators, Spectrometers, Detectors and Associated Equipment*, 789:28 – 42,
2805 2015.
- 2806 [56] M Adamowski et al. The liquid argon purity demonstrator. *Journal of Instru-*
2807 *mentation*, 9(07):P07005, 2014.
- 2808 [57] P. Vilain et al. Coherent single charged pion production by neutrinos. *Physics*
2809 *Letters B*, 313(1-2):267–275, aug 1993.
- 2810 [58] R. Acciarri et al. Convolutional neural networks applied to neutrino events
2811 in a liquid argon time projection chamber. *Journal of Instrumentation*,
2812 12(03):P03011, 2017.
- 2813 [59] R. Acciarri et al. Design and construction of the MicroBooNE detector. *Journal*
2814 *of Instrumentation*, 12(02):P02017–P02017, feb 2017.
- 2815 [60] C. E. Aalseth et al.l. DarkSide-20k: A 20 tonne two-phase LAr TPC for direct
2816 dark matter detection at LNGS. *The European Physical Journal Plus*, 133(3),
2817 mar 2018.

- 2818 [61] H Fenker. Standard beam pwc for fermilab. Technical report, Fermi National
2819 Accelerator Lab., Batavia, IL (USA), 1983.
- 2820 [62] H Fesbach. Theoretical nuclear physics: Nuclear reactions. 1992.
- 2821 [63] J. A. Formaggio and G. P. Zeller. From ev to eev: Neutrino cross sections across
2822 energy scales. *Rev. Mod. Phys.*, 84:1307–1341, Sep 2012.
- 2823 [64] E. Friedman et al. K+ nucleus reaction and total cross-sections: New analysis
2824 of transmission experiments. *Phys. Rev.*, C55:1304–1311, 1997.
- 2825 [65] V.M. Gehman, S.R. Seibert, K. Rielage, A. Hime, Y. Sun, D.-M. Mei,
2826 J. Maassen, and D. Moore. Fluorescence efficiency and visible re-emission
2827 spectrum of tetraphenyl butadiene films at extreme ultraviolet wavelengths.
2828 *Nuclear Instruments and Methods in Physics Research Section A: Accelerators,*
2829 *Spectrometers, Detectors and Associated Equipment*, 654(1):116 – 121, 2011.
- 2830 [66] H. Geiger and E. Marsden. On a diffuse reflection of the formula-particles.
2831 *Proceedings of the Royal Society A: Mathematical, Physical and Engineering*
2832 *Sciences*, 82(557):495–500, jul 1909.
- 2833 [67] Howard Georgi and S. L. Glashow. Unity of all elementary-particle forces. *Phys.*
2834 *Rev. Lett.*, 32:438–441, Feb 1974.
- 2835 [68] D.Y. Wong (editor) G.L. Shaw (Editor). *Pion-nucleon Scattering*. John Wiley
2836 & Sons Inc, 1969.
- 2837 [69] Glassman High Voltage, Inc., Precision Regulated High Voltage DC Power Sup-
2838 ply.
- 2839 [70] D S Gorbunov. Sterile neutrinos and their role in particle physics and cosmology.
2840 *Physics-Uspekhi*, 57(5):503, 2014.

- 2841 [71] C. Green, J. Kowalkowski, M. Paterno, M. Fischler, L. Garren, and Q. Lu. The
2842 Art Framework. *J. Phys. Conf. Ser.*, 396:022020, 2012.
- 2843 [72] S. Hansen, D. Jensen, G. Savage, E. Skup, and A. Soha. Fermilab test beam
2844 multi-wire proportional chamber tracking system upgrade. June 2014. International
2845 Conference on Technology and Instrumentation in Particle Physics (TIPP
2846 2014).
- 2847 [73] J. Harada. Non-maximal θ_{23} , large θ_{13} and tri-bimaximal θ_{12} via quark-
2848 lepton complementarity at next-to-leading order. *EPL (Europhysics Letters)*,
2849 103(2):21001, 2013.
- 2850 [74] Peter W. Higgs. Broken symmetries and the masses of gauge bosons. *Physical*
2851 *Review Letters*, 13(16):508–509, oct 1964.
- 2852 [75] P.W. Higgs. Broken symmetries, massless particles and gauge fields. *Physics*
2853 *Letters*, 12(2):132–133, sep 1964.
- 2854 [76] H J Hilke. Time projection chambers. *Reports on Progress in Physics*,
2855 73(11):116201, 2010.
- 2856 [77] N. Ishida, M. Chen, T. Doke, K. Hasuike, A. Hitachi, M. Gaudreau, M. Kase,
2857 Y. Kawada, J. Kikuchi, T. Komiyama, K. Kuwahara, K. Masuda, H. Okada,
2858 Y.H. Qu, M. Suzuki, and T. Takahashi. Attenuation length measurements of
2859 scintillation light in liquid rare gases and their mixtures using an improved
2860 reflection suppresser. *Nuclear Instruments and Methods in Physics Research*
2861 *Section A: Accelerators, Spectrometers, Detectors and Associated Equipment*,
2862 384(2-3):380–386, jan 1997.
- 2863 [78] G. Pulliam J. Asaadi, E. Gramellini. Determination of the electron lifetime in
2864 lariat. Technical report, August 2017.

- 2865 [79] George Jaffé. Zur theorie der ionisation in kolonnen. *Annalen der Physik*,
2866 347(12):303–344, 1913.
- 2867 [80] C. Jarlskog. A basis independent formulation of the connection between quark
2868 mass matrices, CP violation and experiment. *Zeitschrift für Physik C Particles
2869 and Fields*, 29(3):491–497, sep 1985.
- 2870 [81] B J P Jones, C S Chiu, J M Conrad, C M Ignarra, T Katori, and M Toups. A
2871 measurement of the absorption of liquid argon scintillation light by dissolved ni-
2872 tragen at the part-per-million level. *Journal of Instrumentation*, 8(07):P07011,
2873 2013.
- 2874 [82] Benjamin J. P. Jones. *Sterile Neutrinos in Cold Climates*. PhD thesis, MIT,
2875 2015.
- 2876 [83] Cezary Juszczak, Jarosław A. Nowak, and Jan T. Sobczyk. Simulations from
2877 a new neutrino event generator. *Nuclear Physics B - Proceedings Supplements*,
2878 159:211–216, sep 2006.
- 2879 [84] D. I. Kazakov. Beyond the standard model: In search of supersymmetry. In
2880 *2000 European School of high-energy physics, Caramulo, Portugal, 20 Aug-2 Sep 2000: Proceedings*, pages 125–199, 2000.
- 2882 [85] Dae-Gyu Lee, R. N. Mohapatra, M. K. Parida, and Merostar Rani. Predic-
2883 tions for the proton lifetime in minimal nonsupersymmetric $so(10)$ models: An
2884 update. *Phys. Rev. D*, 51:229–235, Jan 1995.
- 2885 [86] M A Leogui de Oliveira. Expression of Interest for a Full-Scale Detector Engi-
2886 neering Test and Test Beam Calibration of a Single-Phase LAr TPC. Technical
2887 Report CERN-SPSC-2014-027. SPSC-EOL-011, CERN, Geneva, Oct 2014.

- 2888 [87] W. H. Lippincott, K. J. Coakley, D. Gastler, A. Hime, E. Kearns, D. N. McK-
2889 insey, J. A. Nikkel, and L. C. Stonehill. Scintillation time dependence and pulse
2890 shape discrimination in liquid argon. *Phys. Rev. C*, 78:035801, Sep 2008.
- 2891 [88] Jorge L. Lopez and Dimitri V. Nanopoulos. Flipped SU(5): Origins and re-
2892 cent developments. In *15th Johns Hopkins Workshop on Current Problems*
2893 *in Particle Theory: Particle Physics from Underground to Heaven Baltimore,*
2894 *Maryland, August 26-28, 1991*, pages 277–297, 1991.
- 2895 [89] Vincent Lucas and Stuart Raby. Nucleon decay in a realistic so(10) susy gut.
2896 *Phys. Rev. D*, 55:6986–7009, Jun 1997.
- 2897 [90] Ettore Majorana. Teoria simmetrica dell'elettrone e del positrone. *Il Nuovo*
2898 *Cimento*, 14(4):171–184, apr 1937.
- 2899 [91] Hisakazu Minakata and Alexei Yu. Smirnov. Neutrino mixing and quark-lepton
2900 complementarity. *Phys. Rev. D*, 70:073009, Oct 2004.
- 2901 [92] M. Mooney. The microboone experiment and the impact of space charge effects.
2902 2015.
- 2903 [93] E. Morikawa, R. Reininger, P. Gürtler, V. Saile, and P. Laporte. Argon, kryp-
2904 ton, and xenon excimer luminescence: From the dilute gas to the condensed
2905 phase. *The Journal of Chemical Physics*, 91(3):1469–1477, aug 1989.
- 2906 [94] FM Newcomer, S Tedja, R Van Berg, J Van der Spiegel, and HH Williams.
2907 A fast, low power, amplifier-shaper-discriminator for high rate straw tracking
2908 systems. *IEEE Transactions on Nuclear Science*, 40(4):630–636, 1993.
- 2909 [95] Emmy Noether. Invariant variation problems. *Transport Theory and Statistical*
2910 *Physics*, 1(3):186–207, jan 1971.

- 2911 [96] I. Nutini. Study of charged particles interaction processes on ar in the 0.2 - 2.0
2912 GeV energy range through combined information from ionization free charge
2913 and scintillation light. Technical report, jan 2015.
- 2914 [97] D. R. Nygren. The time projection chamber: A new 4π detector for charged
2915 particles. Technical report, 1974.
- 2916 [98] L. Onsager. Initial recombination of ions. *Phys. Rev.*, 54:554–557, Oct 1938.
- 2917 [99] S. Pascoli, S.T. Petcov, and A. Riotto. Leptogenesis and low energy cp-violation
2918 in neutrino physics. *Nuclear Physics B*, 774(1):1 – 52, 2007.
- 2919 [100] C. Patrignani et al. Review of Particle Physics. *Chin. Phys.*, C40(10):100001,
2920 2016.
- 2921 [101] B. Pontecorvo. Neutrino Experiments and the Problem of Conservation of
2922 Leptonic Charge. *Sov. Phys. JETP*, 26:984–988, 1968. [Zh. Eksp. Teor.
2923 Fiz.53,1717(1967)].
- 2924 [102] T. Yang R. Acciarri. Investigation of the non-uniformity observed in the wire
2925 response to charge in lariat run 1. Technical report, February 2017.
- 2926 [103] T. Yang R. Acciarri, M. Stancari. Determination of the electron lifetime in
2927 lariat. Technical report, March 2016.
- 2928 [104] Martti Raidal. Relation between the neutrino and quark mixing angles and
2929 grand unification. *Phys. Rev. Lett.*, 93:161801, Oct 2004.
- 2930 [105] Steve Ritz et al. Building for Discovery: Strategic Plan for U.S. Particle Physics
2931 in the Global Context. 2014.
- 2932 [106] C. Rubbia. The Liquid Argon Time Projection Chamber: A New Concept for
2933 Neutrino Detectors. 1977.

- 2934 [107] L.M. Saunders. Electromagnetic production of pions from nuclei. *Nucl. Phys.*,
2935 *B7*: 293-310(1968).
- 2936 [108] Qaisar Shafi and Zurab Tavartkiladze. Neutrino democracy, fermion mass hier-
2937 archies, and proton decay from 5d su(5). *Phys. Rev. D*, 67:075007, Apr 2003.
- 2938 [109] Sigma-Aldrich, P.O. Box 14508, St. Louis, MO 63178 USA.
- 2939 [110] R. K. Teague and C. J. Pings. Refractive index and the lorentz–lorenz function
2940 for gaseous and liquid argon, including a study of the coexistence curve near the
2941 critical state. *The Journal of Chemical Physics*, 48(11):4973–4984, jun 1968.
- 2942 [111] J. Thomas and D. A. Imel. Recombination of electron-ion pairs in liquid argon
2943 and liquid xenon. *Phys. Rev. A*, 36:614–616, Jul 1987.
- 2944 [112] D.R.O. Morrison N. Rivoire V. Flaminio, W.G. Moorhead. Compilation of
2945 Cross Sections I: π^+ and π^- Induced Reactions. *CERN-HERA*, pages 83–01,
2946 1983.
- 2947 [113] D.R.O. Morrison N. Rivoire V. Flaminio, W.G. Moorhead. Compilation of
2948 Cross Sections II: K^+ and K^- Induced Reactions. *CERN-HERA*, pages 83–02,
2949 1983.
- 2950 [114] Hermann Weyl. Gravitation and the electron. *Proceedings of the National
2951 Academy of Sciences of the United States of America*, 15(4):323–334, 1929.
- 2952 [115] Colin et al Wilkin. A comparison of pi+ and pi- total cross-sections of light
2953 nuclei near the 3-3 resonance. *Nucl. Phys.*, B62:61–85, 1973.
- 2954 [116] D. H. Wright and M. H. Kelsey. The Geant4 Bertini Cascade. *Nucl. Instrum.
2955 Meth.*, A804:175–188, 2015.

- 2956 [117] C. S. Wu, E. Ambler, R. W. Hayward, D. D. Hoppes, and R. P. Hudson.
2957 Experimental test of parity conservation in beta decay. *Phys. Rev.*, 105:1413–
2958 1415, Feb 1957.
- 2959 [118] N Yahlali, L M P Fernandes, K Gonzlez, A N C Garcia, and A Soriano. Imaging
2960 with sipms in noble-gas detectors. *Journal of Instrumentation*, 8(01):C01003,
2961 2013.
- 2962 [119] T. Yanagida. Horizontal symmetry and masses of neutrinos. *Progress of Theo-*
2963 *retical Physics*, 64(3):1103–1105, sep 1980.